PFC/RR-87-4

SELF-CONSISTENT THEORY OF TRIGGERED WHISTLER EMISSIONS

Molvig K.; Hilfer, G.; Myczkowski, J.

March 1987

Plasma Fusion Center

Massachusetts Institute of Technology

Cambridge, Massachusetts 02139

This work was supported by the Office of Naval Research No. N00014-83-K-0319. Reproduction, translation, publication, use and disposal, in whole or part, by or for the United States government is permitted.

SELF-CONSISTENT THEORY OF TRIGGERED WHISTLER EMISSIONS

Kim Molvig , Godehard Hilfer, and Jacek Myczkowski

Nuclear Engineering Dept. & Plasma Fusion Center, MIT

ABSTRACT

A kinetic theory of triggered VLF whistler emissions is given that is capable of predicting from a small scale numerical implementation the observed emission forms, and frequency-time characteristics. The present paper focuses on the theoretical developments and the explanation of the triggering process, complete with a demonstration of the threshold behavior (sometimes known as the dot-dash anomaly) and the generation of specific falling frequency emissions that compare quite favorably to typical observations made in the controlled experiments based in Siple Station, Antarctica. The theory that gives these results is a fully self-consistent nonlinear treatment based on kinetic theory and valid in the asymptotic limit when several trapping periods occur within the interaction region. For a typical set of parameters, $l = 4.3$, $n = 400\ cm^{-3}$, and amplitude, $B_T \sim 1.6\ pT$, for the input wave magnetic field, one has about seven trapping periods in the triggering signal and would expect good results from the asymptotic limit. In this limit the nonlinear dynamics can be reduced to the determination of the time, τ, that the resonant particles are trapped. The nonlinear currents can be expressed in terms of this function, τ, by simple integrals over the trapped particles' perpendicular velocities alone. Most of the features of the emission process can be determined analytically and properties, such as the rate of change of frequency, related to magnetospheric parameters. For more quantitative predictions such as amplitude and frequency waveforms, a small numerical code which integrates the nonlinear wave equations is used. The theoretical picture of the triggering mechanism

contains the observed threshold behavior wherein short triggering pulses of nominal amplitude $B_T \sim 1\ pT$ and 100 ms in duration or less cannot generate an emission, whereas those in the 200 ms range and longer do. Similar sensitivity is found with respect to initial frequency, where in some cases 5.5 kHz signals can trigger, but 5.0 kHz signals cannot. Gains in the range of $20 - 30\ dB$ are obtained with initial temporal growth rates in the range $100 - 200\ dB/sec$. The emission process requires an inverted population in the perpendicular velocity distribution function but not necessarily linear instability. A sufficient number of high energy electrons is required that the driven currents can offset convection, but provided this is satisfied, a sufficiently long triggering signal will always generate a self-sustaining emission. Interestingly, however, the self-sustaining emission does not depend on the number of these high energy particles or the details of the velocity distribution function but only on bulk magnetospheric parameters such as magnetic field, gradient scale length, and the plasma density in the plasmapause. Also the marginal signals generated just above the threshold are always fallers as is observed. These features have not been explained by existing theories. Unresolved issues include the mechanism of termination, the generation of risers and hooks for more intense emission situations, and the detailed synchronization of the frequency time and amplitude waveforms. This last point requires the solution of a peculiar singular two-way wave equation for the phase which is presently solved in a subsidiary asymptotic limit valid within the interaction region. These unexplained points could well be explained within the present theory by the inclusion of the variable resonant velocity in the projection of the electron distribution function.

I. Introduction

Triggered VLF emissions have fascinated and challenged magnetospheric scientists for several decades[1]. Recently the observations have been carried into space[2-22] and provided *in situ* measurements of the wave fields at the point of origin of the emission phenomenon. Moreover, the spacecraft experiments have discovered similar emissions originating from the magnetospheres of Jupiter[9,19], Saturn[22], and most recently Uranus. In fact the cyclical, quasiperiodic nature of the emissions from Jupiter are reminiscent of the kind of behavior exhibited by pulsars[23] at much higher frequency. During these years of experimentation on terrestrial whistlers a quite detailed and quantitative picture of the observational properties has been compiled[24-26]. The challenge to theory has been to account for these varied features. Many of the qualitative physical features underlying these emissions have long been identified and understood[27-36]. Nonetheless, in spite of an impressive array of excellent theoretical work[36], the goal of a self-consistent, first principles theory capable of predicting the observed emission forms, threshold behavior, and frequency-time characteristics has remained elusive. The present paper describes such a theory (presented elsewhere in abbreviated form[37]) and gives the first results obtained from it.

The theory focuses on the controlled emission experiments as reviewed recently by Helliwell[38]. Coherent VLF signals in the frequency range $1.8 - 7\ kHz$ injected into the magnetosphere from Siple Station ($L = 4.2$), Antarctica, can be amplified by some 30 dB and, under the appropriate conditions, trigger intense narrowband whistler mode emissions. A key parameter in the experiments is the spectral purity of the transmitted signal. If the width of the signal spectrum exceeds $10\ Hz$, there is substantial loss of gain by as much as 20 dB. The occurrance of triggering exhibits a sharp threshold behavior with respect to input signal intensity and duration[38]. Onset of triggering appears at signal lengths[39] in the range of 50 to 100 ms and intensities of the order of kW, with these values varying somewhat according to magnetospheric conditions. Additional transmitter power has very little effect on received emission intensity once the threshold is exceeded. For near threshold values, the emissions tend to be fallers[39] following the termination of the input signal. At longer trigger lengths and under active magnetospheric conditions the emissions tend to be risers triggered before the end of the pulse[39].

Another key feature of the emissions is the constancy of their intensity, once they have been triggered[26,39]. Thus their nature is one of a rapidly varying frequency and nearly constant amplitude - exactly the opposite characteristics from what would appear in a linear amplification mechanism. The explanation of the observed features must lie

in the nonlinear dynamics[33-35]. Accordingly, the theory here to be developed focuses on the nonlinear dynamics surrounding particle trapping in the whistler signal. This is the strongest nonlinearity present. In fact trapping occurs for ratios of signal strength to earth's magnetic field[40], B_w/B_0, on the order of 10^{-5}. Of course, linear mechanisms, such as amplification of the trigger signal in propagating inside a duct from the ionosphere to the equator may play an important role in the overall picture.

The theoretical developments have been reviewed[24] by Matsumoto[36], and the reader is referred there for more specific discussion of the various contributions. The work of Nunn[33], however, should be emphasized as particularly insightful and instrumental to the developments we report. Although the theory was limited by its semi-empirical nature and required several ad hoc smoothing and damping parameters to render it numerically stable, it is the only complete self consistent theory previously given. The equations differ fundamentally from those of the present theory, which is, by contrast, a deductive asymptotic calculation, but some structural parallels exist.

Matsumoto's paper also reviewed the experiments as they pertain to theory and generated a list of features of artificially stimulated emissions that theory should explain. It is noteworthy that such a detailed morphology of the phenomenon can be ascertained directly from the observations. The list is repeated here with minor revisions:

1) MECHANISM FOR TRIGGERING exhibiting,

   a) Threshold behavior as a function of pulse length (also known as the dot-dash anomaly).

   b) Narrow frequency bandwidth ($\sim$ 100 Hz), and even narrower bandwidths ($\sim$ 10 Hz) required of the triggering signal.

   c) Triggering by both high and low power transmitters.

   d) Repeatability.

2) GROWTH OF SIGNALS by 20 to 35 bB.

   a) Exponential phase of triggering wave growth with rate of 25 - 250 dB/sec.

   b) Frequency lock to or within 200 Hz above triggering signal during growth phase.

   c) Release of emissions at times of growth stop or of triggering wave termination.

3) VARIATION IN FREQUENCY

a) Starting at the triggering frequency and rising initially.

b) Predominance of risers for longer triggering pulse and fallers for shorter pulse.

This is an almost verbatim version of Matsumoto's list, but organized under three main headings. All the features on this list can be accounted for by the results in this paper, discussed in section VII, with the exception of the first half of 3b - the risers. Risers are not excluded by the theory, of course, but do not occur for the marginal case near the triggering threshold which is emphasized in this paper. Although a suggestion of how risers would form will be given in Section VII, they have not been generated in a completely satisfactory manner to this point. There are several other important aspects of the problem that the theory has not yet explained and must be regarded as limitations, in spite of its ability to account for Matusmoto's list.

There are several specific points of the observational properties missing from Matsumoto's list that should also be explained from the theory, (and will be accounted for below):

4) Most active triggering occurring on times of low magnetic activity following substorms by several days.

5) Acute sensitivity to the initial frequency. Appearance of frequent triggering on the higher of two frequencies very close together, (5.5 kHz and 5.0 kHz), with *no* ASE's associated with the lower frequency.

6) Relative insensitivity of the total gain and the frequency variation to large changes in magnetospheric conditions.

Electrons moving along magnetic field lines can resonate with the perpendicular electric field of a right circularly polarized whistler wave propagating along field lines (because of the "ducting" phenomenon[41]) if the condition,

$$\omega - \Omega_{ce} = k v_{\|} \ , \qquad (1-1)$$

is satisfied. Since $\omega < \Omega_{ce}/2$ is required for ducting to be effective[1,41], eq.(1-1) implies that $v_{\|} < 0$, or that resonant electrons move opposite to the wave propagation direction. The resonance condition is not homogeneous since the magnetic field strength is a function of arc length, s. Consequently, the dominant interaction occurs where the resonance condition is locally stationary, or for constant frequency, near the magnetic equator. The concept of inhomogeneity induced frequency changes was first introduced by Hansen[42] and Helliwell[29]. Helliwell noted that if one requires equation (1-1) to be stationary as the electrons follow

their adiabatic orbits along the field lines, then the frequency change in time, $\dot{\omega}$, seen by the electrons is,

$$\dot{\omega} \propto -s \,, \qquad (1-2)$$

where $s = 0$ is the magnetic equator. Equation(1-2), known as the Helliwell condition, links risers to upstream emission and fallers to downstream emission, with the flow direction in our convention determined by the wave propagation. One of the problems for theory has been to derive this condition, if correct, from the self consistent nonlinear currents.

The theory follows a physical picture based on trapping near the equator for several trapping periods. This is a familiar idea and has been the basis of several previous works[29,33,34-37,43]. What is new in the present paper is to give this idea a complete mathematical formulation by deriving from it simple expressions for the nonlinear currents[36]. This then provides a basis for a physical understanding of the emission process itself, and detailed calculations of the frequency and amplitude waveforms, which is also new. The key idea that evolves from the analysis is the representation of the nonlinear current in terms of the time that each particle is trapped, $\tau(v_\perp, s, t)$. The nonlinear dynamics are then reduced to the solution of a simple convection equation for τ,

$$\left(\frac{\partial}{\partial t} + V_R \frac{\partial}{\partial s}\right)\tau = 1, \qquad (1-3)$$

which is integrated subject to the trapping condition[28-37,40,42-50], eq.(3-45). In contrast, in Nunn's theory[33] there are three equations in place of (1-3), two for the trapping vortex location in phase space and one for the volume of the this vortex. The trapping time, τ, is not explicitly computed in Ref.33 (although the trapping volume is given the symbol, τ).

Recent theoretical interest[40,45,47,49,50] has focused on the role of the untrapped resonant particles which may be important in some cases but are generally found to be a smaller contributor[40] to the currents than the trapped particles. In the present paper, these particles play a subdominant role and are absent from the leading order asymptotic theory (although they could easily be added to higher order approximations within the present framework).

Certain aspects of the theory and its applicability to observed phenomenon can be understood from some very simple considerations and formulas. These have been known, for the most part[28,29,32,34,35,40,44], but are derived as byproducts of the theory below as well. First there is the trapping threshold, determined by the condition that the resonant electrons undergo a full trapping period in crossing the equator. This condition sets a

lower bound on the wave magnetic field of the triggering wave,

$$B_T > 5.8\, l_4^{-13/3} n_{100}^{-2/3} (1-\omega/\Omega)^2 (\Omega/\omega)^{1/6} \left[1 - \frac{2}{3}\frac{L^2}{L_n^2}(1-\omega/\Omega)\right]^{1/6} \; pT \qquad (1-4)$$

Here the field strength is given in picotesla, the plasma density in units of 100 cm^{-3}, and l-shell number in units of 4, as appropriate for conditions near the plasmapause. The factor L/L_n gives the ratio of magnetic to density scale lengths, although the last factor in square brackets is very close to unity, and this is not very important here. The quantity, ω, is the wave frequency and Ω is the equatorial gyrofrequency. Note that the trapping threshold is a very strong function of l-number and frequency, such that trapping becomes much stronger at higher l and ω. If ducting[41] is required for the emission process, however, we must have $\omega/\Omega < 1/2$, so that emissions should occur most frequently near $\omega \sim \Omega$. This is indeed observed. The density dependence in eq.(1-4) will localize activity where the density is highest, opposing the tendency to move to higher l-shells. The net effect is to position the emission activity in the vicinity of the plasmapause[51].

There is some question as to the input signal strength, B_{TR} that actually arrives at the field line equator for triggering. Most direct satellite measurements in situ have tended[18] to find $B_{TR} \sim .05pT$ about an order of magnitude less than used in this paper and well below the trapping threshold. However at least some of the data[6] is biased toward smaller values of B_{TR}, and other measurements[11] have yielded $B_{TR} \sim .5pT$, very close to what we use. Also the satellites have always seen unducted signals whereas the emissions originate in ducts[6]. There is a likelihood that the ducted signals are much higher[5] because of linear preamplification, as is suggested independently by the echo triggered emissions[6]. Also if the coherency bandwidth condition[38,39] $\delta\omega/\omega \leq 2 \times 10^{-3}$ is used to infer the input signal strength via $\delta\omega(1+\Omega/2\omega) \sim \omega_{tr}$, one finds $B_{TR} \sim 1\ pT$. The "ramping" experiments[38,67] imply a similar number.

A related parameter is the inverse of the number of trapping periods, the expansion parameter of the asymptotic theory. This is measured by the factor,

$$C_o = \frac{9}{2l^2}\frac{c^2}{R_E^2\omega_{pe}^2}\left(\frac{B}{B_T}\frac{\Omega}{\omega_o}\frac{1}{\sqrt{\Omega/\omega_o - 1}}\right)^{3/2},$$

$$= 5.7 \times 10^{-9} l_4^{-2} n_{100}^{-1} \left(\frac{B}{B_T}\right)^{3/2}, \qquad (1-5)$$

where $\omega_o/\Omega = .4$ has been used for simplicity. For a typical set of parameters, $l = 4.3$, $n = 400\ cm^{-3}$, and $B_T/B = 4\times10^{-6}$ (this corresponds to $B_T \sim 1.6\ pT$), one has $C_o \sim .15$, implying about seven trapping periods.

Finally, the energies of the electrons responsible for the emission process[40,52] can be obtained from the resonant velocity and the dominant perpendicular velocity, $v_\perp^o$, of eq.(4-29). This gives the minimum resonant energy,

$$E_R = \tfrac{1}{2}mc^2 \frac{\Omega^2}{\omega_{pe}^2}\frac{\Omega}{\omega}(1-\omega/\Omega)^2\left[9+(1-2L^2/L_n^2)(1-\omega/\Omega)\right]$$
$$= 5.75\ l_4^{-6} n_{100}^{-1}\frac{\Omega}{\omega}(1-\omega/\Omega)^2\left[9+(1-2L^2/L_n^2)(1-\omega/\Omega)\right]\ keV\ . \qquad (1-6)$$

This exhibits a scaling with parameters that is similar to the trapping threshold.

Section II sets forth the WKB equations used as the framework for the theory. In section III, the asymptotic ordering is established and used to compute the electron orbits throughout the inhomogeneous trapping process. These orbits are used as characteristics to compute the nonlinear currents in section IV. This section obtains the expression for the trapping time, τ, as well as the trapping and cutoff conditions, to give the theory a self-consistent, closed form. Section V draws the picture of the emission process that can be inferred directly from the nonlinear theory. Features that can be seen from the theory at this level include: 1) the relation of triggering to an inversion in the perpendicular velocity distribution function (without requiring linear instability); 2) the dot-dash anomaly; 3) the appearance of an initial rise in frequency followed by a rapidly falling tone for the marginal self-sustaining emission. Section VI describes the numerical procedure used to advance the nonlinear wave equations. A detailed discussion of the numerical results and comparison with the experimental observations is given in section VII. The main results and conclusions are summarized in section VIII.

II. WKB Wave Equations

Observed emissions satisfy the general requirements of WKB in that the propagation characteristics of the waves are linear[33] (due to the cold electrons). The wave length is the shortest spatial scale and the wave period is smaller than the time scale of amplitude evolution. We follow the formal developments as given by Bernstein[53], but include in the first order current a general non-linear dependence on the complex wave amplitude. The wave electric field is represented in the eikonal form, to leading order, as

$$\mathbf{E}(s,t) = \alpha_1(s,t)e^{i\psi_w(s,t)}\mathbf{e}_1 \qquad (2-1)$$

where s is the arc length coordinate along the field line and $\mathbf{e}_1 = (\mathbf{e}_x + i\mathbf{e}_y)/2$ is the Whistler polarization vector, and the wave frequency and wave number are given by

$$\omega = -\frac{\partial\psi_w}{\partial t}, \qquad k = \frac{\partial\psi_w}{\partial s}. \qquad (2-2)$$

The WKB equations are obtained by an expansion in $\frac{1}{\omega}\frac{\partial\alpha_1}{\partial t} \sim \frac{1}{k}\frac{\partial\alpha_1}{\partial s}$, giving, at first order, an evolution equation for the complex amplitude, α_1,

$$\sum_l \left\{ -\mathbf{e}_j^* \cdot \frac{\partial\omega\underline{\underline{\epsilon}}}{\partial\omega} \cdot \mathbf{e}_l \frac{\partial\alpha_l}{\partial t} + \left[(\nabla_{\mathbf{k}}\omega\underline{\underline{\epsilon}}) : \mathbf{e}_l\mathbf{e}_j^*\right] \cdot \nabla\alpha_j \right\} = \beta_j, \qquad (2-3)$$

where,

$$\begin{aligned}\beta_j = \sum_l \alpha_l \mathbf{e}_j^* \Bigg\{ & \frac{\partial}{\partial\omega}(\omega\underline{\underline{\epsilon}}) \cdot \frac{\partial\mathbf{e}_l}{\partial t} + \frac{1}{2}\left[\frac{\partial}{\partial t}\left(\frac{\partial(\omega\underline{\underline{\epsilon}})}{\partial t}\right)\right] \cdot \mathbf{e}_l \\ & - \left[(\nabla\mathbf{e}_l)^T \cdot \nabla_{\mathbf{k}}\right] \cdot \omega\underline{\underline{\epsilon}}^T - \frac{1}{2}\left[\nabla \cdot (\nabla_{\mathbf{k}}\omega\underline{\underline{\epsilon}})\right] \cdot \mathbf{e}_l \\ & + 4\pi\underline{\underline{\sigma}}^H \cdot \mathbf{e}_l \Bigg\} - 4\pi e^{-i\psi_w}\mathbf{e}_1^* \cdot \mathbf{J}_{NL}\left[E_T A e^{i(\varphi+\psi_w)}\mathbf{e}_1\right], \end{aligned} \qquad (2-4)$$

and the sum, in eqs.(2-3)and(2-4), runs over the system eigenmodes. The dielectric tensor, $\underline{\underline{\epsilon}}(\mathbf{k},\omega)$, is written,

$$\underline{\underline{\epsilon}} = \epsilon_1\mathbf{e}_1\mathbf{e}_1^* + \epsilon_2\mathbf{e}_2\mathbf{e}_2^* + \epsilon_3\mathbf{e}_3\mathbf{e}_3^*. \qquad (2-5)$$

We assume there is no coupling of modes or degeneracy in the propagation of the Whistler emission, so that $\epsilon_2 \neq 0$, $\epsilon_3 \neq 0$, and

$$\epsilon_1 = 1 - \frac{c^2k^2}{\omega^2} - \frac{\omega_{pe}^2}{\omega(\omega-\Omega)}, \qquad (2-6)$$

gives the Whistler dispersion relation. In here ω_{pe}^2 represents the local plasma frequency and Ω the local gyro frequency. In this case the following relations hold,

$$\mathbf{e}_1^* \cdot \frac{\partial}{\partial \omega}(\omega \underline{\underline{\epsilon}}) \cdot \mathbf{e}_l = \frac{\partial}{\partial \omega} \omega \epsilon_1, \qquad (2-7)$$

$$\frac{\partial}{\partial t}\mathbf{e}_1 = 0; \quad \nabla \mathbf{e}_1 = 0; \quad \frac{\partial}{\partial t}\epsilon_1 = 0, \qquad (2-8)$$

and,

$$\nabla_{\mathbf{k}} \omega \underline{\underline{\epsilon}} : \ \mathbf{e}_1 \mathbf{e}_1^* = \nabla_{\mathbf{k}} \omega \epsilon_1 = -\frac{\partial \omega}{\partial \mathbf{k}} \frac{\partial}{\partial \omega}(\omega \epsilon_1) = -\mathbf{v}_g \frac{\partial}{\partial \omega}(\omega \epsilon_1). \qquad (2-9)$$

Using eqs. (2-7), (2-8), and (2-9), eq. (2-3) for the complex Whistler amplitude becomes,

$$\frac{\partial \alpha_1}{\partial t} + \mathbf{v}_g \cdot \nabla \alpha_1 + \gamma \alpha_1 = -\frac{4\pi e^{-i\psi_w} \mathbf{e}_1^* \cdot \mathbf{J}_{NL}\left[E_T A e^{i(\varphi+\psi_w)} \mathbf{e}_1\right]}{\omega \partial \epsilon_1 / \partial \omega} - \frac{\alpha_1}{2} \frac{1}{\frac{\partial}{\partial \omega}(\omega \epsilon_1)} \nabla \cdot \left[\mathbf{v}_g \frac{\partial}{\partial \omega}(\omega \epsilon_1)\right] \qquad (2-10)$$

where,

$$\gamma = \frac{4\pi \mathbf{e}_1^* \cdot \underline{\underline{\sigma}}^H \cdot \mathbf{e}_1}{\omega \partial \epsilon_1 / \partial \omega}, \qquad (2-11)$$

is the linear damping decrement due to the background plasma which contains the Hermetian piece of the conductivity tensor $\underline{\underline{\sigma}}^H$.

We now specialize and scale these equations to the problem at hand. First we neglect the linear damping and the divergence of the group velocity (as higher order in the $\epsilon^{1/3}$ expansion as outlined below). The field amplitude is written

$$\alpha_1 = E_T A e^{i\varphi}, \qquad (2-12)$$

where E_T is the field of the triggering wave, so that A is a dimensionless, order unity, slowly varying amplitude. We then scale the velocity to $V_s = c\Omega_0/\omega_{pe0}$ (gyrofrequency and plasma frequency values at the equator) and the time period to $\omega_s = \sqrt{\Omega \omega_{pe} E_T / B}$. Then eq.(2-10) and eq.(2-12) combine to

$$e^{i\varphi}\left(\frac{\partial}{\partial t} + \frac{v_g}{V_s}\frac{\partial}{\partial s}\right) A + iAe^{i\varphi}\left(\frac{\partial}{\partial t} + \frac{v_g}{V_s}\frac{\partial}{\partial s}\right)\varphi = -\frac{4\pi e^{-i\psi_w} \mathbf{e}_1^* \cdot \mathbf{J}_{NL}\left[E_T A e^{i(\varphi+\psi_w)} \mathbf{e}_1\right]}{(\omega \partial \epsilon_1 / \partial \omega) \omega_s E_T} \qquad (2-13)$$

Defining the real and imaginary parts of the non-linear current as,

$$I_R = Re\left\{ \frac{4\pi e^{-i(\psi_w+\varphi)}\mathbf{e}_1^* \cdot \mathbf{J}_{NL}}{(\omega\partial\epsilon/\partial\omega)\omega_s E_T} \right\} \qquad (2-14)$$

and,

$$I_I = Im\left\{ \frac{4\pi e^{-i(\psi_w+\varphi)}\mathbf{e}_1^* \cdot \mathbf{J}_{NL}}{(\omega\partial\epsilon/\partial\omega)\omega_s E_T} \right\} \qquad (2-15)$$

gives the dimensionless wave equations

$$\left(\frac{\partial}{\partial t} + \frac{v_g}{V_s}\frac{\partial}{\partial s} \right) A = -I_R \qquad (2-16)$$

and,

$$\left(\frac{\partial}{\partial t} + \frac{v_g}{V_s}\frac{\partial}{\partial s} \right) \varphi = -I_I/A \qquad (2-17)$$

which are in form similar to wave equations in References [31,33,45].

Note that the slowly varying wave phase φ is included with ψ_w in computing the non-linear current, so that frequency shifts, $\delta\omega = -\partial\varphi/\partial t$, away from the triggering frequency, $\omega = -\partial\psi_w/\partial t$, are included in the non-linear current.

III. Asymptotic Orbit Theory

The wave magnetic fields[11,40], B_w, encountered in artificially stimulated emissions as well as in natural whistlers, emissions of chorus[54] and hiss, are in the range of 10 pT or less. This is some five orders of magnitude smaller than the background magnetospheric field, B, at the plasmapause and provides an excellent smallness parameter, $\varepsilon \sim \sqrt{B_w/B}$, for an asymptotic theory. The inhomogeneity is likewise small as measured by the dimensionless parameter, $c/(\omega_{pe} l R_E) \sim 10^{-4}$. These two parameters can be related by a formal ordering which turns out to be $c/(\omega_{pe} l R_E) \sim (B_w/B)^{5/6}$ (and is, therefore, quite realistic as well) leading to analytic expressions for the orbit characteristics, as required for the kinetic theory.

The number of trapping oscillations a particle undergoes in passing through the interaction region is nominally $\varepsilon^{-1/3} \sim 7$, for the triggered emission problem. For the field strengths found in chorus, this number could be somewhat larger. The theory developed here considers the limit where many trapping periods occur within the interaction region and the relative oscillations in the parallel velocity are small. Then, because the rate of change of wave frequency with time is slow and the spatial inhomogeneity in the magnetic field is weak, motion along the field lines occurs on a slower time scale than trapping. There is an adiabatic invariant[34,40] associated with this motion that allows an analytic description of the detailed structure of the trapping vortex in phase space.

A. Asymptotic Ordering

The exact equations for the orbits[28-34,40,45-49,55-58] are

$$\frac{ds}{dt} = v_\parallel, \tag{3-1}$$

$$\frac{dv_\parallel}{dt} = -\Omega \frac{B^w}{B} v_\perp \cos\psi - \frac{1}{2}\frac{v_\perp^2}{B}\frac{\partial B}{\partial s}, \tag{3-2}$$

$$\frac{dv_\perp}{dt} = (v_\parallel - \frac{\omega}{k})\Omega \frac{B^w}{B}\cos\psi + \frac{1}{2}\frac{v_\parallel v_\perp}{B}\frac{\partial B}{\partial s}, \tag{3-3}$$

$$\frac{d\phi}{dt} = -\frac{(v_\parallel - \omega/k)}{v_\perp}\Omega \frac{B^w}{B}\sin\psi + \Omega, \tag{3-4}$$

where B^w is the slowly varying wave magnetic field amplitude which is related to the electric field amplitude, $E_T A$, of eq.(2-12) by

$$B^w = \frac{ck}{\omega} E_T A. \tag{3-5}$$

The phase, ψ , in equations (3-1) to (3-4) gives the phase of a particle with respect to the wave and is expressed as,

$$\psi = \psi_w + \varphi + \phi, \tag{3-6}$$

where ϕ is the particle's gyrophase angle. Equation (3-4) may be expressed in terms of the phase ψ,

$$\begin{aligned}\frac{d\psi}{dt} &= \frac{ds}{dt}\frac{\partial\psi_w}{\partial s} + \frac{\partial\psi_w}{\partial t} + \frac{d\phi}{dt} + \frac{d\varphi}{dt} \\ &= -\frac{(v_\parallel - \omega/k)}{v_\perp}\Omega\frac{B^w}{B}\sin\psi + kv_\parallel - \omega + \Omega. \end{aligned} \tag{3-7}$$

The frequency, ω, in eq.(3-7) includes the contribution from the slowly varying phase change, $\partial\varphi/\partial t$, driven by the nonlinear current.

The emission process occurs in a region near the magnetic equator where the equilibrium field strength is taken to be[29,33]

$$B = B_0(1 + \frac{s^2}{L^2}), \tag{3-8}$$

and the scale length, L, ignoring any corrections[49,60] to the dipole[24] field, is expressed in terms of the field line l number and earth radius, R_E, as[34]

$$L = \frac{\sqrt{2}}{3} l R_E. \tag{3-9}$$

To develop an asymptotic theory for the orbits note that eq.(3-7) can be written

$$\frac{d\psi}{dt} = kv_\parallel - \omega + \Omega + \mathcal{O}(\varepsilon^2). \tag{3-10}$$

The correction term in eq.(3-10) is much higher order than we will work to and can be ignored[33,40,49] henceforth. Orbital behavior similar to trapping occurs near the equator where the gradient terms are small. Without the gradient terms the trapping oscillations are evident from eqs.(3-2) and (3-10), giving a trapping frequency, $\omega_{tr} = \sqrt{\Omega k v_\perp B^w/B}$. Particles with parallel velocities on the order of

$$V_R \equiv (\omega - \Omega)/k = V_R(s,t), \tag{3-11}$$

are resonant and stay in nearly constant phase with respect to the wave[29]. It is then convenient to define a new velocity variable

$$v = v_\parallel - V_R, \tag{3-12}$$

anticipating that $v/V_R \ll 1$.

In terms of this new variable the equations of motion become,

$$\frac{ds}{dt} = V_R + v, \tag{3-13}$$

$$\frac{dv}{dt} = -v_\perp \Omega \frac{B_w}{B} \cos\psi - \frac{1}{2} v_\perp^2 \frac{1}{B} \frac{\partial B}{\partial s} - V_R \frac{\partial V_R}{\partial s} - v \frac{\partial V_R}{\partial s} - \frac{1}{k} \dot{\omega} (1 + \frac{\Omega}{2\omega}), \tag{3-14}$$

where the last term arises from evaluating

$$\dot{\omega} \frac{\partial V_R}{\partial \omega} = \frac{\dot{\omega}}{k} - \frac{\omega - \Omega}{k^2} \frac{\partial k}{\partial \omega} \dot{\omega}. \tag{3-15}$$

The time derivative of ω is $\dot{\omega} = (\frac{\partial}{\partial t} + V_R \frac{\partial}{\partial s})\omega$. The remaining equations are,

$$\frac{dv_\perp}{dt} = -(\Omega/k - v)\Omega \frac{B_w}{B} \cos\psi + \frac{1}{2} v_\perp (V_R + v) \frac{1}{B} \frac{\partial B}{\partial s}, \tag{3-16}$$

$$\frac{d\psi}{dt} = kv + \mathcal{O}(\varepsilon^2). \tag{3-17}$$

The basic velocity scale, V_s, is set by the resonance condition. Since frequencies are comparable to the gyrofrequency in the triggering problem, actually $\omega \sim \Omega/2$, one has $V_R \sim \Omega/k$. From the whistler dispersion relation for frequencies near Ω_{ce} the wavelength is of the order of the collisionless skin depth, or $k \sim \omega_{pe}/c$. Thus we take the velocity scale to be,

$$V_s \equiv c \frac{\Omega}{\omega_{pe}}. \tag{3-18}$$

It turns out, as will be seen shortly, that the perpendicular velocities for particles subject to trapping are of the same order[46] so that V_s characterizes all velocity directions.

The time scale is set by the trapping period which, using $v_\perp \sim V_s$ and $k \sim \omega_{pe}/c$, implies a frequency scale,

$$\omega_s \sim \Omega \sqrt{B_w/B}. \tag{3-19}$$

Now we can define a smallness parameter, ε, as

$$\varepsilon \equiv \frac{\omega_{tr}}{\Omega_0} \ll 1, \tag{3-20}$$

indicating at the same time that $B^w/B \sim \varepsilon^2$ as noted above.

Assuming the time scale in equation (3-14) to be the trapping period, the first term on the right hand side of eq.(3-14) implies that

$$\frac{v}{V_R} \sim \frac{\Omega}{kV_R} \frac{\omega_{tr}}{\Omega} \sim \varepsilon. \tag{3-21}$$

To the order we work then, v is always negligible compared to V_R . The fourth term on the right hand side of eq.(3-14) my be dropped.

The asymptotic ordering is determined in three steps. First note that for trapping and entrapping and detrapping to all occur, the wave and inhomogeneity terms must be comparable. The terms on the right hand side of eq.(3-14) scale respectively like (dropping the fourth),

$$v_\perp \Omega \frac{B_w}{B} \sim \frac{v_\perp^2 s}{L^2} \sim v_\parallel \frac{\Omega s}{kL^2} \sim \frac{\dot{\omega}}{k} \qquad (3-22)$$

Taking the velocities of order V_s, eq.(3-22) essentially determines s to be of order s_o, where,

$$\frac{s_o}{L} \sim \frac{B_w}{B} \frac{\omega_{pe} L}{c}, \qquad (3-23)$$

gives the length of the *interaction region*[29,36] in which trapping can occur. Also the magnitude of frequency changes as seen by the particles, $\dot{\omega}$, is bounded by $\dot{\omega} < \Omega^2 B_w/B$.

Secondly, we want the s motion along the field line to be on a slower time scale than trapping so that s will vary adiabatically while the trapping oscillations occur. This is the condition that many trapping periods[34] span the interaction region. Therefore, we require $\dot{s}/s_o \sim V_s/s_o \sim \epsilon^\alpha \omega_{tr}$, where $0 \leq \alpha \leq 1$ remains to be determined. This implies,

$$(\frac{c}{\omega_{pe} L})^2 (\frac{B}{B_w})^{3/2} \sim \varepsilon^\alpha. \qquad (3-24)$$

Satisfying condition (3-24) for some α, is the key assumption in the theory. This requires, with $(B_w/B)^{3/2} > (c/\omega_{pe}L)^2$, that the wave field exceeds the critical value for trapping over a full period. A more precise rendering of this condition, and its relation to observations, is given in equation (1-4). Although we will stipulate a third condition below that will uniquely determine α and relate the scale length, L, and wave field, B_w, this third condition is largely a matter of convenience. A very similar asymptotic theory would be possible without the third condition. It would just contain more complex s dependence in the inhomogeneity terms.

In addition to the explicit inhomogeneity terms involving spatial derivatives in eqs.(3-13) to (3-17), there is considerable s dependence due to $\Omega(s)$ and $k(s)$. These effects are corrections of order $(s/L)^2$ as compared to unity. It is convenient, as a third condition, to have these variations enter on the next slower time scale, $\varepsilon^{2\alpha}$,thus

$$\left(\frac{s_o}{L}\right)^2 \sim (\frac{B_w}{B})^2 (\frac{\omega_{pe} L}{c})^2 \sim \varepsilon^{2\alpha}. \qquad (3-25)$$

Using equations (3-24) and (3-25) it follows that,

$$\frac{c}{\omega_{pe}L} \sim (\frac{B_w}{B})^{5/6}, \qquad (3-26)$$

and,

$$\alpha = \frac{1}{3}, \qquad (3-27)$$

which completes the ordering by expressing all the small parameters in terms of $\varepsilon^{1/3}$. The time scale $\sim \varepsilon^{-1/3}$ covers the motion of the resonant electrons completely through the interaction region.

For conditions at the edge of the plasmasphere[51], $l \sim 4, n \sim 400\ cm^{-3}$, one has $\varepsilon^{1/3} \sim .15$ which implies a nominal interaction length of 7 trapping periods. Note also that as B_w increases, the number of trapping oscillations increases and condition (3-24) gets stronger even though in the formal theory $\varepsilon^{1/3}$ is larger. The asymptotic ordering breaks down at larger B_w values due to the third condition chosen largely to streamline the ordering and to eliminate some of the messy s dependence. Paradoxically, the validity of an asymptotic treatment of the orbits at larger B_w is actually improved.

The equations for the orbits correct to order $\varepsilon^{1/3}$ are,

$$\frac{ds}{dt} = V_R, \qquad (3-28)$$

$$\frac{dv}{dt} = -v_\perp \frac{B_w}{B}\Omega \cos\psi - s\left[\frac{v_\perp^2}{L^2} - V_R\frac{\Omega}{kL^2}\left(3 - 2\frac{L^2}{L_n^2}\left(1 - \frac{\omega}{\Omega}\right)\right)\right] - \frac{\dot{\omega}(1+\Omega/2\omega)}{k}, \qquad (3-29)$$

$$\frac{d\psi}{dt} = kv, \qquad (3-30)$$

where the perpendicular velocity changes are higher order[30-37,40]. All quantities such as Ω , k, and V_R can be evaluated at the equator on account of eq.(3-25). The inhomogeneity term in eq.(3-29) has been evaluated expressing the wave number derivatives in terms of the density gradient where the parameter L_n is defined through the expression for the cold electron density[33],

$$n(s) = n_o\left(1 + \frac{s^2}{L_n^2}\right). \qquad (3-31)$$

In the diffusive equilibrium model[40,61], L/L_n is very small, but we retain the term here for generality. The equatorial plasma density is given[29,40,62] in terms of the l-shell number by $n_o(l) = 4000exp(2-l)$. Note that the amplitude, A, and frequency ω in eq.(3-5) contain s dependences on the scale of the interaction region, $\epsilon^{1/3}$, that have not been denoted explicitly.

The perpendicular velocity is constant to the order we work in the trapping dynamics. However, this small change in perpendicular velocity, $dv_\perp/dt \sim \epsilon$, is required for the calculation of the current. To leading order[49],

$$\frac{d}{dt}\mu = \frac{d}{dt}\left(\tfrac{1}{2}\frac{v_\perp^2}{B}\right) = \left(\frac{\partial}{\partial t} + V_R\frac{\partial}{\partial s}\right)\tfrac{1}{2}\frac{v_\perp^2}{B} = -\frac{v_\perp}{B}\frac{\Omega^2}{k}\frac{B_w}{B}\cos\psi, \qquad (3-32)$$

where, $\mu = \frac{1}{2}v_\perp^2/B$, is the magnetic moment, an adiabatic invariant in the absence of the wave fields. In here equatorial values can be taken since corrections from $B = B(s)$ are of order $s^2/L^2 \sim \epsilon^{2/3}$ higher and, therefore, negligible in the present ordering scheme. That is, we may take $v_\perp \simeq const$ as far as the trapping dynamics are concerned. The same holds for the calculation of the leading order change in μ.The $v_\perp$ on the right hand side of eq.(3-32) may be taken to be constant. In what follows, we will regard $v_\perp$ in the driving terms as a constant (essentially the equatorial value), and compute the wave driven changes in μ that create the current.

It will be convenient for the remainder of this paper to work with dimensionless equations. The velocity scale is given by V_s, eq.(3-18), using equatorial values. The frequency scale is given by ω_s (eq.(3-19)) using the field of the triggering wave. Expressed in terms of the electric field strength, the frequency scale is,

$$\omega_s \equiv \sqrt{\Omega\omega_{pe}\frac{E_T}{B}}, \qquad (3-33)$$

where again, equatorial values are implied. For monochromatic triggering signals, one can use,

$$\frac{E_T}{B} = \frac{B_T}{B}\frac{\Omega}{\omega_{pe}}\frac{\omega_o}{\Omega}\sqrt{\frac{\Omega}{\omega_o}-1}, \qquad (3-34)$$

where ω_o is the triggering frequency.

Instead of the deviation v of the parallel velocity from the resonance velocity it is more convenient to use the frequency u defined by $kv \equiv u$ in eq.(3-29) and to scale this to ω_s. This amplifies the small velocity perturbations, v, to be of order unity and sets their scale to be much smaller than V_s. By the same token we scale $\dot{\omega}$ by ω_s^2 in the dimensionless equations, which then become,

$$\frac{ds}{dt} = V_R = -\frac{\omega}{\Omega}\left(\frac{\Omega}{\omega}-1\right)^{3/2}, \qquad (3-35)$$

$$\begin{aligned}\frac{du}{dt} &= -\frac{v_\perp A}{1-\omega/\Omega}\cos\psi - sS'(v_\perp,\omega) - \dot{\omega}T, \\ &\equiv -\frac{v_\perp A}{1-\omega/\Omega}\cos\psi - S \qquad (3-36)\end{aligned}$$

$$\frac{d\psi}{dt} = u, \tag{3-37}$$

where S' has the form,

$$S' = Cv_\perp^2 + D. \tag{3-38}$$

The quantity $S = S's + T\dot{\omega}$ has been termed the inhomogeneity factor[36,40,46-49] and was written in this form by Nunn[33]. The coefficients, C, D, and T, are,

$$C = \frac{V_s^2}{\omega_s^2 L^2}\sqrt{\frac{B}{E_T}\frac{\Omega}{\omega_{pe}}}\frac{1}{\sqrt{\frac{\Omega}{\omega}-1}} \equiv \frac{C_o}{\sqrt{\frac{\Omega}{\omega}-1}}, \tag{3-39}$$

$$\frac{D}{C} = \frac{\omega}{\Omega}(\frac{\Omega}{\omega}-1)^2(3-2\frac{L^2}{L_n^2}(1-\frac{\omega}{\Omega})), \tag{3-40}$$

$$T = 1 + \frac{\Omega}{2\omega} \quad . \tag{3-41}$$

The magnetic moment or perpendicular velocity change can be found from,

$$\frac{d\mu}{dt} = -v_\perp \frac{\omega_s}{\Omega}\frac{\Omega}{\omega}A\cos\psi, \tag{3-42}$$

or,

$$\frac{dv_\perp}{dt} = -\frac{\omega_s}{\Omega}\frac{\Omega}{\omega}A\cos\psi, \tag{3-43}$$

where the second form expresses the change in the equatorial value, neglecting the order $\sim \epsilon^{2/3}$ changes arizing from the adiabatic variation of the perpendicular velocity along the inhomogeneous field line.

Note that C_o depends on the inhomogeneity scale length, L, and wave magnetic field, B_T, such that, $C_o \propto L^{-2}B_T^{-3/2}$. Thus, recalling (3-24), $C_o \ll 1$ is the primary condition for validity of the asymptotic theory. Since $S \sim 1$, this implies $s \gg 1$, which is the dimensionless form of the condition of many trapping periods.

B. Perturbation Theory and Adiabatic Invariant for Trapping

For known functions of amplitude, $A(s,t)$, and frequency, $\omega(s,t)$, equation (3-35) may be integrated to give the arc length as an explicit function of the time along the orbit. This allows the inhomogeneity parameter, S, in eq.(3-36), to be evaluated as an explicit function of time. We can then combine eqs.(3-35) and (3-36) to obtain[33-37,40]

$$\frac{d^2\psi}{dt^2} + \frac{v_\perp A}{1-\omega/\Omega}\cos\psi = -S. \tag{3-44}$$

There exist bounded oscillatory solutions to this equation as long as the inhomogeneity parameter on the right-hand side satisfies,

$$\frac{|S|\,(1-\omega/\Omega)}{v_\perp A} \equiv |Q| \leq 1, \qquad (3-45)$$

assuming for now that the frequency stays constant. Equation (3-45) is called the trapping condition[28-37,40,42-44,47,50,52,53,55-57]. The rescaled inhomogeneity parameter, $Q \equiv S(1-\omega/\Omega)/(v_\perp A)$, has been defined here for convenience. It will reappear frequently in the development of the currents in the next section.

This equation can be solved by an expansion in powers of $\varepsilon^{1/3}$ using the method of multiple time scales[63,64],

$$\psi = P_o + \psi_1 + \psi_2 + \cdots \qquad (3-46)$$

$$S = S_0 + S_2 + \cdots \qquad (3-47)$$

$$\frac{d}{dt} = \frac{\partial}{\partial t_0} + \frac{\partial}{\partial t_1} + \frac{\partial}{\partial t_2} + \cdots \qquad (3-48)$$

Then

$$\frac{d^2\psi}{dt^2} = \frac{\partial^2 P_o}{\partial t_0^2} + \varepsilon^{1/3}\left(\frac{\partial^2\psi_1}{\partial t_0^2} + 2\frac{\partial^2 P_o}{\partial t_0 \partial t_1}\right)$$

$$+ \quad \varepsilon^{2/3}\left(\frac{\partial^2\psi_2}{\partial t_0^2} + 2\frac{\partial^2\psi_1}{\partial t_0 \partial t_1} + 2\frac{\partial^2 P_o}{\partial t_0 \partial t_2} + \frac{\partial^2 P_o}{\partial t_1^2}\right) + \cdots \qquad (3-49)$$

and

$$\cos\psi = (\cos P_o) - (\psi_1 \sin P_o) - \left(\tfrac{1}{2}\psi_1^2 \cos P_o + \psi_2 \sin P_o\right) + \cdots \qquad (3-50)$$

with corrections to S coming in at second order by virtue of the ordering, eq.(3-25). Therefore, the stable phase, P_o, about which the trapped particles oscillate, is a function of S and does not change on the fast time scale,

$$\frac{\partial P_o}{\partial t_0} = \frac{\partial S_0}{\partial t_0} = 0. \qquad (3-51)$$

Using these expansions in eq.(3-44), the leading order is,

$$\frac{v_\perp A}{1-\omega/\Omega}\cos P_o + S_o = 0, \qquad (3-52)$$

yielding

$$P_o = P_o\big(s(t)\big) = \cos^{-1}\Big(-\frac{S(1-\omega/\Omega)}{v_\perp A}\Big) = \cos^{-1}(-Q). \qquad (3-53)$$

To next order one finds,

$$\frac{\partial^2}{\partial t_0^2}\psi_1 + \frac{v_\perp A}{(1-\omega/\Omega)}\sin(-P_o) \quad \psi_1 = 0, \tag{3-54}$$

which is an oscillator equation with oscillation frequency,

$$\omega_0 = \sqrt{\frac{v_\perp A \sin(-P_o)}{1-\omega/\Omega}} = \sqrt{\frac{v_\perp A}{1-\omega/\Omega}}\left(1-Q^2\right)^{1/4}. \tag{3-55}$$

Thus ψ_1 becomes,

$$\psi_1 = \delta\psi(t_1, t_2, \cdots) \quad \sin\phi(t_0, t_1, t_2, \cdots) \tag{3-56}$$

where

$$\frac{\partial\phi}{\partial t_0} = \omega_0. \tag{3-57}$$

Since ϕ is inherently secular on the fast time scale, one must compute $d\phi/dt$ to requisite order to evaluate ϕ. To find $\partial\phi/\partial t_1$ the next equation in the expansion hierarchy is needed. It reads

$$\frac{\partial^2\psi_2}{\partial t_0^2} + \omega_0^2\psi_2 = -2\frac{\partial^2\psi_1}{\partial t_0\partial t_1} - 2\frac{\partial^2 P_o}{\partial t_0\partial t_2} - \frac{\partial^2 P_o}{\partial t_1^2} + \frac{1}{2}\psi_1^2\frac{v_\perp A}{1-\omega/\Omega}\cos P_o - S_2\,. \tag{3-58}$$

The objective is to eliminate secularities of ψ_2 on the fast time-scale. From equation (3-51) $\partial P_o/\partial t_0$ vanishes, thus eliminating the second term on the right-hand side of equation (3-58). The third term cannot drive the left-hand oscillator at frequency ω_0. The fourth term,

$$\tfrac{1}{2}(\cos P_o)\delta\psi^2\sin^2(\omega_0 t + \cdots) = \frac{1}{4}\delta\psi^2(\cos P_o)\left[1-\cos(2\omega_0 t + \cdots)\right]$$

contains second harmonic time dependence and cannot produce secularities either. It is then left to require that,

$$\frac{\partial^2\psi_1}{\partial t_1\partial t_0} = \frac{\partial}{\partial t_1}\left[\,(\delta\psi\omega_0)\cos\phi\right] = \cos\phi\frac{\partial}{\partial t_1}(\delta\psi\omega_0) - \delta\psi\omega_0\sin\phi\frac{\partial\phi}{\partial t_1} \tag{3-59}$$

contain no harmonic time dependence at frequency, ω_o, which would lead to a secularity in ψ_2. This will be guaranteed under the following two conditions,

$$\frac{\partial}{\partial t_1}\delta\psi\omega_0 = 0 \tag{3-60}$$

and

$$\frac{\partial\phi}{\partial t_1} = 0 \tag{3-61}$$

Therefore, the combination $\delta\psi\omega_0$, the amplitude of trapping oscillations in phase ψ times the frequency is constant on the slow time-scale. The orbits during trapping can now be evaluated. These will be accurate through the $\varepsilon^{-1/3}$ time scale and are, therefore, valid during all of the transition of the interaction region from entrapping through detrapping. From eqs.(3-57) and (3-61), ϕ can be obtained as,

$$\phi = \int dt \sqrt{\frac{v_\perp A(s(t),t)\sin(-P_o(s(t)))}{1-\omega(s(t),t)/\Omega}}. \qquad (3-62)$$

It follows that the particle's phase, ψ, is,

$$\psi = P_o + \delta\psi \sin\phi, \qquad (3-63)$$

where,

$$\delta\psi\omega_o = const \equiv \delta v \ , \qquad (3-64)$$

is an adiabatic invariant as noted previously in Refs.34 and 40.

The parallel velocity perturbation can be written, from eq.(3-37) and (3-64), as

$$u = \dot{P}_o + \delta v \cos\phi(t), \qquad (3-65)$$

which makes use of the adiabatic invariant. The time rate of change of the center of oscillation[30,33,44] P_o is given by

$$\dot{P}_o = \frac{\frac{\partial Q}{\partial S} S' V_R}{\sqrt{1-Q^2}} = \frac{\partial P_o}{\partial t_1}, \qquad (3-66)$$

which completes the analytic solution of the trapped electron orbits.

C. Phase Space Analysis and Numerical Orbits

The system of coupled eqs.(3-36) and (3-37), that was just solved, is nearly autonomous because the explicit time dependences in the inhomogeneity S, the amplitude A, and the frequencies ω/Ω are slow. One can, therefore, illustrate the orbital motion which they contain by trajectories in a $u-\psi$ phase space. For this purpose all slow time dependences are considered frozen such that $S, A, v_\perp$ and ω/Ω function as parameters for different phase space realizations. That allows to integrate the system of equations once. The resulting constant of integration is

$$h = \tfrac{1}{2}u^2 + \frac{v_\perp A}{1-\frac{\omega}{\Omega}} \sin\psi + S\psi \qquad (3-67)$$

(see also Refs.[33,40,45,46]). This constant parameterizes the orbits of individual electrons as they move in $u-\psi$ space. From eq.(3-67) the functional form $u(\psi)$ of each trajectory, symmetric about the resonance line, $u=0$, is found to be

$$u=\pm\sqrt{2}\sqrt{h-\sin\psi-Q\psi}, \qquad (3-68)$$

where we have chosen

$$v_{\perp}A/(1-\omega/\Omega)=1, \qquad (3-69)$$

for convenience. A particular choice of h gives one member of the family of orbits that fills the phase plane. This is depicted[33,47] in Figs.3.1-3 which display the relevant phase space near resonance ($u=0$) for three different values of the inhomogeneity parameter, $Q=1$, $Q=0.5$ and $Q=0$. From these figures and eq.(3-68) it can be seen that the range of ψ for each orbit is limited. The restriction is imposed by the radicant in (3-68) which is positive only for $\psi<\psi_a$ when $Q>1$ and $\psi>\psi_a$ when $Q<-1$. The value ψ_a, of course, is determined by eq.(3-68) when $u=0$.

To illustrate the untrapped resonant particle motion downstream of $Q=1$ consider Fig.3.1 . Electrons will flow into the $u-\psi$ window from the top left and exit at the bottom left. Upstream of $Q=-1$ (not shown explicitly) phase space looks as if turned around by 180^o, Electrons enter from the bottom right and disappear to the top right. These orbits, for large inhomogeneities, are essentially those employed in a linear theory of the current.

Small inhomogeneity, $|Q|<1$, produces an additional class of trajectories, called trapped orbits, see Fig.3.2 . In this case eq.(3-68) has three solutions, ψ_a,ψ_b,ψ_c, for any given h and $u=0$. A particle that starts with ψ between ψ_a and ψ_b gyrates clockwise about P_o. For an initial $\psi\leq\psi_c$ at $Q<0$ the electron will not become trapped and hence will continue on a slightly perturbed adiabatic orbit after passing through resonance. Electrons with a given value h can not exist in between ψ_b and ψ_c nor can they achieve larger (smaller) values than ψ_a on the right (left) side of P_o for $Q>0(Q<0)$.

One critical point of the system of eqs.(3-36) and (3-37) is the center or o-point, P_o, defined by $\cos\psi_x=0$, $u=0$, $\sin\psi_x<0$. The other critical point, in a given 2π range of ψ, is a saddle or x-point, defined by $\cos\psi_x=0$, $u=0$, $\sin\psi_x>0$. Associated with the latter is a special orbit, with

$$h_x=\sin\psi_x+Q\psi_x, \qquad (3-70)$$

whose two intersection points with the resonance axis, ψ_b and ψ_c, coincide. This orbit is called the separatrix. It's circular portion separates the trapped resonant particles

inside the vortex about P_o from the untrapped resonant particles. The open ended branch associated with ψ_c splits the untrapped resonant electrons into two groups, those which pass through resonance before ψ_x and those which have to wind around the trapping vortex in order to cross the resonance axis.

The electrons inside the separatrix spend many trapping periods in resonance with the wave at an average phase of $\psi = P_o$. According to eq.(3-42) they experience a nearly constant acceleration of magnetic moment, while their parallel velocity follows the resonance velocity, not the adiabatic orbit $v_{\|} = \sqrt{2(E - \mu B)/m}$. The passing electrons, by contrast, resonate for roughly one trapping period after which their phase quickly increases. This phase mixing leaves little net change in the magnetic moment of individual electrons.

The size of the trapping vortex can be expressed in terms of the height Δu of the separatrix,

$$\Delta u = \sqrt{\frac{2v_{\perp}A}{1 - \frac{\omega}{\Omega}}}\sqrt{\sin\psi_x - \sin P_o + Q(\psi_x - P_o)}. \qquad (3-71)$$

See also eq.(4-15) in the next Section. Note also the overall nonuniform distribution of orbits. Specific nomenclature for this was introduced in Ref.47.

At the equator, $Q = 0$, the separatrix stretches over the full 2π range in ψ (see Fig.3.3). This point represents to the homogeneous magnetic field case where all resonant electrons are trapped at infinitesimal amplitude. Because of the parallel motion of the electrons, which changes Q, this isolated point is of no practical significance. At every other point along the field line the inhomogeneity requires a finite amplitudes, eq.(1-4), for recognizable trapping to occur.

When Q is not frozen during the electron's motion near the resonance line in $u - \psi$ phase space, the separatrix can be crossed. This generates a qualitatively different class of orbits , although, it hardly affects the appearance of phase space at any instant in time. These orbits can now enter and leave the interior at the x-point where their orbital speed ($\dot{u}$ and $\dot{\psi}$) becomes very small. While they stagnate, near the x-point, the virtual separatrix crosses their location. This process is called entrapping. Entrapping of particles inflates the trapping vortex downstream and deflates it upstream in the reverse manner. Notice that only a small sliver of phase space close to the separatrix[40] undergoes in succession entrapping downstream, trapping oscillations about P_o while crossing the equator, and detrapping upstream. The center of trapping oscillations also migrates in time. Its location depends only on the inhomogeneity parameter Q. Starting at $-\pi$ for $Q = 1$, P_o reaches $-\frac{1}{2}\pi$ for $Q = 0$ and disappears at $\psi = 0$ for $Q = -1$. The average position of the trapped

particles, which is P_o, controls the energy transfer (through eq.(3-42)) to the wave and in turn to the nonlinear currents.

The chain of events entrapping, trapping and detrapping is shown in Figs.3.4-6 for one electron. The parameters used in the Runge-Kutta integration for both figures are exactly the same as in the faller of section VII. See there for details. Figure 3.4 shows the whole path in $u - \psi$ phase space of a single electron for the duration of entrapping, trapping and detrapping. It makes the slow migration of the orbit center point P_o. clearly visible. Figure 3.5 shows $u(t)$ (solid line) and $\psi(t)$ (broken line) separately. An amplitude of $A = 3$ in Fig.3.4 and 3.5 leads to $6\frac{1}{2}$ trapping oscillations. Notice the remarkable constancy of the amplitude in u throughout the trapping state as expected from the adiabatic invariant eq.(3-65). Figure 3.6 shows the equivalent of Fig.3.4 for the triggering amplitude $A = 1$. The number of trapping oscillations in this particular case is small. This reflects the conditions of low magnetospheric activity or a weak input signal which are known to lead to falling emissions.

IV. The Non Linear Current

Observed emissions satisfy the general requirements of WKB in that the propagation characteristics of the waves are linear[33] (due to the cold electrons). The wave length is the shortest spatial scale and the wave period is smaller than the time scale of amplitude evolution. We follow the usual development[53], but include in the first order current a general non-linear dependence on the complex wave amplitude.

Defining the real and imaginary parts of the non-linear current as,

$$I_R = Re\left\{ \frac{4\pi e^{-i(\psi_w+\varphi)}\mathbf{e}_1^* \cdot \mathbf{J}_{NL}}{(\omega\partial\epsilon/\partial\omega)\omega_s E_T} \right\} \qquad (2-14)$$

and,

$$I_I = Im\left\{ \frac{4\pi e^{-i(\psi_w+\varphi)}\mathbf{e}_1^* \cdot \mathbf{J}_{NL}}{(\omega\partial\epsilon/\partial\omega)\omega_s E_T} \right\} \qquad (2-15)$$

gives the dimensionless wave equations

$$\left(\frac{\partial}{\partial t} + \frac{v_g}{V_s}\frac{\partial}{\partial s}\right) A = -I_R \qquad (2-16)$$

and,

$$\left(\frac{\partial}{\partial t} + \frac{v_g}{V_s}\frac{\partial}{\partial s}\right) \varphi = -I_I/A \qquad (2-17)$$

which are in form similar to wave equations in References [31,33,45].

Note that the slowly varying wave phase φ is included with ψ_w in computing the non-linear current, so that frequency shifts, $\delta\omega = -\partial\varphi/\partial t$, away from the triggering frequency, $\omega = -\partial\psi_w/\partial t$, are included in the non-linear current.

With the knowledge of the response of single electrons subject to a narrowband Whistler signal as described in the previous section one can generate the orbital characteristics and construct the nonlinear current. The current components required are indicated in equations (2-16) and (2-17), which single out the $\mathbf{e}_1^* \cdot \mathbf{v} = v_\perp e^{-i\phi}$ component. The complex dimensionless non-linear current is given as,

$$I_{NL} = I_R + iI_I = \frac{4\pi e^{-i(\psi_w+\varphi)}\mathbf{e}_1^* \cdot \mathbf{J}_{NL}}{(\omega\partial\epsilon_1/\partial\omega)\omega_s E_T}. \qquad (4-1)$$

Thus when the velocity moment of the distribution function, f, required for the current is computed we have,

$$I_{NL} = -\frac{\omega_{pe}^2}{(\omega\partial\epsilon_1/\partial\omega)}\frac{B}{c\Omega}\frac{V_s}{E_T\omega_s}\int d^3v v_\perp e^{-i\psi} F. \qquad (4-2)$$

The normalization $f = nF$ is used in equation (4-2) to explicitly display the ambient plasma density, leaving F normalized to unity. Also the velocity space in eq.(4-2) is dimensionless, scaled to V_s as in the previous section. Since the velocity integrals are taken at a fixed position s and time t the angular integral in eqn.(4-2) is taken over ψ instead of the original ϕ (see eq.(3-6)). The expression for the wave energy is,

$$\omega \partial \epsilon_1 / \partial \omega = \frac{\omega_{pe}^2}{\Omega^2} \frac{\Omega}{\omega} \frac{1}{(1 - \frac{\omega}{\Omega})^2}. \qquad (4-3)$$

To conform with the scalings of section III, we rescale the parallel velocity in the differential to u, and write the differential in terms of ψ and the magnetic moment, μ, giving,

$$d^3v = \frac{\omega_s}{\Omega} \sqrt{\frac{\Omega}{\omega} - 1} B du d\psi d\mu. \qquad (4-4)$$

The current then becomes,

$$I_{NL} = -\sqrt{\frac{\omega}{\Omega}} \left(1 - \frac{\omega}{\Omega}\right)^{5/2} \frac{\Omega^2}{\omega_s^2} \int B d\psi du d\mu \sqrt{2\mu B} e^{-i\psi} F. \qquad (4-5)$$

The distribution function F is governed by the Vlasov equation, which advances the system such that phase space volume is conserved. An equivalent description is the constancy of F along particle orbits, i.e. Liouville's theorem[36,65]. Explicitly, the Liouville theorem is,

$$F(v_\parallel, \psi, \mu, t) = F\left(v_{\parallel c}(t_c; u, \psi, \mu, t), \psi_c(t_c; u, \psi, \mu, t), \mu_c(t_c; u, \psi, \mu, t), t_c\right), \quad (4-6)$$

where the subscript c on the right hand side of eq.(4-6) denotes *characteristics*. When t_c is pushed far enough into the past, all particles near the equator at time t will be far away and not interacting strongly with the wave. The distribution then assumes its *equilibrium* form, stationary and independent of phase, ψ . The interaction of the electrons with the wave causes only small fractional changes for both $v_\parallel$ and μ . Therefore, it is convenient to expand about $v_\parallel = V_R$, and the initial $\mu = \mu_c$, giving

$$F(v, \psi, \mu, t) = F(V_R, \mu_c) + v_c \frac{\partial F}{\partial v_\parallel}(V_R, \mu_c) + \Delta\mu \frac{\partial F}{\partial \mu}(V_R, \mu_c). \qquad (4-7)$$

The first term on the right cannot contribute to the current. One can anticipate similarly that circulating particles will be distributed uniformly in phase and will not contribute significantly. The parallel velocity perturbation v_c is of $\mathcal{O}(\epsilon)$, as seen in section

III. The perpendicular velocity perturbation, although changing at the rate ε, is secular. It undergoes monotonic acceleration or deceleration over a period of $\mathcal{O}(\varepsilon)^{-1/3}$ which is the length of time the particle is trapped. This, therefore, is the dominant contribution to the current. Then equation (4-5) becomes to leading order,

$$I_{NL} = -\sqrt{\frac{\omega}{\Omega}}\left(1-\frac{\omega}{\Omega}\right)^{5/2}\frac{\Omega^2}{\omega_s^2}\int B d\psi du d\mu \sqrt{2\mu B}e^{-i\psi}\Delta\mu\frac{\partial F}{\partial\mu} \qquad (4-8)$$

The needed expression for $\Delta\mu$ can be obtained by integrating eqn.(3-42) backward in time along the characteristics[27,33]. However, since the theory pertains to the interaction region, $s^2/L^2 \sim \epsilon^{2/3}$, corrections due to the s dependence of B are negligible, and it is unnecessary to retain them in the current. Accordingly, the form of eq.(3-43), which expresses the change in equatorial $v_\perp$ due to the wave, is sufficient and more convenient to use. Henceforth, $v_\perp$ will be used as the independent variable with the understanding that it refers to the equatorial and not local value. The particle orbits from eq.(3-28), (3-62), and (3-63) give the past history integral for $\Delta v_\perp$ the form

$$\Delta v_\perp = \frac{\omega_s}{\Omega}\frac{\Omega}{\omega}\int_o^\tau d\tau'\, A(s+\tau' V_R, t-\tau') \times \cos\left[P_o + \frac{\delta v}{\omega_o}\sin\left(-\int_o^\tau d\tau'\omega_o + \eta\right)\right], \qquad (4-9)$$

or,

$$\Delta v_\perp = \frac{\omega_s}{\Omega}\frac{\Omega}{\omega}\int_o^\tau d\tau' A \sum_{n=-\infty}^{+\infty}\frac{1}{2}\left[e^{iP_o}J_n(\frac{\delta v}{\omega_o})e^{in\theta(\tau')} + e^{-iP_o}J_n(\frac{\delta v}{\omega_o})e^{-in\theta(\tau')}\right], \qquad (4-10)$$

where $\theta(\tau')$ is the phase of the sine function in eq.(4-10). Recall that these expressions apply only to the trapped phase of the orbits. Thus $e^{in\theta(\tau')}$ is rapidly oscillating on the trapping time scale while ω_o , P_o and A are all varying slowly. Provided, $\varepsilon^{1/3} \ll 1$, only the $n = 0$ terms from the sum survive, leaving

$$\Delta v_\perp = -\frac{\omega_s}{\Omega}\left(1-\frac{\omega}{\Omega}\right)\frac{\Omega}{\omega}\frac{1}{v_\perp}\int_o^\tau d\tau'\, S\, J_o\left(\sqrt{\frac{(u-\partial P_o}{\partial t_1)^2/\omega_o^2} + (\psi - P_o)^2}\right), \qquad (4-11)$$

where we have used $\cos P_o = -S(1-\omega/\Omega)/v_\perp A$. Note that the untrapped particles will not contribute to the current to leading order in $\varepsilon^{1/3}$. Except during a time[40] period

of $\mathcal{O}(1)$ when they are near the trapping boundary, the untrapped particles undergo a perturbation independent of phase. Or, rather, the phase dependence mixes away[44] on a very fast time scale relative to that of the integral (4-11). In contrast the trapped particles contribute to the current for a time of $\mathcal{O}(\varepsilon)^{-1/3}$, or for all the time they are trapped[40,44]. By the same argument, the details of the trapping boundary - where particles reside for a time of order one while passing to and from trapped space - are not important either.

As the integral for the current, using eq.(4-11) in (4-8), one obtains to leading order

$$I_{NL} = \sqrt{\frac{\Omega}{\omega}}\left(1-\frac{\omega}{\Omega}\right)^{7/2}\frac{\Omega}{\omega_s}\int_{tr} dv_\perp\, v_\perp du\, d\psi\, e^{-i\psi}\int_o^\tau d\tau'\, S\, J_o \frac{\partial F}{\partial v_\perp}. \qquad (4-12)$$

The argument of the Bessel function J_o is the same as in eqn.(4-11) and the integration reaches over all trapped space.

We now replace the argument of the Bessel function by the local ($\tau' = 0$) values. Then using cylindrical coordinates in u, ψ space

$$\begin{aligned} u^2 + \omega_o^2(\psi - P_o)^2 &= r^2 \\ u &= r\,\sin\theta \\ \psi - P_o &= \frac{r}{\omega_o}\,\cos\theta \\ du d\psi &= \frac{1}{\omega_o} dr d\theta r, \end{aligned} \qquad (4-13)$$

equation (4-12) becomes

$$\begin{aligned} I_{NL} = \sqrt{\frac{\Omega}{\omega}}\left(1-\frac{\omega}{\Omega}\right)^{7/2}\frac{\Omega}{\omega_s}\int_{tr} dv_\perp\, v_\perp \int_o^{2\pi} d\theta \frac{1}{\omega_o} \\ \times \int_o^{\Delta u} dr r e^{-iP_o - i\frac{r}{\omega_o}\cos\theta}\int_o^\tau d\tau'\, S\, J_o\left(\frac{r}{\omega_o}\right)\frac{\partial F}{\partial v_\perp}, \end{aligned} \qquad (4-14)$$

where Δu is the width in u of the trapping separatrix given by

$$\Delta u = \sqrt{2}\omega_o\sqrt{1-\frac{Q\cos^{-1}Q}{\sqrt{1-Q^2}}}. \qquad (4-15)$$

Performing the angular integral in (4-14) gives

$$I_{NL} = \sqrt{\frac{\Omega}{\omega}}\left(1-\frac{\omega}{\Omega}\right)^{7/2}\frac{\Omega}{\omega_s}\int_{tr} dv_\perp v_\perp\, e^{-iP_o} 2\pi\omega_o \int_o^{\Delta u/\omega_o} dx\, x\, J_o^2(x)$$

$$\times \int_o^\tau d\tau' \left(S'(s+\tau' V_R) + \dot{\omega} T\right) \frac{\partial F}{\partial v_\perp}. \quad (4-16)$$

Equation (4-16) completes the non-linear theory. Taking real and imaginary parts of I_{NL} to give I_R and I_I , respectively, specifies the currents needed to advance the wave equations (2-16) and (2-17).

First of all, recognize that the Bessel function integral in eq.(4-16) is effectively a trapping volume is phase space, an order unity quantity. It is, therefore, convenient to define a trapping volume,

$$\alpha_v(Q) \equiv 2\pi(1-Q^2)^{1/4} \int_o^{\Delta u/\omega_o} dx x J_o^2(x), \quad (4-17)$$

where part of the oscillation frequency, ω_o, in the integrand of eq.(4-16) has been absorbed into the definition (4-17). The time integral in eq. (4-16) is easily carried out. Expressing P_o in terms of S , $v_\perp$, and A , we then get handy expressions for I_R and I_I ,

$$I_R = -\sqrt{\frac{\Omega}{\omega}}\left(1-\frac{\omega}{\Omega}\right)^3 \frac{\Omega}{\omega_s} A^{1/2} \int_{tr} dv_\perp v_\perp^{3/2} \alpha_v(Q) Q(S\tau - \tfrac{1}{2} V_R S' \tau^2) \frac{\partial F}{\partial v_\perp}, \quad (4-18)$$

and,

$$I_I = \sqrt{\frac{\Omega}{\omega}}\left(1-\frac{\omega}{\Omega}\right)^3 \frac{\Omega}{\omega_s} A^{1/2} \int_{tr} dv_\perp v_\perp^{3/2} \alpha_v(Q) \sqrt{1-Q^2}(S\tau - \tfrac{1}{2} V_R S' \tau^2) \frac{\partial F}{\partial v_\perp}. \quad (4-19)$$

In comparison with this the currents of Nunn's theory[7] appear somewhat similar but are expressed in terms of the vortex phase center, rather than the trapping time, and require parallel velocity gradients in addition with the consequence that only systems with linear instability can cause emissions, in contrast to the findings below.

There remains to determine τ, the time spent trapped. This can be done by propagating the trapping condition along the the particle orbits into the past to determine when the entrapping first occurred. Thus, for τ to be non-zero, the trapping condition,

$$|Q| \equiv \frac{(1-\omega/\Omega)|S'(s+|V_R|\tau) + T\dot{\omega}(s+|V_R|\tau, t-\tau)|}{v_\perp A(s+|V_R|\tau, t-\tau)} < 1, \quad (4-20)$$

must be satisfied. Then τ is the time, into the orbit's past history, that equation(4-20) was first satisfied. That is

$$\frac{v_\perp A(s+|V_R|\tau, t-\tau)}{1-\omega/\Omega} = |S'(s+|V_R|\tau) + T\dot{\omega}(s+|V_R|\tau, t-\tau)|. \quad (4-21)$$

This algorithm for determining τ is not particularly convenient for numerical purposes as it requires retaining lengthy time history data for A and $\dot{\omega}$, and finding roots of potentially very complex functions.

We can develop an alternate procedure for finding τ by noting that eq.(4-21) is invariant under the transformation,

$$\begin{aligned} t &\rightarrow t + \Delta t \\ \tau &\rightarrow \tau + \Delta t \\ s &\rightarrow s - V_R \Delta t. \end{aligned} \qquad (4-22)$$

This means that the root, $\tau = \tau(s,t)$, satisfies the condition,

$$\tau(s,t) = \tau(s + |V_R|\Delta t, t - \Delta t) + \Delta t. \qquad (4-23)$$

This has a clear physical interpretation. A particle trapped at position s and time t has been trapped an additional time, Δt, since being at position $s + |V_R|\Delta t$. One can also form a differential equation from (4-23) by taking the limit $\Delta t, \Delta s \rightarrow 0$, with $\Delta s/(|V_R|\Delta t) = 1$,

$$\frac{\partial \tau}{\partial t} + |V_R|\frac{\partial \tau}{\partial s} = 1. \qquad (4-24)$$

In physical terms, the rate of change of τ with time, along the particle orbit, is one - provided the particle is trapped. Thus (4-24) must be augmented by the condition (4-20). Equation (4-24) advances τ if eq.(4-20) is satisfied. Otherwise τ is zero.

The assumption of many trapping oscillations during trapped state is expressed by the condition[34]

$$\omega_{tr}\tau > 2\pi, \qquad (4-25)$$

which requires a trapping duration τ of at least one trapping period. The smallness of the expansion parameter $\varepsilon^{1/3}$ guarantees the constancy of $A, \omega, \dot{\omega}$ during one trapping oscillation such that eq.(4-25) functions as a limit on the range of perpendicular velocities (see Fig.7.4 and Ref.[19]). In general, for constant $A, \omega, \dot{\omega}$ the interaction region is located between the points, $Q = \pm 1$. Note that a constant $\dot{\omega}$ merely shifts the trapping equator. The length Δs of the interaction region to one side of the equator is given by

$$\frac{2S'\Delta s(1 - \frac{\omega}{\Omega})}{v_\perp A} = \frac{2(Cv_\perp^2 + D)(1 - \frac{\omega}{\Omega})\Delta s}{v_\perp A} = 1 \qquad (4-26)$$

so that $\tau = 2\Delta s/|V_R|$. The condition, (4-25), of trapping for a full period, is then

$$A^3 \geq 4\pi^2 V_s^2 C^2 (1 - \frac{\omega}{\Omega})^3 \frac{(v_\perp^2 + D/C)^2}{v_\perp^3}. \qquad (4-27)$$

Cutoffs to the velocity integrals for the currents (4-18) and (4-19) are obtained from the two real roots of equation (4-27) which is fourth order in $v_\perp$. For large amplitudes the lower cutoff, $v_\perp^-$, is proportional to the inverse of the amplitude ($v_\perp^- \sim A^{-1}$), while the upper cutoff obeys $v_\perp^+ \sim A^3$. This implies a very rapid increase in the number of trapped particles with amplitude[40], one of the nonlinear feedback mechanisms that is critical to the triggering process. There is also a minimum amplitude, A_{MIN}, at which real roots for equation (4-27) exist. This occurs for the velocity

$$v_\perp^0 = \sqrt{\frac{3D}{C}}, \qquad (4-28)$$

(see also Fig.5.1) at which the right hand side of equation (4-27) is a minimum. Evaluating equation (4-27) at $v_\perp^0$ gives,

$$A_{MIN} \equiv 3.75 C_o^{\frac{2}{3}} (1 - \frac{\omega}{\Omega})^2 (\frac{\Omega}{\omega})^{\frac{1}{6}} \left[1 - \frac{2}{3}\frac{L^2}{L_n^2}(1 - \frac{\omega}{\Omega})\right]^{1/6}, \qquad (4-29)$$

which is the trapping threshold, below which the nonlinear currents are effectively zero. Since the equations have been scaled using B_T, the amplitude of the input signal is $A = 1$. Therefore, $A_{MIN} < 1$ is a necessary condition for triggering in the dimensionless picture. In the numerical implementation of the theory the quartic (4-27) is solved to give cutoffs $v_\perp^-$ and $v_\perp^+$, and $A_{MIN} < 1$ is assured by proper choice of the initial conditions.

V. Triggering Mechanism

The purpose of this section is to give the theoretical picture of the triggering of emissions that follows directly from the nonlinear theory developed above. It will be possible to show in simple terms how triggering is related to an inversion in the perpendicular velocity distribution function (although not requiring a distribution that is linearly unstable). It also is possible to see how the occurrence of triggering is a consequence of the length of the input signal and thereby to understand the dot-dash anomaly[13,14]. The discussion of this section will focus on those features of the emission process which can be immediately inferred from the theory. A more detailed discussion of some of the results and explanation of some of the unexpected consequences of the numerical integration will follow in subsequent sections.

The equations of the self-consistent theory are collected here for convenience. First we have the equations for the wave amplitude and phase propagation equations (2-16) and (2-17)

$$\left(\frac{\partial}{\partial t}+\frac{v_g}{V_s}\frac{\partial}{\partial s}\right)A=-I_R \qquad (5-1)$$

and,

$$\left(\frac{\partial}{\partial t}+\frac{v_g}{V_s}\frac{\partial}{\partial s}\right)\varphi=-I_I/A \qquad (5-2)$$

accompanied by equations (4-18) and (4-19) for the nonlinear currents

$$I_R=-\beta A^{1/2}\int_{tr} dv_\perp v_\perp^{3/2}\alpha_v(Q)Q(S\tau-\tfrac{1}{2}V_R S'\tau^2)\frac{\partial F}{\partial v_\perp}, \qquad (5-3)$$

and,

$$I_I=\beta A^{1/2}\int_{tr} dv_\perp v_\perp^{3/2}\alpha_v(Q)\sqrt{1-Q^2}(S\tau-\tfrac{1}{2}V_R S'\tau^2)\frac{\partial F}{\partial v_\perp}, \qquad (5-4)$$

where,

$$\beta=\sqrt{\frac{\Omega}{\omega}}\left(1-\frac{\omega}{\Omega}\right)^3\frac{\Omega}{\omega_s}. \qquad (5-5)$$

The currents contain the trapping volume α_v defined in equation (4-17)

$$\alpha_v(Q)=2\pi(1-Q^2)^{1/4}\int_o^{\Delta u/\omega_o} dx x J_0^2(x), \qquad (5-6)$$

where $\Delta u/\omega_o$ is given in equation (4-15),

$$\frac{\Delta u}{\omega_o} = 2\sqrt{\sqrt{1-Q^2} - Q\cos^{-1}Q}. \qquad (5-7)$$

and the trapping time τ which evolves according to equation (4-24)

$$\frac{\partial \tau}{\partial t} + |V_R|\frac{\partial \tau}{\partial s} = 1, \qquad (5-8)$$

If the trapping condition (4-20),

$$|Q| \equiv \frac{|S|(1-\omega/\Omega)}{v_\perp A} < 1, \qquad (5-9)$$

is satisfied. A cut-off in the perpendicular velocity integrals is implied by the trapping threshold condition, eq.(4-27),

$$A^3 \geq \pi^2 V_R^2 C^2 (1-\frac{\omega}{\Omega})^3 \frac{(v_\perp^2 + D/C)^2}{v_\perp^3}, \qquad (5-10)$$

indicating the existence of at least one trapping oscillation as the resonant electrons pass through the interaction region. These ten equations constitute a highly nonlinear system whose full ramifications can be understood only by numerical integration, to follow in subsequent sections. The present section is devoted to the qualitative aspects of the theory that can be inferred directly from the equations and will allow us to form a simple picture of the triggering process.

Consider a constant amplitude or square wave triggering pulse[30,33,49] of constant frequency approaching the equatorial region from upstream ($-s$). In order for the currents to form, the triggering amplitude must exceed the threshold value for trapping, as indicated in equation (5-10). For amplitudes slightly above this value particles will be trapped downstream (at positive s) within a narrow window in perpendicular velocity space centered on $v_\perp^0 = \sqrt{\frac{3D}{C}}$. The window falls into a region of the distribution function with positive slope. This situation is illustrated in Figure (5.1) for the distribution function

$$F = \Delta e^{-v_\perp^2/v_{th}^2}\left(1 - e^{-v_\perp/v_b}\right). \qquad (5-11)$$

This form of the high energy distribution function underlies all of the subsequent examples.

If the pulse is long enough and spans the equator, the form of the input wave implies that the trapping condition is satisfied, for any perpendicular velocity by eq.(5-10), between two conjugate points, the entrapping point (s_+) and detrapping point (s_-). Both points

in this case would be symmetric about the equator. Since the nonlinear currents are determined by the particle's spatial location and phase space location as expressed by the average phase, P_0, one can think in terms of representative electrons each parameterized by its perpendicular velocity and weighted by the trap size α_v.

The real current integrand as given in equation (5-3) for such a representative electron has the form

$$S(S\tau - \frac{1}{2}|V_R|S'\tau^2)\frac{\partial F}{\partial v_\perp}. \qquad (5-12)$$

When there are no frequency changes ($\dot{\omega} = 0$) the effective inhomogeneity, $S = S's$, is proportional to the arc length since S' is usually a positive constant. The trapping time τ is also linear in the arc length since the resonance velocity is constant to leading order. In the interaction region then the trapping time τ can represented by

$$\tau = \frac{s - s_+}{V_R}. \qquad (5-13)$$

It increases linearly from the detrapping point

$$s_+ = \frac{v_\perp A}{(1-\omega/\Omega)S'}, \qquad (5-14)$$

in the upstream direction. With these two expressions the integrand of the real current in eq.(5-3) takes the form

$$-s(s+s_+)(s-s_+)\left(\frac{S'^2}{2|V_R|}\right)\frac{\partial F}{\partial v_\perp}, \qquad (5-15)$$

which has a cubic dependence on the arc length. This form allows one to understand easily how the supply of free energy in the distribution function ($\partial F/\partial v_\perp > 0$) is related to triggering of emissions. Note that this form exhibits the current zeros at $s = 0, s = s_+, s = -s_+$. Therefore, if $\partial F/\partial v_\perp > 0$ the current amplifies (is negative) between the entrapping point and the equator as well as upstream of $-s_+$ while it damps the wave (positive current) between the equator and $s = -s_+$. In short, one can expect upstream damping and downstream emission. Of course the current is zero downstream of s_+ where no trapped electrons exist. This characteristic waveform is illustrated in Figure 5-2.

The triggering of emissions proceeds as follows. The triggering wave propagates towards the equator from upstream. The first currents which form upstream (when $s_+ < 0$) amplify the front end of the incoming pulse. Once the triggering wave has propagated across the equator ($s_+ > 0$) the upstream current becomes negative and begins to dampen out the remaining incoming portion of the trigger wave. Simultaneously the downstream

waveform amplifies as indicated in Figure (5-2b). As the trailing edge of the morse dash approaches the equatorial region it is damped until all of the upstream portion of the signal is eliminated. Since trapping can occur at zero amplitudes at the equator, the waveform can begin from zero amplitude at the equator[29] and grow to some amplified value downstream. As the signal level grows, the initially narrow window of trapped perpendicular velocities in the unstable portion of the distribution function expands, therewith supplying more current to the amplification process. Provided this current is sufficiently large to offset convection the emission sustains itself. One ends up with a wave train emanating from the equator at zero amplitude and growing to some final value downstream. The input waveform is no longer needed. The self-sustaining emission can grow to a very large amplitude downstream. If the total currents are not sufficiently strong, that is too small in magnitude or spatial extend, the triggering signal will experience transient modifications but ultimately disconnect from the equator and propagate downstream without amplification. The spatial extend of the current depends on the inhomogeneity and the length of the triggering signal. This is why the process exhibits threshold behavior with respect to pulse length, input power, density of tail electrons, and the other parameters. It is clear that reversing the sign of the distribution function slope would eliminate any possibility of triggering, since initially the weak triggering signal would be damped instead of amplified thereby preventing the development of sufficiently strong currents.

As the amplitude grows to a very large value the range of perpendicular velocities, which is allowed by condition (5-10), passes into the stable region of the distribution function, as indicated in Figure (5-1). At first sight this would seem to imply a saturation of the growth process. It turns out, however, that this saturation is only local, as we will discuss in detail along with the rest of the numerical results in Section 7.

VI. Numerical Implementation

This section describes the numerical code developed to solve the equations (5-1) to (5-10) of the self-consistent theory. A discussion will be given of the numerical schemes, their stability criteria, and certain minimal smoothing procedures which are required to render the asymptotic theory numerically well posed.

Consider first, the amplitude equation (5-1). Since it is hyperbolic, the Lax-Wendroff difference scheme[66] would be the immediate choice. However, the nonlinear current driving equation (5-1) invalidates the usual derivation. To adopt the scheme to our purposes we start with the basic idea behind Lax-Wendroff by discretizing equation 5-1 with a forward difference in time, a centered difference in space, and by adding diffusion. Then the amplitude for the next time step is predicted by

$$A_j^{n+1} = A_j^n - \frac{v_g\lambda}{2}\left(A_{j+1}^n - A_{j-1}^n\right) - \Delta t(I_R)_j^n + \frac{\varepsilon\lambda}{\Delta x}\left(A_{j+1}^n - 2A_j^n + A_{j-1}^N\right), \qquad (6-1)$$

here $\lambda = \Delta t/\Delta x$ while ε is the diffusion parameter. The need for diffusion in this scheme is twofold. On the one hand, diffusion is needed for stability in the usual Law-Wendroff scheme. On the other hand, it eliminates grid oscillations that can arise due to sharp transitions or boundaries in the amplitude evolution. The price for adding this numerical dissipation is signal degradation. The proper value for the diffusion coefficient is then found as a trade-off between stability and signal degradation. In Lax-Wendroff one uses $\varepsilon = v_g^2\Delta t/2$ which is the minimum value of the diffusion parameter required for stability.

One can analyze the difference scheme (6-1) for stability in the usual way by examining the behavior of linearized Fourier perturbations $A_j^n = M^n e^{ikx_j}$. Then finds a formula for the amplification coefficient is

$$M = \left(1 - \Delta t\tilde{I}\right) + \mu\lambda\left(cos[k\Delta x] - 1\right) - iv_g\lambda sin[k\Delta x], \qquad (6-2)$$

where

$$\mu = \frac{2\varepsilon}{\Delta x}, \qquad (6-3)$$

and

$$\tilde{I} = \frac{\partial(I_R)_j^n}{\partial A_j^n}. \qquad (6-4)$$

Thus the condition for stability is $||M||^2 < 1$. This implies

$$\tilde{I}\Delta t \ll 1, \qquad \lambda < \frac{\Delta x}{2\varepsilon}, \qquad \varepsilon \geq v_g^2\frac{\Delta t}{2}. \qquad (6-5)$$

To this one should add the requirement that $\Delta t \sim \Delta x^2$ for consistent accuracy, although this latter condition is more stringent than required for stability. The minimum value of ε required for stability is, $\varepsilon = v_g^2 \Delta t/2$, which reduces the scheme to pure Lax-Wendroff with an additional first order term due to the nonlinear current. We sometimes find it convenient to have additional smoothing and allow ε to be variable.

The phase equation (5-2) can be rewritten as

$$\left(\frac{\partial}{\partial t} + \frac{v_g}{V_s}\frac{\partial}{\partial s}\right)\varphi =$$

$$-\dot{\omega}\left(1+\frac{\Omega}{2\omega}\right)\sqrt{\frac{\Omega}{\omega}}\left(1-\frac{\omega}{\Omega}\right)^3 \frac{\Omega}{\omega_s} A^{-1/2} \int dv_\perp v_\perp^{3/2} \alpha_v(Q)\sqrt{1-Q^2}\tau \frac{\partial F}{\partial v_\perp}$$
$$-\sqrt{\frac{\Omega}{\omega}}\left(1-\frac{\omega}{\Omega}\right)^3 \frac{\Omega}{\omega_s} A^{-1/2} \int dv_\perp v_\perp^{3/2} \alpha_v(Q)\sqrt{1-Q^2} S'\left(s\tau - \tfrac{1}{2}V_R\tau^2\right)\frac{\partial F}{\partial v_\perp} \quad (6-6)$$

or more compactly

$$A\left(\frac{\partial}{\partial t} + v_g\frac{\partial}{\partial s}\right)\varphi = -TB\left(\frac{\partial}{\partial t} + V_R\frac{\partial}{\partial s}\right)\delta\omega - E \quad (6-7)$$

where TB is the coefficient of $\dot{\omega}$ in the first term on the right hand side of eq.(6-6) and E represents the second term. (see also eqs.(7-12) through (7-14)). The numerical difficulty associated with the phase equation can be seen rather clearly from equation (6-7). This is a peculiar two-way wave equation which changes its character in response to the variable coefficients B and E. In the initial phases of evolution of a triggered emission the coefficients B and E are zero since there are no currents, and we have a simple wave equation propagating the phase downstream. As the emission develops the coefficients E and B grow very large, and the equation is dominated by propagation upstream of the perturbed frequency. It is non trivial to obtain a stable difference scheme for these two-way propagation characteristics in response to the variable coefficients. Here we will utilize a subsidiary asymptotic limit valid in the interaction region wherein the left hand side of equation (6-7) is neglected. The motivation for this arises out of a similar feature in the amplitude evolution which will be discussed in Section 7. The equation for the change in frequency is merely

$$TB\dot{\omega} = -E \quad (6-8)$$

where $\dot{\omega}$ is the convective derivative following the resonance velocity. The numerical calculations show that the coefficients E and B are very large within the interaction region and

go to zero abruptly at the edges of it. In fact the ratio E/TB needed to evaluate $\dot{\omega}$ can be found quite accurately, simply by evaluating these coefficients at a dominant velocity (e.g. $v_\perp = \sqrt{D/C}$). In this case the integrals defining E and B don't have to be carried out, and we find simply

$$\dot{\omega} = -\frac{D}{T}(2s - V_R\tau) \qquad (6-9)$$

From this expression one can compute the instantaneous change in frequency by integrating along the characteristics of

$$\left(\frac{\partial}{\partial t} + V_R\frac{\partial}{\partial_s}\right) \quad \delta\omega = \dot{\omega} \qquad (6-10)$$

which results in

$$\delta\omega = -\int_{entr}^{detr} \frac{\dot{\omega}}{V_R} ds. \qquad (6-11)$$

Expression (6-10) for $\dot{\omega}$ as well as expression (5-6) for α_v and (5-8) for τ are valid only within the trapping region and go abruptly to zero outside of it. These discontinuities are a natural by-product of the asymptotic theory but present problems for any numerical scheme. To render the asymptotic theory well posed numerically, some minimal smoothing must be introduced. This smoothing is also justified from a physical point of view in that particles take a finite time to become entrapped downstream and subsequently to detrap upstream. It is only in the asymptotic limit that this transition occurs instantaneously. Allowance for the finite times for trapping and detrapping leads one to construct equations valid not only in the trapping region but outside as well. This continuity is needed to ensure a stable numerical transition from one region to the other. The finite time for trapping and detrapping is of order of the trapping period or $1/\omega_{tr} \equiv \nu$. This time varies with velocity $\omega_{tr} \sim \sqrt{v_\perp}$ in a way that is important to include to avoid oversmoothing of the large perpendicular velocity particles (for simplicity we neglect the A and ω dependence of ω_{tr}).

For example, in the case of the trapping volume α_v we utilize the following equation

$$\left(\frac{\partial}{\partial t} + V_R\frac{\partial}{\partial s}\right)\alpha_v' + \nu\alpha_v' = \nu\alpha_v \qquad (6-12),$$

where α_v is given by the eq.(5-6) and α_v' is the desired smoothed trapping volume needed in the numerical prescription. Notice that the decay toward the asymptotic value proceeds along the particle orbits. This will shift and distort somewhat the waveform in the upstream direction. A similar equation will be used to smooth $\dot{\omega}$. Equation (6-12) is

differenced using the Lax-Wendroff type of scheme with additional variable diffusion to eliminate grid oscillations.

$$\begin{aligned}\alpha_j'^{n+1} &= \alpha_j'^n\left(1-\nu\Delta t+\tfrac{1}{2}\nu^2\Delta t^2\right)-\tfrac{1}{2}V_R\lambda\left(1-\nu\Delta t\right)\left(\alpha_{j+1}'^n-\alpha_{j-1}'^n\right)\\ &+\left(\tfrac{1}{2}V_R^2\lambda^2+\varepsilon\lambda/\Delta x\right)\left(\alpha_{j+1}'^n-2\alpha_j'^n+\alpha_{j-1}'^n\right)+\alpha_j^n\left(-\nu\Delta t+\tfrac{1}{2}\nu^2\Delta t^2\right)\\ &+\frac{1}{4}\nu\Delta t\lambda V_R\left(\alpha_{j+1}^n-\alpha_{j-1}^n\right)+\tfrac{1}{2}\nu\Delta t\left(\alpha_j^{n+1}-\alpha_j^n\right) \qquad (6-13)\end{aligned}$$

Fourier stability analysis indicates the following stability criteria

$$\nu\Delta t\ll 1,\quad V_R^2\lambda^2+\frac{2\varepsilon\lambda}{\Delta x}<1,\quad 0<\frac{2\varepsilon\lambda}{\Delta x}<1 \qquad (6-14)$$

A similar problem arises in connection with the τ equation (5-8) which is valid only in the interaction region. This is particularly critical since τ is the principal dynamical quantity and according to (5-8) would jump abruptly from a maximum value near the detrapping point to zero. Making this drop to zero to proceed smoothly corresponds physically to allowance for the finite time of particle detrapping and dephasing. We represent this outside of the interaction region by evolving τ according to the equation

$$\left(\frac{\partial}{\partial t}+V_R\frac{\partial}{\partial s}\right)\tau=-\nu\tau \qquad (6-15)$$

The difference scheme parallels those above, giving

$$\tau_j^{n+1}=\tau_j^n-\frac{V_R\lambda}{2}\left(\tau_{j+1}^n-\tau_{j-1}^n\right)+\left(\tfrac{1}{2}v^2{}_R\lambda^2+\frac{\varepsilon\lambda}{\Delta x}\right)\left(\tau_{j+1}^n-2\tau_j^n+\tau_{j-1}^n\right), \qquad (6-16)$$

which is

$$\begin{aligned}\tau_j^{n+1} &= \tau_j^n\left(1-\nu\Delta t+\tfrac{1}{2}\nu^2\Delta t^2\right)-\frac{1}{2}V_R\lambda\left(1-\nu\Delta t\right)\left(\tau_{j+1}^n-\tau_{j-1}^n\right)\\ &+\left(\tfrac{1}{2}v^2{}_R\lambda^2+\frac{\varepsilon\lambda}{\Delta x}\right)\left(\tau_{j+1}^n-2\tau_j^n+\tau_{j-1}^n\right). \qquad (6-15)\end{aligned}$$

The logic of the marching scheme that evolves the amplitude and the other dynamical quantities in time is based on these difference approximations. Initially a triggering signal of amplitude equal to 1 is propagated into the grid from the upstream side. This is a rounded-off square wave pulse with continuous first derivative. At each time step the trapping condition (4-20), as well as the cut-off condition equation (4-27) (evaluated using the average amplitude over the interaction region) is checked for all perpendicular velocities and grid points. If the particles in question are trapped τ, α_v and $\dot{\omega}$ are stepped using the

above schemes and the real current is accumulated. If the velocity corresponds to a particle that is not trapped long enough τ, α_v and $\dot{\omega}$ are stepped using the decaying equations. Then we can compute the instantaneous change in frequency $\delta\omega$ as well as the corrected frequency ω throughout the grid as needed to advance the current.

This code runs in a stable manner until amplifications on the order of ten are obtained. At this point oscillations in the waveform tend to appear at the equator which are difficult to eliminate but decrease by simply reducing the step size. This is connected to the fact, discussed in the following section, that the intrinsic value of the currents are large and a numerical cancellation to a high degree of accuracy is required to evaluate the vanishingly small current near the equator where the cancellation must be perfect. We anticipate that this problem will be cured when additional physical features such as the variation in resonance velocity are included. Such additional effects should stop the downstream growth of the interaction region, therewith limiting the total amplification to 20 - 30dB for which the scheme in its present conception appears adequate.

VII. Discussion of Results

This section presents the detailed results obtained by numerical integration of the wave equations. The full wave equation (5-2) for the phase has not been integrated at this time. Rather, a subsidiary asymptotic limit is utilized instead, as introduced in section VI and described below. The method for determining the frequency arose out of the understanding of the amplitude evolution at constant frequency, which must, therefore, be considered first. However, since the frequency changes affect the amplitude evolution only weakly[26], we present in the figures the waveforms that result when the whole evolution, including frequency changes, is done self-consistently.

The self consistent numerical determination of the waveform evolution that was idealized in section V (Figures 5.2a,b,c) is given in Figures 7.1a,b,c) . A comparison of the two sets is instructive. Apart from some ripples on the amplitude waveform, the idealized and actual pictures do not differ significantly until frame c. Here, what was initially a rather unexpected result appears. The amplitude has a triangular waveform where the upslope is linear to high accuracy implying that the nonlinear currents of the self-sustaining emission are very nearly constant in space, see Fig.7.1c), in spite of the large variability, with s, of the integrand in eq.(5-3) (see also Fig.7.5). This comes about because as the emission grows and more particles become trapped, the intrinsic size of I_R gets very large. It can only be offset by the trapping of stable, $\partial F/\partial v_\perp < 0$, particles to bring the full integral in eq.(5-3) to near zero (recall Fig.5.1). In fact, the asymptotic condition, $I_R \simeq 0$, implies a linear waveform for A, as will now be shown now.

Two strong physical mechanisms necessitate this simple result. The first mechanism is the local feed-back between the amplitude and the real part of the current linked by the trapping condition. The trapping condition,

$$Av_\perp \geq (1-\omega/\Omega)\,|(C'v_\perp^2 + D)s + T\dot{\omega}|, \qquad (7-1)$$

sets the range of perpendicular velocities that can be trapped at the value, A, of the local amplitude. From the condition of trapping for a full period, eq.(4-27), it can be seen that the relevant range of integration in the real current integral (eq.(5-3)) expands quickly towards high perpendicular velocities. If the amplitude is small, then this integration region is small. Since triggering requires this small perpendicular velocity region to fall into the unstable part of the distribution function the resulting current is negative downstream. Hence a small amplitude is amplified. On the other hand, if the amplitude is large, the range of trapped perpendicular velocities is very large. Since high perpendicular velocities

enjoy a stronger weighting in the current integral and their distribution function gradient is negative, the resulting current will be negative. Hence a high amplitude is damped. This stable feed-back between the amplitude and the current drives the amplitude to a local equilibrium value which balances the competing current contributions from low and high perpendicular velocities against each other. One can formulate this mechanism mathematically by a perturbation expansion of eq.(5-1) whose leading order is,

$$I_R = 0. \tag{7-2}$$

This will determine $A' = \partial A/\partial s$. The next order then gives from A' the residual current necessary to balance convection,

$$v_g A' = I_R. \tag{7-3}$$

The second mechanism involved in the linear amplitude shape results from the property of the trapping condition to favor an intermediate perpendicular velocity $v_\perp^m$ with a minimum absolute inhomogeneity parameter $|Q|$. In other words, the interaction regions which are centered about the equator $Q = 0$ shrink spatially for both higher and lower perpendicular velocities than $v_\perp^m$. This is visualized in Fig.7.2 which shows the location of the entrapping points,

$$s_+ = \frac{1}{Cv_\perp^2 + D}\left(\frac{v_\perp A}{1-\omega/\Omega} - T\dot{\omega}\right), \tag{7-4}$$

and the detrapping points,

$$s_- = \frac{1}{Cv_\perp^2 + D}\left(\frac{-v_\perp A}{1-\omega/\Omega} - T\dot{\omega}\right), \tag{7-5}$$

for different perpendicular velocities at constant A, ω/Ω and $\dot{\omega} = 0$. In this case the largest interaction region is associated with

$$v_\perp^m = \sqrt{D/C}. \tag{7-6}$$

Note that if $\dot{\omega} > 0$ ($\dot{\omega} < 0$) the drop shaped curve is pushed upstream (downstream) for small perpendicular velocities, but for simplicity ignore $\dot{\omega}$ in the following derivation.

As was pointed out earlier for triggering it is necessary that $v_\perp^m$ falls into the unstable part of the distribution function ($\partial F/\partial v_\perp > 0$). Consequently, far downstream there will be a region where the current is dominated by the amplifying neighborhood of $v_\perp^m$ since the amplitude is initially too low to trap enough stabilizing perpendicular velocities. Therefore, a negative current spike forms, which raises and steepens the front of the wave.

This shrinks the spread in entrapping points until all velocities are entrapped at practically the same point. Then the real current can be written in the following form,

$$I_R = -\tfrac{1}{2}\beta \frac{1-\frac{\omega}{\Omega}}{V_R\sqrt{A}} s(s-s_+)(s+s_+) \int\limits_{tr} dv_\perp \sqrt{v_\perp}\alpha_v(Q) S'^2 \frac{\partial F}{\partial v_\perp}, \qquad (7-7)$$

where the common entrapping point s_+ is just a number independent of the perpendicular velocity. To satisfy eq.(7-2) at every s-location it is, therefore, necessary to require in eq.(7-7) that

$$\int\limits_{tr} dv_\perp \sqrt{v_\perp}\alpha_v(Q) S'^2 \frac{\partial F}{\partial v_\perp} = 0. \qquad (7-8)$$

The factors in the integrand are positive except for the gradient of the distribution function which changes from a positive sign for low perpendicular velocities to a negative sign for high perpendicular velocities. Therefore, the only way eq.(7-8) can be satisfied is by adjusting the upper limit $v_\perp^+$ of integration such that the contributions from low perpendicular velocities (with $\frac{\partial F}{\partial v_\perp} > 0$) to the integral cancel the contributions from high perpendicular velocities (which have $\frac{\partial F}{\partial v_\perp} < 0$). The resulting upper perpendicular velocity boundary $v_\perp^+$ is the same for every grid point since all entrapping points have collapsed at the front end of the wave. Since $v_\perp^+$ is the largest perpendicular velocity that can be trapped at all points its inhomogeneity parameter must be unity, $Q(v_\perp^+) = 1$. This is only possible if the amplitude has (from eq.(7-1)) the shape

$$A(s) = \left(1 - \frac{\omega}{\Omega}\right) \frac{|S(v_\perp^+)|}{v_\perp^+}. \qquad (7-9)$$

Hence, the arclength dependence of the amplitude is determined by that of the inhomogeneity S. This wave form is a stable solution. The entrapping and detrapping points are found to be the same to lowest order for all relevant electrons as was assumed in Ref.34.

The amplitude is a linear function of s when the $\dot{\omega}$ contribution to the inhomogeneity S is negligible or linear. Then the inhomogeneity parameter is constant for each perpendicular velocity and takes the simple, arc length independent form

$$Q = \left(1 - \frac{\omega}{\Omega}\right) \frac{Cv_\perp^2 + D}{v_\perp A'}. \qquad (7-10)$$

With this expression the perpendicular velocity weighting of the gradient of the distribution function is fixed, which allows one to integrate the integral in (7-8) once and for all. For the distribution function of eq.(5.11) and other input parameters employed in Fig.7.1 one finds

the value $v_\perp^+ = 7.1$. Then equation (7-3) in combination with eq.(7-9) predicts a residual current of $I_R = -1.017$. This value is in excellent agreement with the value $I_R = -0.995$ obtained from the self-consistent numerical integration of Fig.7.1c after the fivefold display magnification is divided out.

In summary of the above:

The nonlinear dynamics embodied in I_R and not the wave equation (5-1) dominate in determining the emission waveform;

$$I_R \simeq 0 \;\Rightarrow\; A'.$$

Analogous considerations apply to the phase equation (5-2). However, since I_R and I_I/A have different integrands, the waveform, $A(s)$, that made $I_R \simeq 0$ will yield an I_I/A that is non-zero and large. To offset this the frequency must evolve to drive $I_I \simeq 0$. In fact, in a remarkable mimicking of the amplitude dynamics:

The nonlinear dynamics embodied in I_I and not the wave equation (5-2) dominate in determining the frequency waveform;

$$I_I \simeq 0 \;\Rightarrow\; \dot{\omega}.$$

Noting that $\dot{\omega}$ appearing in the inhomogeneity factor is the change seen by the resonant particles, setting $I_\phi = 0$ gives an equation for the frequency change, $\delta\omega$,

$$TB\left(\frac{\partial}{\partial t} + V_R\frac{\partial}{\partial s}\right)\delta\omega = -E\ , \qquad (7-11)$$

where the factors, T, B, and E are defined as,

$$T = 1 + \Omega/2\omega. \qquad (7-12)$$

$$B = \beta A^{-1/2}\int_{tr} dv_\perp v_\perp^{3/2}\alpha_v(Q)\sqrt{1-Q^2}\tau\frac{\partial F}{\partial v_\perp}, \qquad (7-13)$$

$$E = \beta A^{-1/2}\int_{tr} dv_\perp v_\perp^{3/2}\alpha_v(Q)\sqrt{1-Q^2}(S's\tau - \tfrac{1}{2}V_R S'\tau^2)\frac{\partial F}{\partial v_\perp}, \qquad (7-14)$$

The factors B and E are large in the interaction region where the trapping condition is satisfied. Since eq.(7-11) is a wave equation propagating opposite to the group velocity of the whistler waves, one cannot expect numerical schemes based on eq.(5-2) to be very

effective. This may account for much of the numerical stability problems encountered in related schemes previously[33].

If the ratio E/B is evaluated for the dominant velocity, $v_\perp^m = \sqrt{D/C}$, one finds,

$$\dot{\omega} = -\frac{D}{T}(2s - V_R\tau) \ . \qquad (7-15)$$

Since $T > 0$ generally and $D > 0$ for most magnetospheric conditions, eq.(7-15) is just a modified Helliwell condition, here derived from the nonlinear currents. Since, in the marginal case emphasized in this paper, the emission sets up downstream after initiation upstream, one can expect a faller preceded by an initial small offset rise[26].

The frequency-time curve for the emission of Fig.(7.1) is displayed in figure (7.7) along with a similar observed emission triggered by a Siple transmission[39]. At this level of comparison, the agreement between theory and observation is excellent, although some qualifications need to be made. The principle shortcomings are: 1) that the emission does not terminate, but continues to grow in amplitude downstream while dropping further in frequency, and 2) that the amplitude and frequency-time waveforms cannot be synchronized without solving the two way wave equation (6-7) to propagate the frequency signal out of the interaction region. Demonstration of termination may be related to allowance for variation of the distribution function with frequency and arclength due the change in resonant velocity. This in turn effects the synchronization question since as long as the interaction region grows downstream, with the wavefront propagating at the group velocity, propagation of the frequency waveform out of the interaction region is unnecessary.

In addition it should be noted that the asymptotic coefficient is, $C_o = .48$. This is probably too large to trust the asymptotic theory, quantitatively, in the initial phases of triggering. Of course, by the time the amplitude grows to $A \sim 3$, there would be some 6 trapping oscillations and thus one could have confidence in the asymptotic theory through most of the emission process. We feel that the qualitative picture is very likely to be correct anyway. In fact for very similar parameters, as will be shown below, one can get emissions at $C_o \sim .15$ or less where the asymptotic theory would be valid throughout. However, no significant differences in the final emission forms are found in such cases. The larger C_o case of Fig.7.1 is presented first because of the simplicity of the waveforms.

Note also the value chosen for the ratio of density to magnetic field scale length, $L_n/L \sim .735$, which is quite a bit smaller than the values one would use based on the diffusive equilibrium model[61] ($L_n/L \sim \infty$) or the collisionless model[29,40,44,62] ($L_n/L \sim 1$) of the magnetospheric density. This choice was made to adjust the frequency fall rate, via

the coefficient D in equation (7-15), to conform with observations. At larger values of L_n, i.e. $L_n \to \infty$, the $\dot{\omega}$ value would be some 20% higher.

The real current, I_R, and trapping time, τ, as functions of perpendicular velocity and arc length are shown for this case in Figures (7.3-7.6). Observe that the intrinsic magnitude of the current, in both positive and negative regions, is much larger than the final value shown in Fig.(7.1) and that it varies significantly as a function of arc length. This bears on the discussion above explaining the origin of the triangular waveform of the amplitude. Both the current and trapping time originate at very nearly that same spatial location on the upstream side for all significant perpendicular velocities once the emission is underway. This property was also necessary to account for the triangular waveform.

An input signal with a 100 *msec* long pulse, but identical in all other respects does not yield an emission, as shown in Fig.(7.8). The frequency-time curve, showing some small changes associated with the waveform distortion is given in Fig.(7.9)

The sensitivity of the triggering process to the initial frequency[39] is displayed by comparing the sequences of Figures (7.10) and (7.12). The frequency-time curve corresponding to Figure (7.10) is shown in Fig.(7.11). In the first sequence (Fig.(7.10)) with an initial frequency of 5.5 kHz, triggers an emission while a 10% lower frequency, 5.0 kHz does not. Although some small currents form (as indicated by the dotted line in the figure), their is no discernible change in the input signal and no emission. The parameters used to obtain these data are only slightly different from those used above, however, the difference is significant in the following way. The adjustments in the parameters were made to raise A_{min} (eq.(4-29)) to a value near unity so that triggering becomes more sensitive to the trapping threshold than to the number of high energy electrons. Then, because of the sensitive inverse dependence of A_{min} on frequency, emissions can be eliminated by a slight reduction of the triggering frequency if one is very near the threshold initially. The previous case is in a regime that is farther way from the trapping threshold where triggering is primarily determined by the electron density. Since the factor β in front of the current is an inverse function of frequency, lowering the frequency there has the opposite effect.

A case having a larger amplitude triggering signal is shown in figures (7.13) and (7.14). In this run the asymptotic parameter, C_o, is .15 so that one would expect the asymptotic theory to be valid throughout the process. The basic features of the emission remain the same as in figure (7.1) and the frequency-time curve, Fig. (7.14), is very similar to (7.2). An otherwise identical pulse, but with a 100 *msec* length, failed to trigger. The new feature is the appearance of a kind of *double layer* in the current near the origin. This provides

some deterrence to emissions, but is not critical in this case. It arises when the initial pulse traps a wide range of perpendicular velocities that includes some of the particles on the downsloping portion of the distribution function. These high velocity particles contribute strongly to the current near the equator with the opposite signature to the currents created by the destabilizing particles discussed in section V. This accounts for the double layer, and its tendency to interfere with the emission process since it has the stable signature. The localization near the equator can be seen from the trapping condition, eq.(5-9) and Fig.7.2, for a constant amplitude pulse.

For parameters such that the initial interaction length exceeds the pulse length another phenomenon appears. This is shown in Figures (7.15) and (7.16). In this case substantially more high energy electrons are required to initiate an emission. However, the characteristic constant current waveform does not have time to form until after the trailing edge of the triggering signal passes the equator. This prevents the development of the triangular amplitude form originating from the equator. Instead the signal drifts downstream for some distance until the marginal currents necessary to produce the slope required by, $I_R = 0$, are formed. Interestingly this *disconnected* signal has exactly the same slope as the triangular form and it has the same underlying cause. If the slope were continued to the upstream side past the trailing edge of the waveform it would intersect the equator. It is as though the emission "remembers" this location. This gives some indication of the strength of the marginal condition, $I_R = 0$. The currents necessary to bring the amplitude up to the value required by this condition are provided by the spike at the trailing edge.

Finally we have a case that is driven so hard that the emission process begins before the leading edge of the triggering pulse has crossed the equator, shown in Fig.(7.17). Notice that after some evolution a triangular waveform oriented in the reverse direction begins to form on the upstream side. A short inspection will show that the same arguments, stemming from the necessity of cancelling the large currents, apply to the upstream side and give the reversed triangle there (eq.(7-9)). Eventually the downstream triangle also forms, with a spike due to the double layer near the equator. Note that the upstream triangle is also a selfsustaining form. Eventually, the rising frequency generated on the upstream side is canceled by the falling contribution due to the downstream triangle. The frequency-time curve Fig.7.18, in fact, resembles an inverted hook. If the downstream portion were diminished, a sustained riser would be the result. This gives some indication of how a riser, and various hooks might form. To demonstrate these forms compellingly, however, the physics responsible for the termination and the full phase evolution using the two way wave equation must be added.

VIII. Conclusions and Summary

To summarize the triggering picture, a rather strong threshold behavior has been exhibited in that the nonlinear currents must be driven up sufficiently by the trigger signal to offset convection. Otherwise a self-sustaining emission cannot form. The conditions needed for triggering are:

1) An inverted population, $\partial F/\partial v_\perp > 0$, in the trapped range of perpendicular velocities. Linear instability of the tail distribution $F(v_\parallel, v_\perp)$ is not necessary[34].

2) Sufficient amplitude for trapping in the triggering signal.

3) Sufficient density in the resonant portion of the distribution function such that the driven current can offset convection.

If these conditions are satisfied a long enough input wave will always trigger a self-sustaining emission. Furthermore, the resulting emission is independent of trigger length or amplitude, or the number density of high energy electrons. This comes about because of the marginal condition, $I_R = 0$, which determines the amplitude slope, A', in terms of only the magnetospheric parameters which characterize the inhomogeneity and distribution function. The same is true of the frequency change rate as expressed in equation (7-15). These are very persistent features of the emissions that are found over a wide range of parameters.

We conclude by returning to Matsumoto's list[11] of observed features to show how and to what extent they can be explained by the theory. The threshold behavior (points 1a) and 5)) was displayed explicitly. The narrow bandwidth requirement, 1b), follows from the necessity of trapping. In fact, in the example of figure (7.1), the initial trapping frequency was 21 Hz, implying initial frequency bandwidths somewhat less, or near the 10 Hz quoted by Helliwell[13]. Triggering by both high and low power transmitters, 1c), can be understood from the independence on trigger signal of the emission waveform and frequency behavior. Thus high power has no effect once threshold is passed. Matsumotos's point 1d) is somewhat obscure. We take it to mean that emissions can occur repeatedly with no evidence of any recovery time for the phenomenon. This can be accounted for by a small region of distribution function and resulting small energy extraction used in the triggering process. Thus emissions may occur repeatedly.

The growth characteristics described in point 2) are very much in line with the numerical calculations given above. The initial growth exhibited by the exponential rise to the triangular peak at the leading edge is in the range of $100 - 200$ dB/sec in our runs.

Total growth shown is in the 20 to 30 dB range, although, as mentioned above we have yet to get the emissions to terminate and so the final value to be obtained must await further study. During this initial growth phase the frequency is rising slightly, less than 200 Hz, accounting for point 2b). The frequency waveforms superposed on the amplitude show that the frequency drop or "release" begins at the peak of the triangle when growth, as viewed from downstream, stops. This is point 2c).

The frequency variation described in point 3) is evident above for the marginal emissions near the threshold. The fallers observed in the code correspond in some detail, including the initial rise in frequency, to the observation. Risers have not yet been well documented in the theory, for the reasons discussed above. Some indication of how they would arise for longer pulses and more intense magnetospheric conditions was given, however.

Point 4) can be understood if the population inversion required for the emission process is produced by the precipitation of electrons following substorms, but several days are required to reestablish the ducts. Point 6) is related somewhat in that the high energy electron population is expected to vary greatly in quantity and distribution. That this variation is not observed to effect the emission characteristics theoretically was discussed at length above.

The main unanswered questions concern the mechanism behind the termination of the emissions, and the detailed synchronization of the amplitude and frequency waveforms requiring the solution of the two-way wave equation. These points could be resolved within the present theoretical framework. Activity on these issues is currently underway.

Figure Captions

Fig.(3.1): Family of electron orbits in $u - \psi$ phase space. The horizontal axis is a 2π interval in ψ while an interval in u about the resonance line $u = 0$ is drawn vertically. Fast time scale electron motion for a constant inhomogeneity parameter $Q = 1$ and different values of the integration constant h (for more details see text).

Fig.(3.2): Same as Fig.(3.1) but $Q = 0.5$. The broken line represents the separatrix which divides trapped and untrapped orbits. For the definition of $\psi_a, \psi_b, \psi_c, \psi_x$, and P_o see text.

Fig.(3.3): Same as Fig.(3.1) but $Q = 0$.

Fig.(3.4): a) Single electron orbit in $u - \psi$ phase space. The input parameters were taken from the faller in Fig.(7.1-7.3), with $v_\perp = \sqrt{3D/C} = 1.662$. On the horizontal axis ψ is drawn, on the vertical axis u. Contrary to Figure 3.1-3 the exact equations of motion were integrated for a long period of time. The electron enters the window from the top left, becomes entrapped and executes $6\frac{1}{2}$ trapping oscillations while it streams along the field line along the field line across the equator. After detrapping the electron leaves to the top right. A constant amplitude ($A = 3$) and frequency ($\dot{\omega} = 0$) was used.

Fig.(3.5): u (solid line) and ψ (broken line) of the previous graph were plotted individually versus time. The constancy of the amplitude of u oscillations during the trapped state was predicted by eq.(3-64). The continuous rise of the $\psi(t)$ curve reflects the slow drift of the center of oscillation P_o in Fig.(3.4) caused by the change of the inhomogeneity parameter Q during the drift of the electron across the field line equator.

Fig.(3.6): Similar as in Fig.(3.4) except the triggering amplitude $A = 1$ was used. Only $2\frac{1}{2}$ trapping oscillations are possible indicating the closeness to the triggering threshold.

Fig.(5.1): High energy electron distribution function F versus perpendicular velocity. This form of distribution was underlying all numerical integrations displayed in this paper. The shape of F is given in eq.(5-11). In this Figure $\Delta = 1$ was used. The dashed line represents the velocity, $v_\perp^o = \sqrt{3D/C}$, of maximal number of trapping oscillations in the triggering wave of Fig.(7.1). The dotted lines show the lower $v_\perp^-$ and upper $v_\perp^+$ velocity boundary opened by the quartic condition (5-10) for $A = 1$ and the data of Fig.(7.1).

Fig.(5.2): Expected pulse and current evolution. a) Characteristic current signature for undistorted triggering wave. b) Subsequent evolution in the presence of input wave. c) Self

sustaining waveform and current after passage of input wave.

Fig.(7.1): Self-consistent numerical determination of Whistler wave amplitude and real current displayed versus grid points. The position 0 on the x-axis represents the field line equator. The current (dotted line) has been magnified five times for display. a) Low amplitude triggering wave generates small characteristic current signature. b) The triggering wave has propagated into the interaction region spanning the equator. Upstream portion of wave pulse begins to dampen away while downstream portion is amplified. c) The dynamical equilibrium of downstream emission is reached. The downstream current spike indicates the intrinsic size of the current while the constant portion shows the small residual value necessary to balance convection of the wave. The amplitude is essentially a linear function of arc length along the field line.

Fig.(7.2): Trapped perpendicular velocities in a constant amplitude, constant frequency wave versus arclength. The s_+ and s_- curves enclose the interaction region which is longest for $v_\perp = \sqrt{D/C}$.

Fig.(7.3): Real current J_R versus perpendicular velocity and grid points for Fig.(7.1b)

Fig.(7.4): Trapping time τ versus perpendicular velocity and grid points for Fig.(7.1b)

Fig.(7.5): Real current J_R versus perpendicular velocity and grid points for Fig.(7.1c).

Fig.(7.6): Trapping time τ versus perpendicular velocity and grid points for Fig.(7.1c).

Fig.(7.7): Frequency-time curve for the emission depicted in Fig.(7.1).

Fig.(7.8): Amplitude and current evolution for a 100 $msec$ pulse, identical in all other respects to that of Fig.(7.1). Although there is some distortion of the initial pulse, a self-sustaining emission does not form.

Fig.(7.9): Frequency-time curve for the case depicted in Fig.(7.8).

Fig.(7.10): Evolution sequence illustrating the sensitivity to initial frequency, 5.04 kHz in this case. A self-sustaining emission is seen to form.

Fig.(7.11): Frequency-time curve for the case depicted in Fig.(7.10).

Fig.(7.12): Evolution sequence illustrating the sensitivity to initial frequency, 4.5 kHz in this case. No emission forms and the current attains negligible magnitude. The change in the frequency is not discernable.

Fig.(7.13): Emission sequence showing characteristic waveform for larger amplitude input signal.

In this case the asymptotic parameter is, $C_o = .15$. Note the formation of a current double layer near the equator superimposed on the standard signature of Fig.(7.1).

Fig.(7.14): Frequency-time curve for the case depicted in Fig.(7.13).

Fig.(7.15): Emission sequence of a *disconnected* emission, corresponding to shorter input signal length.

Fig.(7.16): Frequency-time curve for the case depicted in Fig.(7.15).

Fig.(7.17): Very strongly driven emission sequence, showing the development of self-sustained upstream currents. A rise in frequency is associated with the dominance of the upstream emission as shown in Fig.(7.18).

Fig.(7.18): Frequency-time curve for the case depicted in Fig.(7.17).

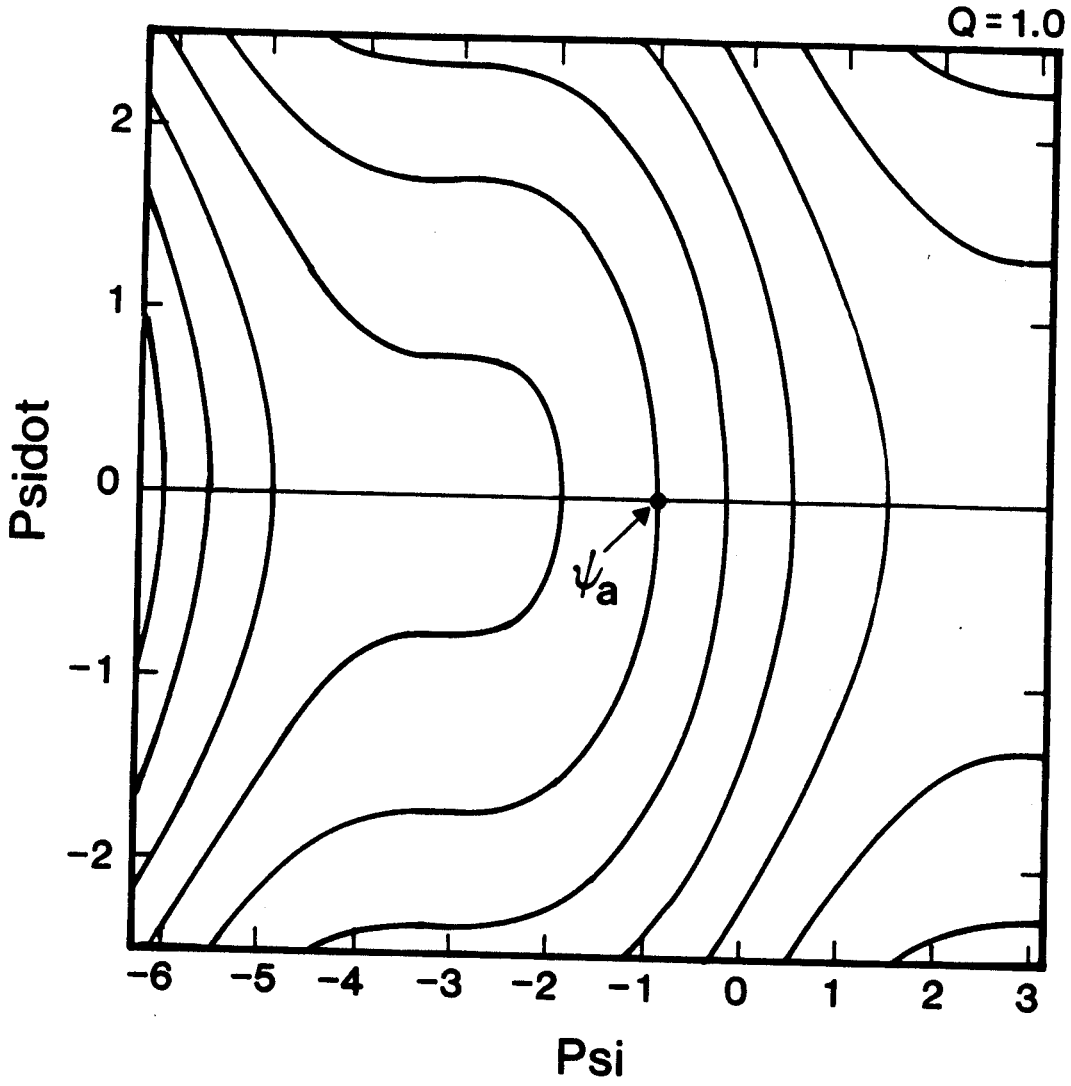

Fig.(3.1)

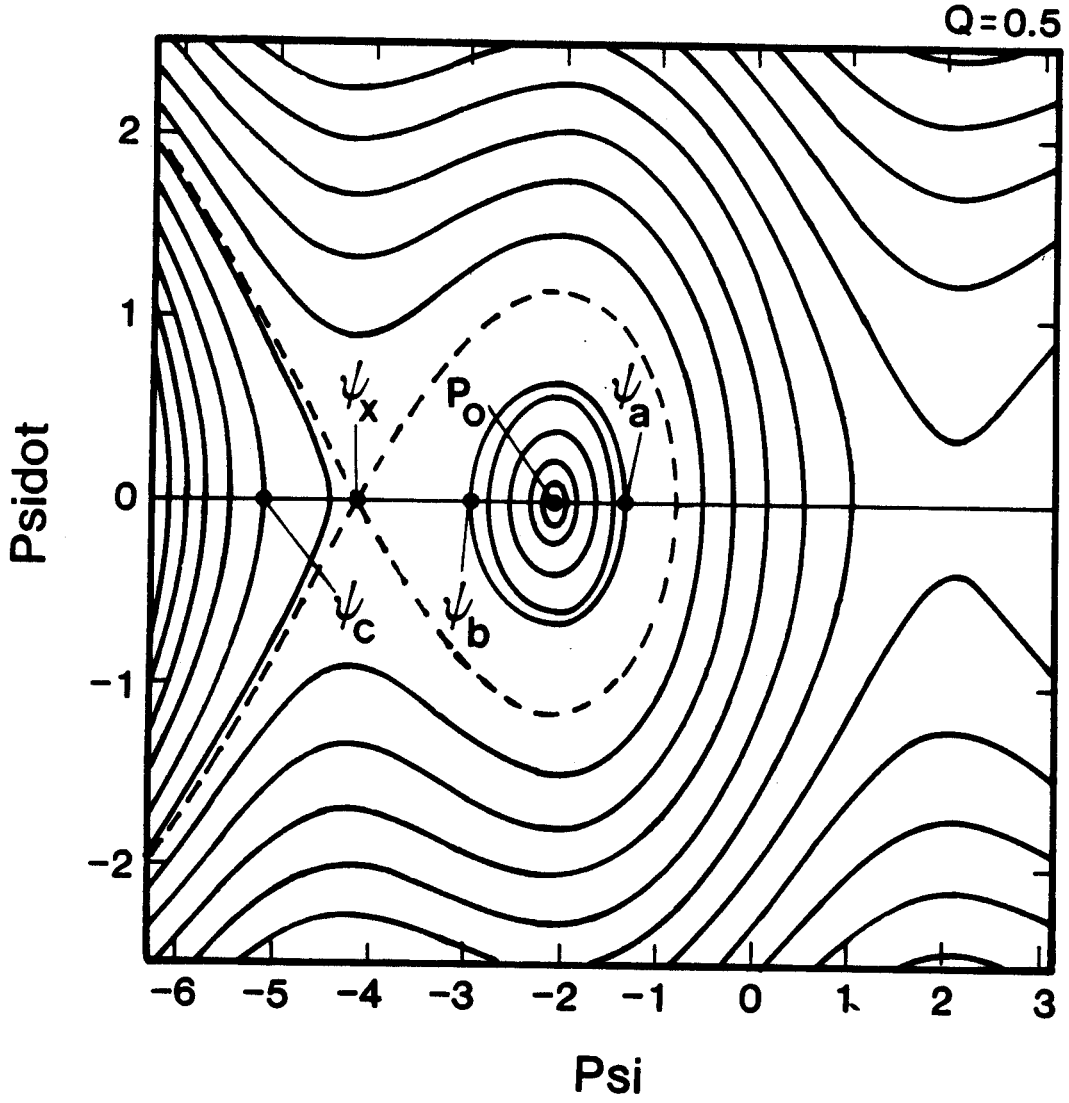

Fig.(3.2)

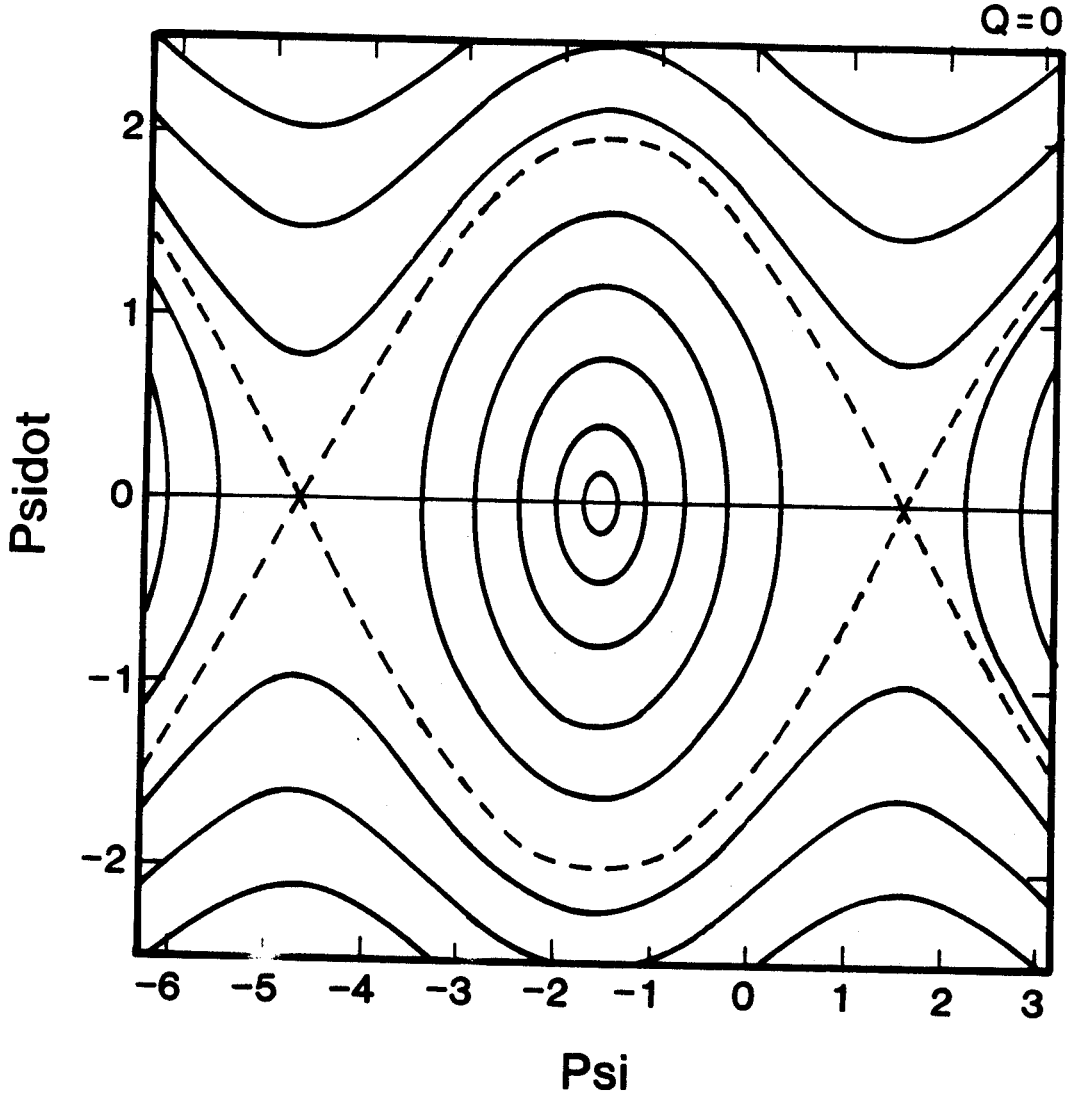

Fig.(3.3)

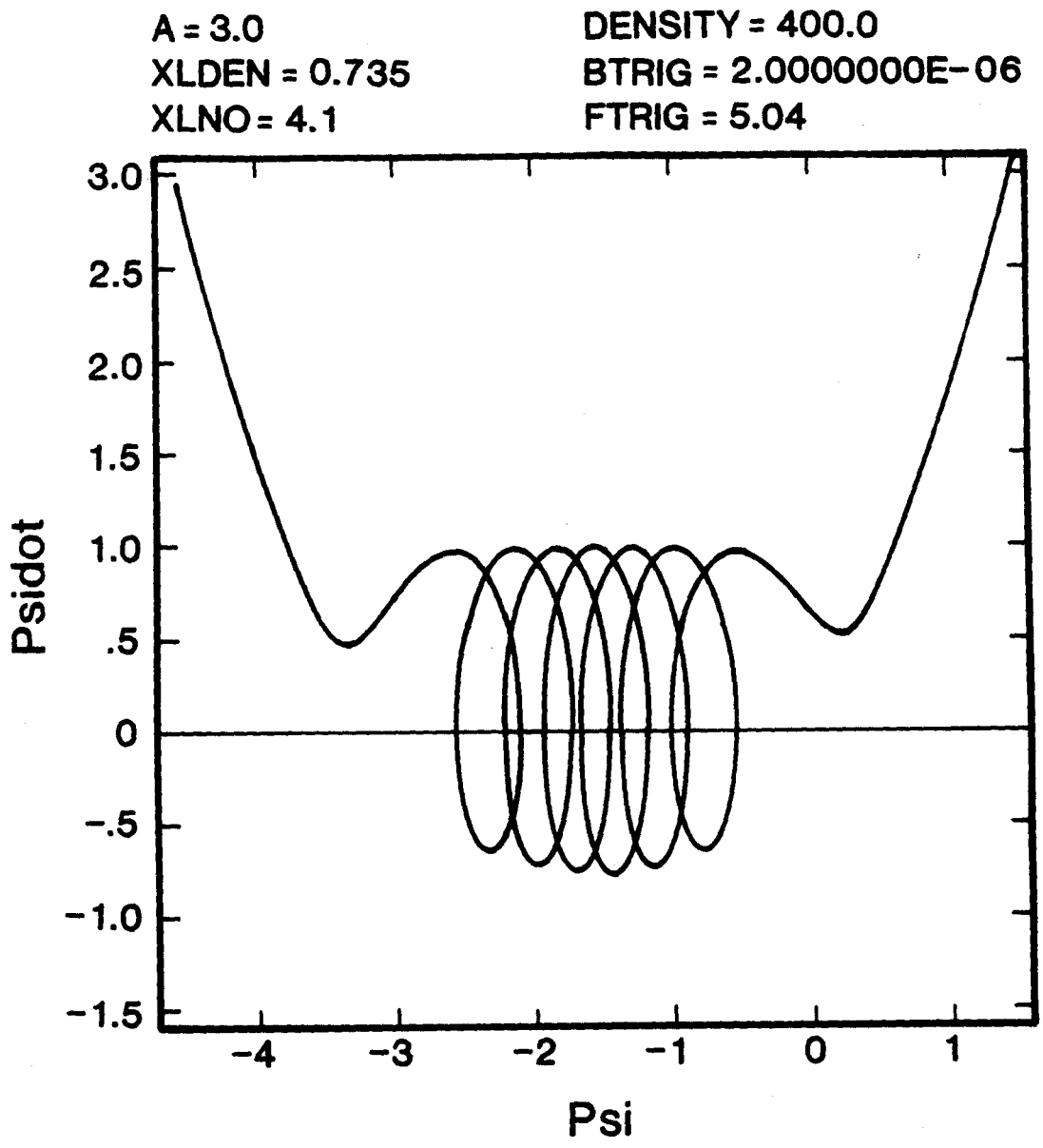
A = 3.0
XLDEN = 0.735
XLNO = 4.1
DENSITY = 400.0
BTRIG = 2.0000000E-06
FTRIG = 5.04
3.0
2.5
2.0
1.5
1.0
.5
0
-.5
-1.0
-1.5
Psidot
-4
-3
-2
-1
0
1
Psi

Fig.(3.4)

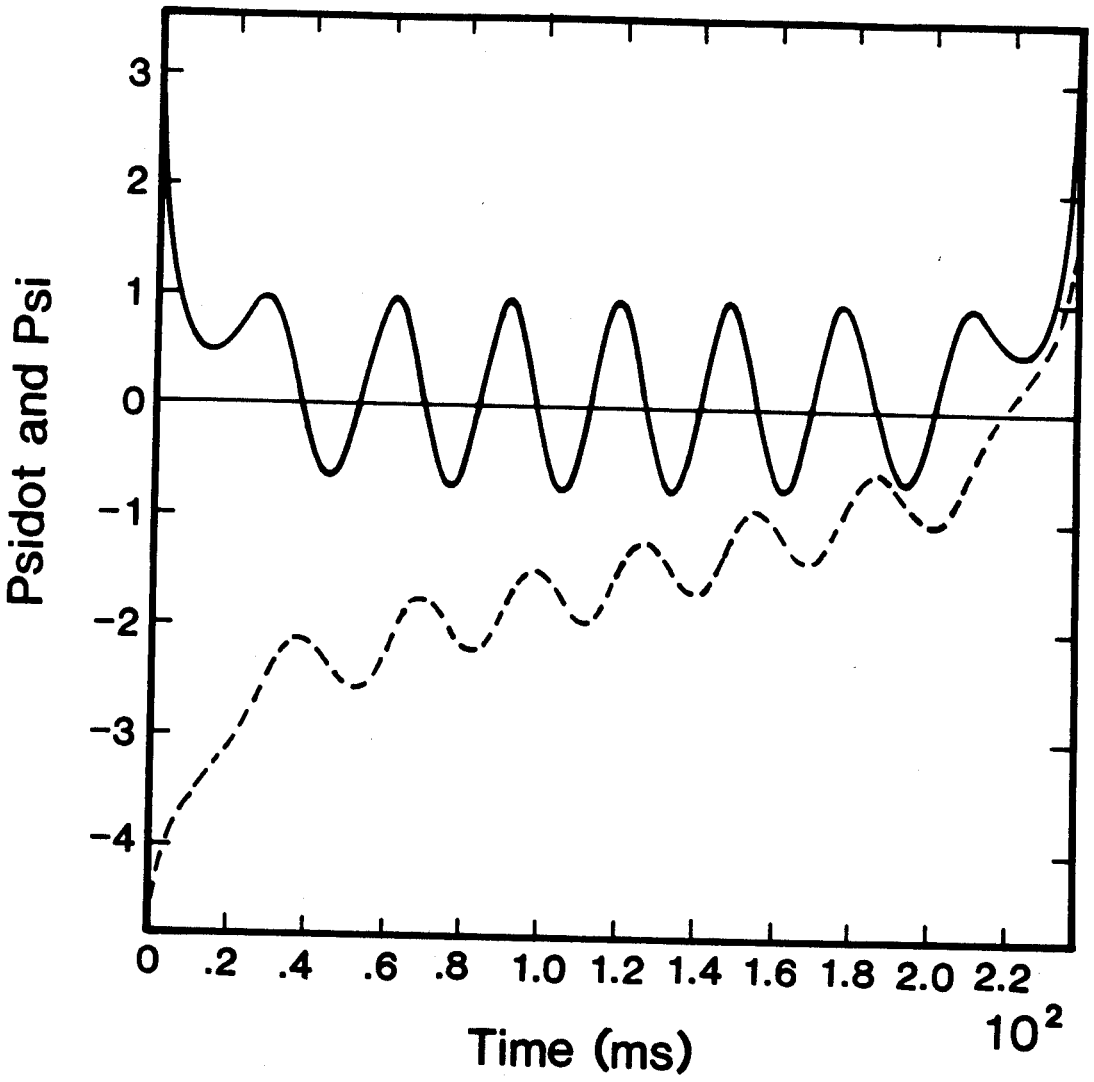

Fig.(3.5)

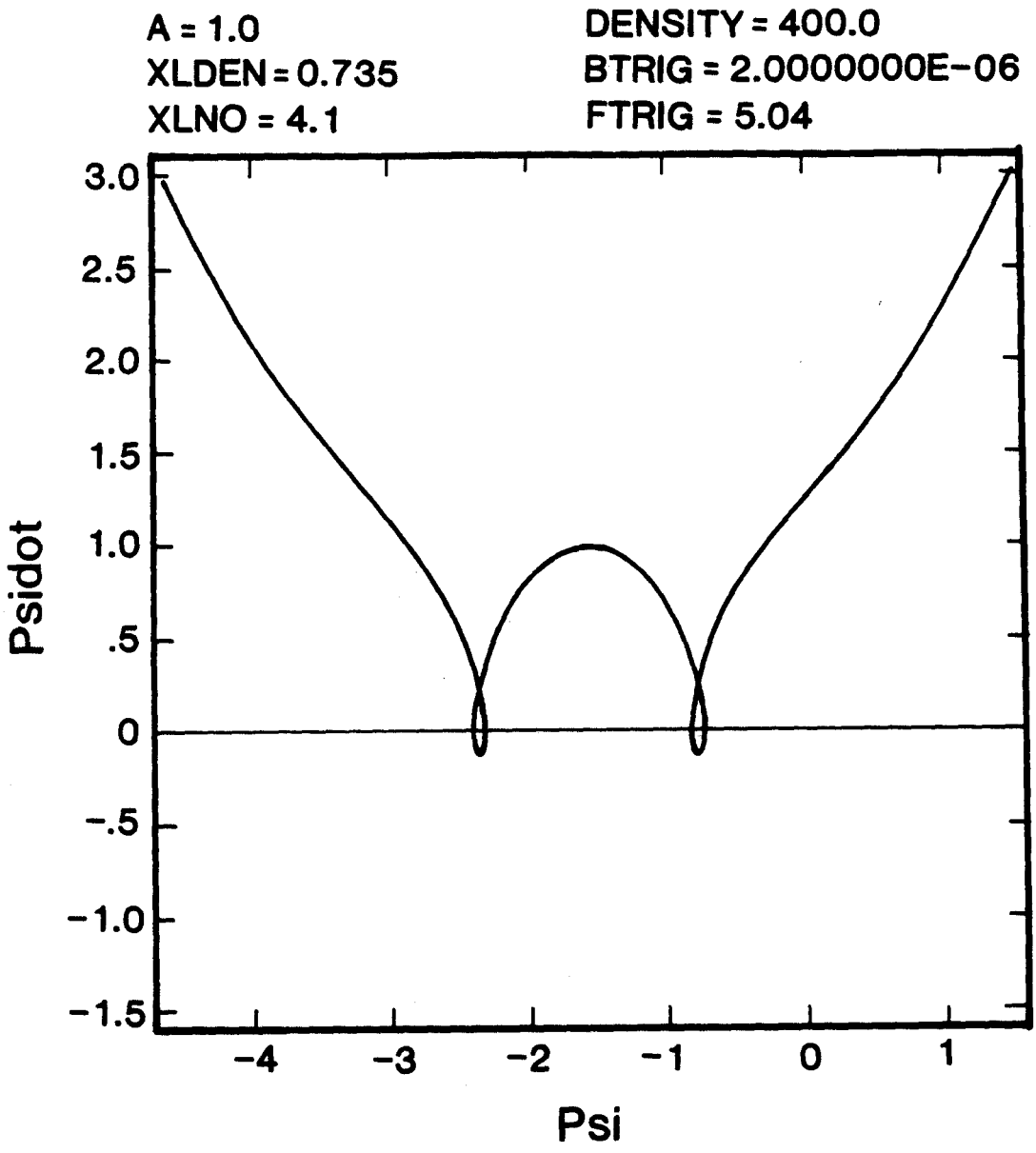
A = 1.0
XLDEN = 0.735
XLNO = 4.1
DENSITY = 400.0
BTRIG = 2.0000000E-06
FTRIG = 5.04
Psidot
3.0
2.5
2.0
1.5
1.0
.5
0
-.5
-1.0
-1.5
-4
-3
-2
-1
0
1
Psi

Fig.(3.6)

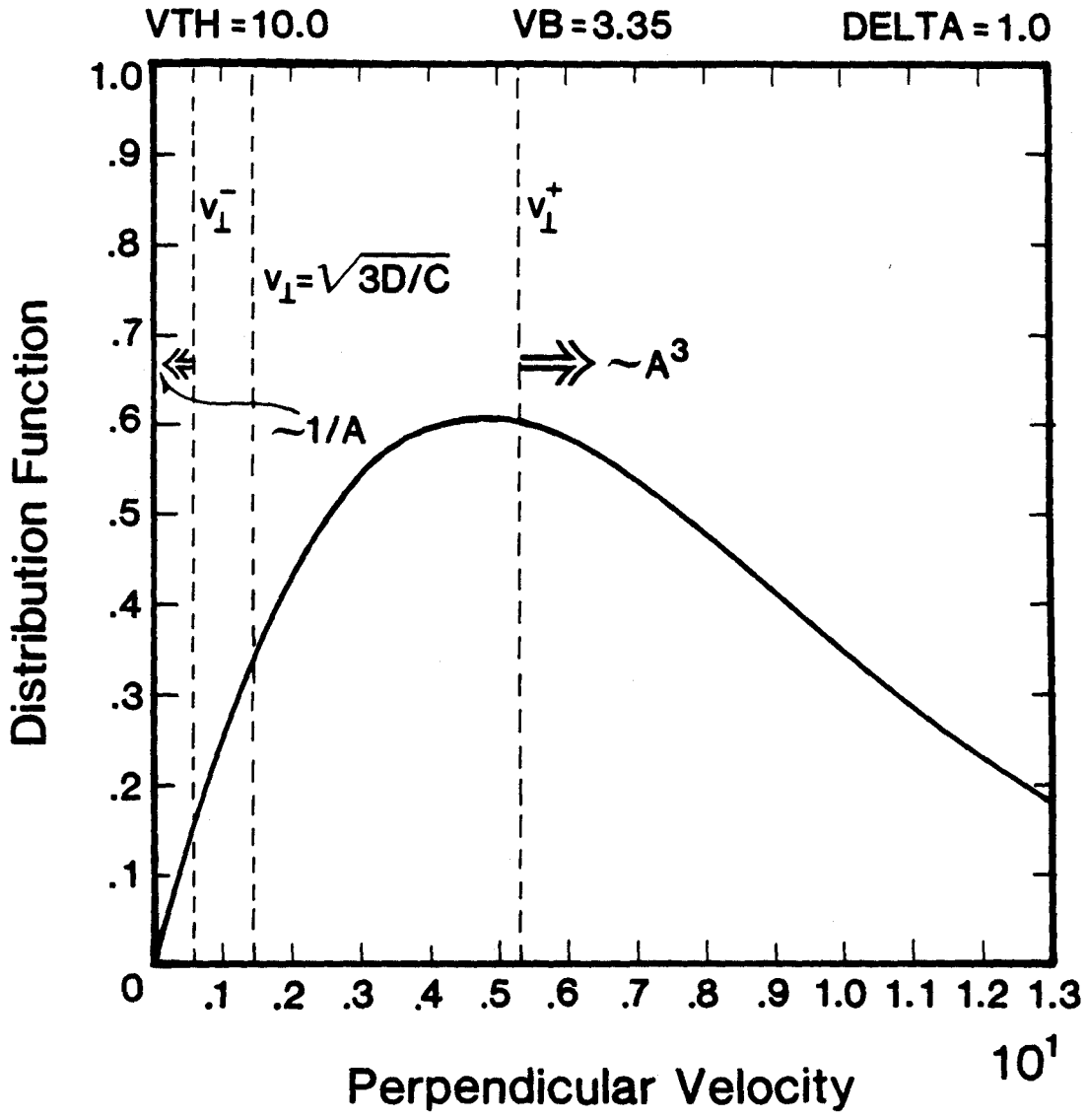
VTH = 10.0
VB = 3.35
DELTA = 1.0
Distribution Function
1.0
.9
.8
.7
.6
.5
.4
.3
.2
.1
0
$v_\perp^-$
$v_\perp^+$
$v_\perp = \sqrt{3D/C}$
$\sim A^3$
$\sim 1/A$
.1 .2 .3 .4 .5 .6 .7 .8 .9 1.0 1.1 1.2 1.3
10^1
Perpendicular Velocity

Fig.(5.1)

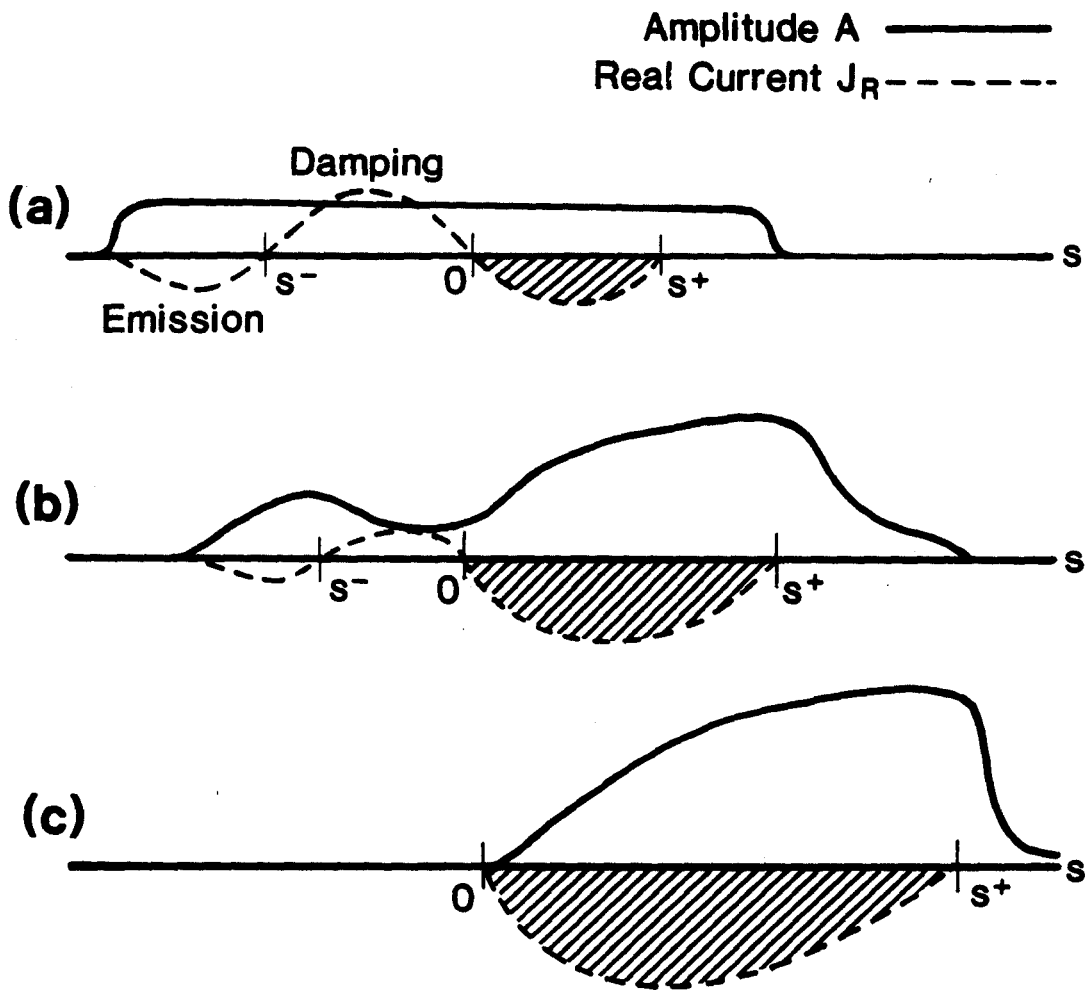
Amplitude A
Real Current J_R
(a)
Damping
Emission
s^-
0
s^+
s
(b)
s^-
0
s^+
s
(c)
0
s^+
s

Fig.(5.2)

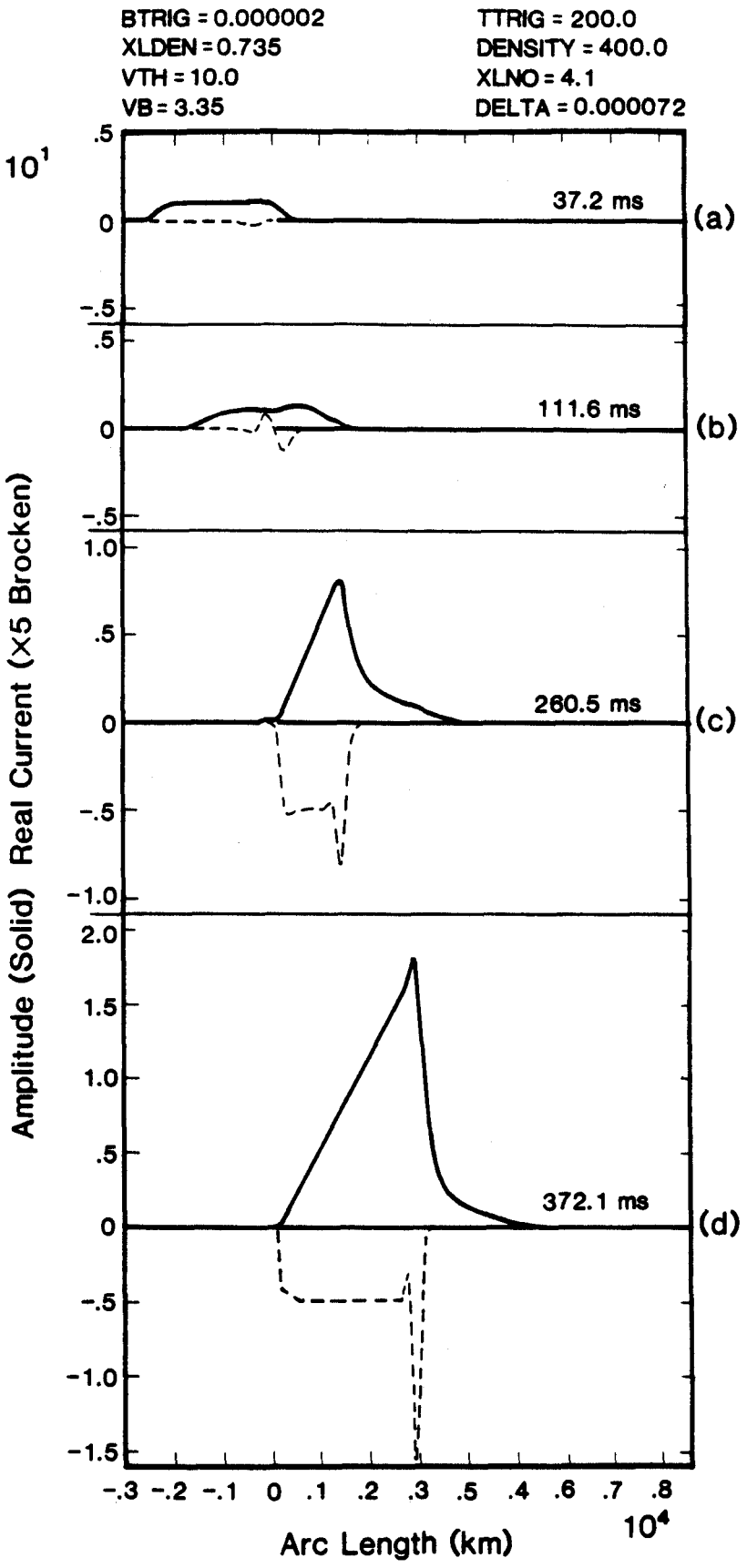

8643.26.23

Fig.(7.1)

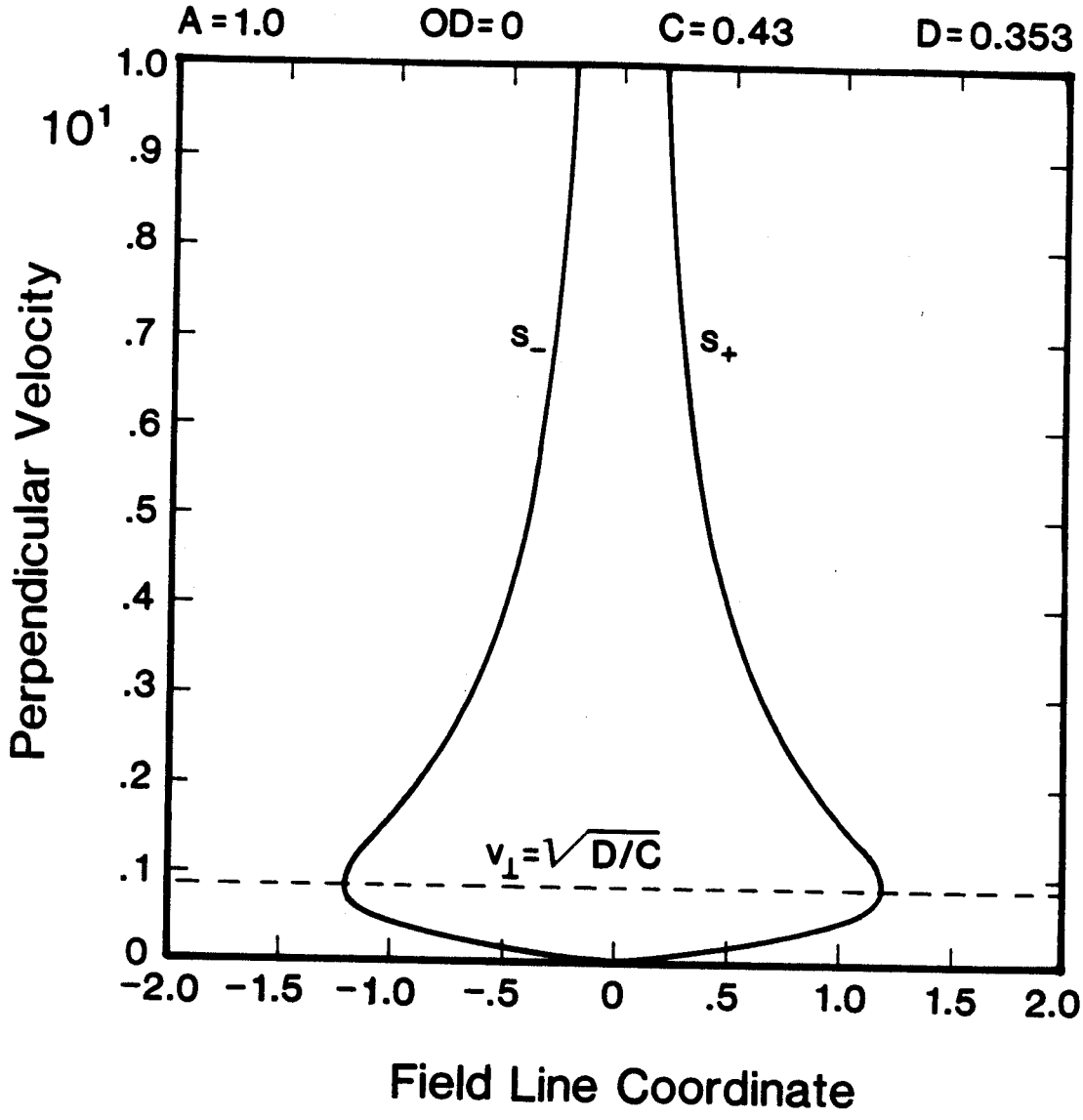
A = 1.0
OD = 0
C = 0.43
D = 0.353
1.0
10^1
.9
.8
.7
.6
.5
.4
.3
.2
.1
0
Perpendicular Velocity
s_-
s_+
$v_\perp = \sqrt{D/C}$
−2.0
−1.5
−1.0
−.5
0
.5
1.0
1.5
2.0
Field Line Coordinate

Fig.(7.2)

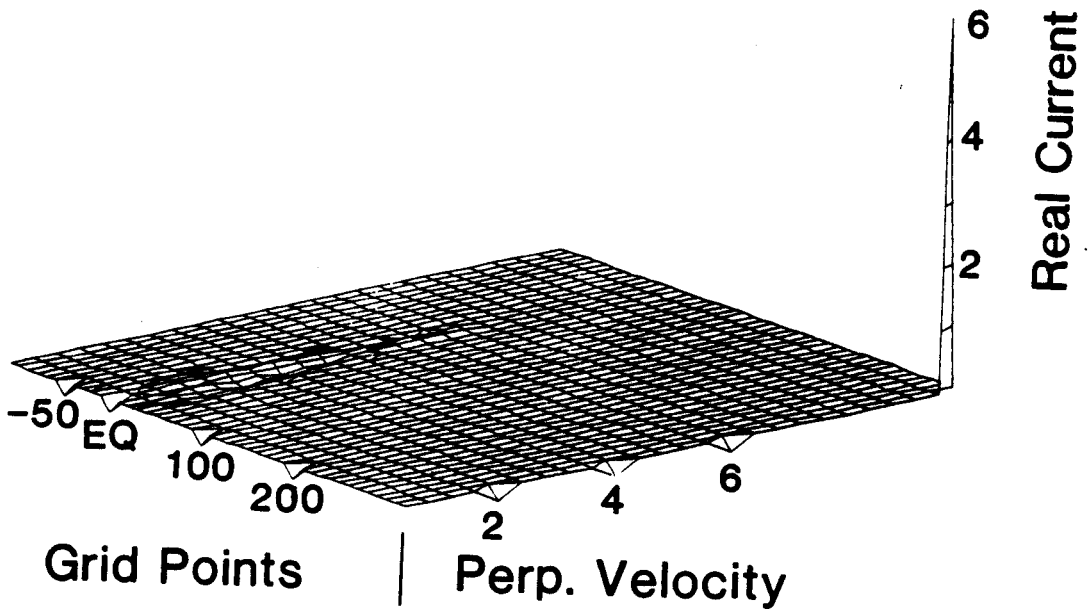

Fig.(7.3)

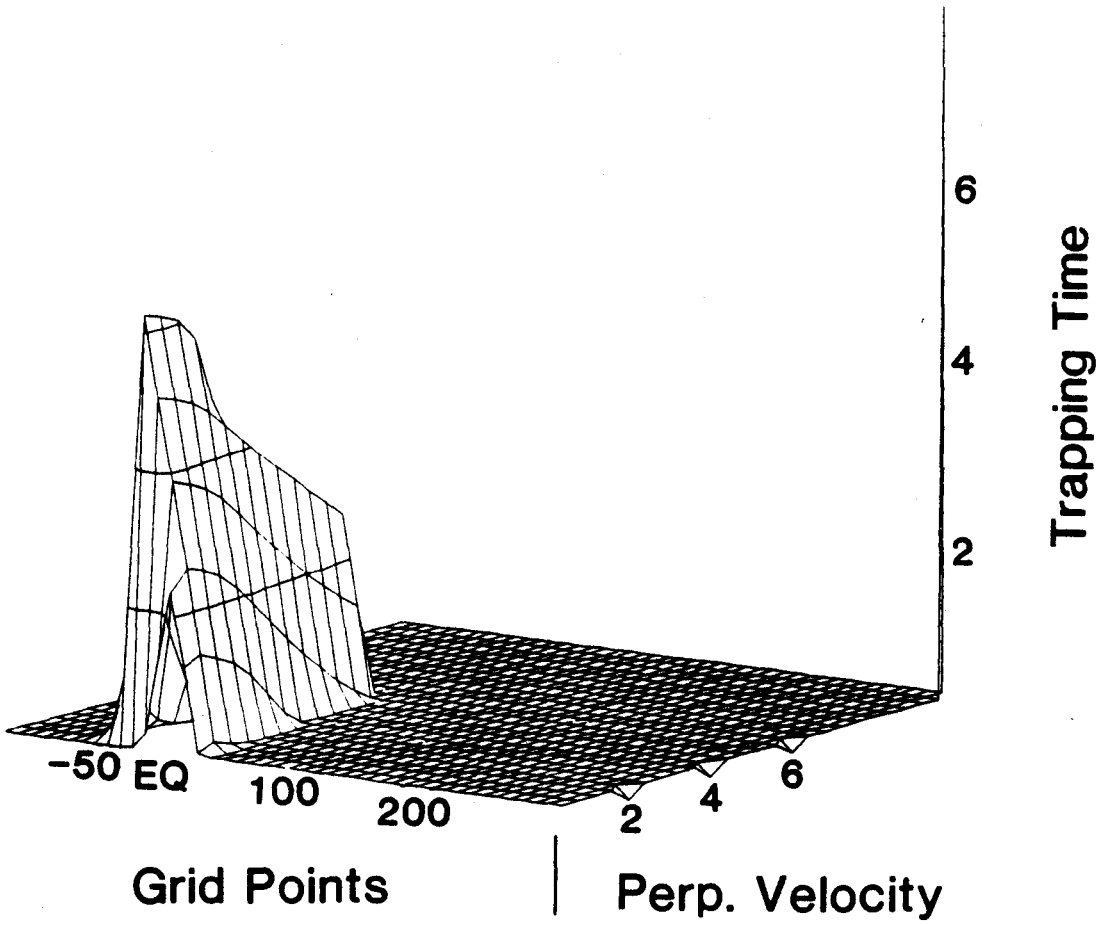

86 3.26.15

Fig.(7.4)

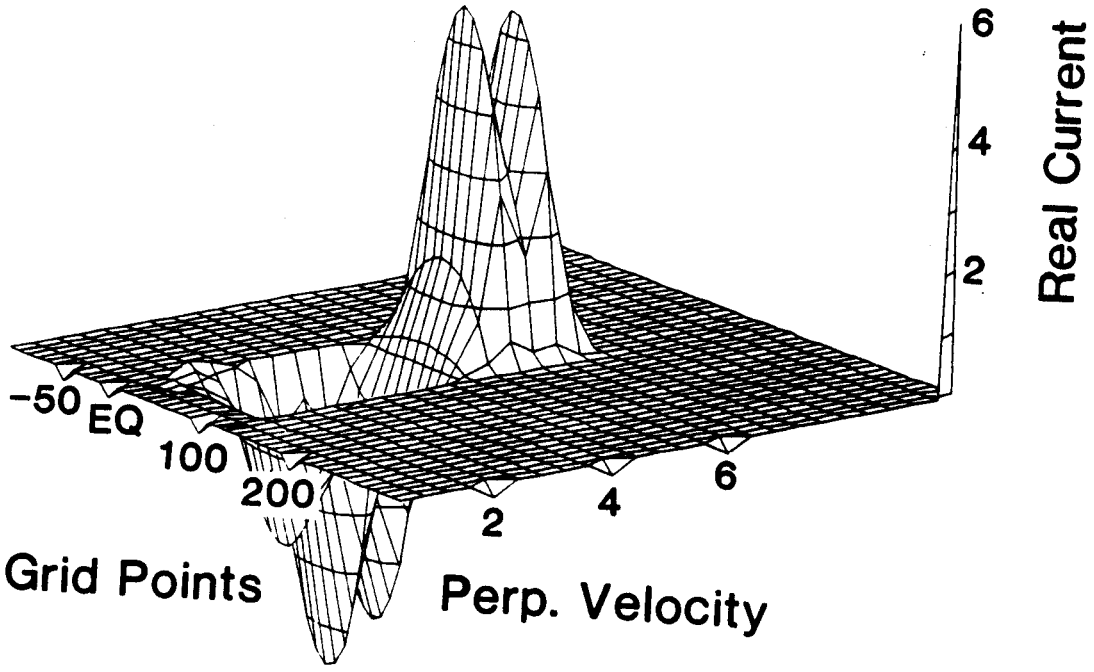

Fig.(7.5)

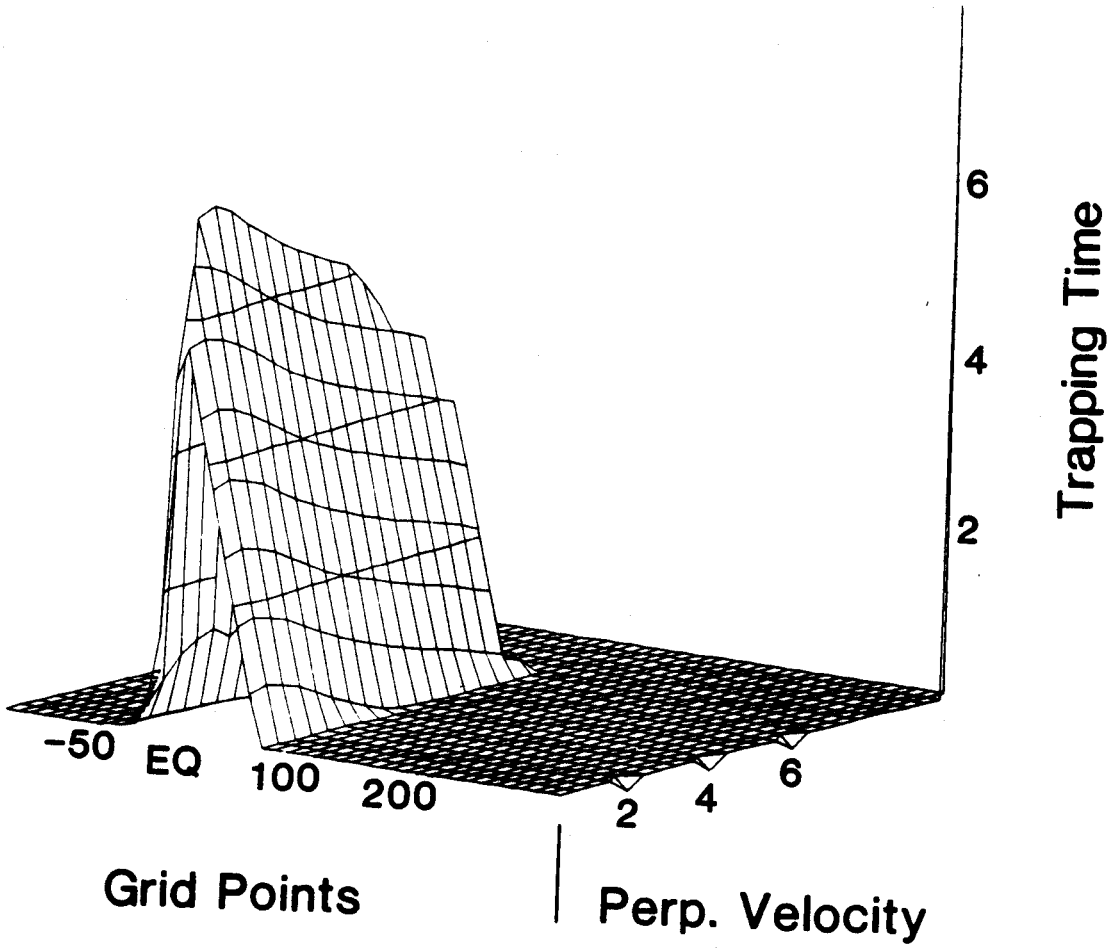
6
4
2
Trapping Time
-50
EQ
100
200
2
4
6
Grid Points
Perp. Velocity

Fig.(7.6)

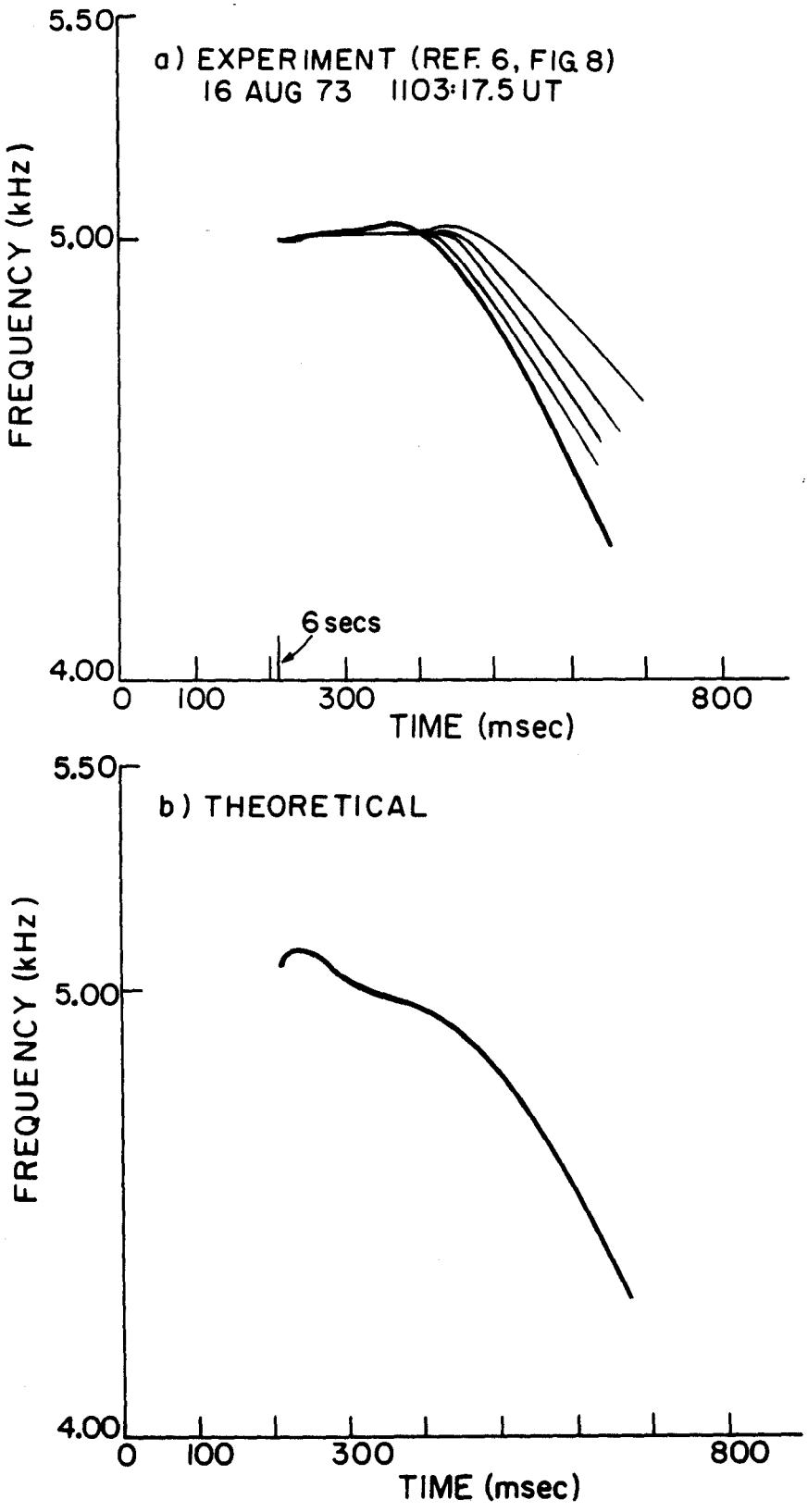
a) EXPERIMENT (REF. 6, FIG. 8)
16 AUG 73 1103:17.5 UT
5.50
5.00
4.00
FREQUENCY (kHz)
6 secs
0
100
300
800
TIME (msec)
b) THEORETICAL
5.50
5.00
4.00
FREQUENCY (kHz)
0
100
300
800
TIME (msec)

Fig. (7.7)

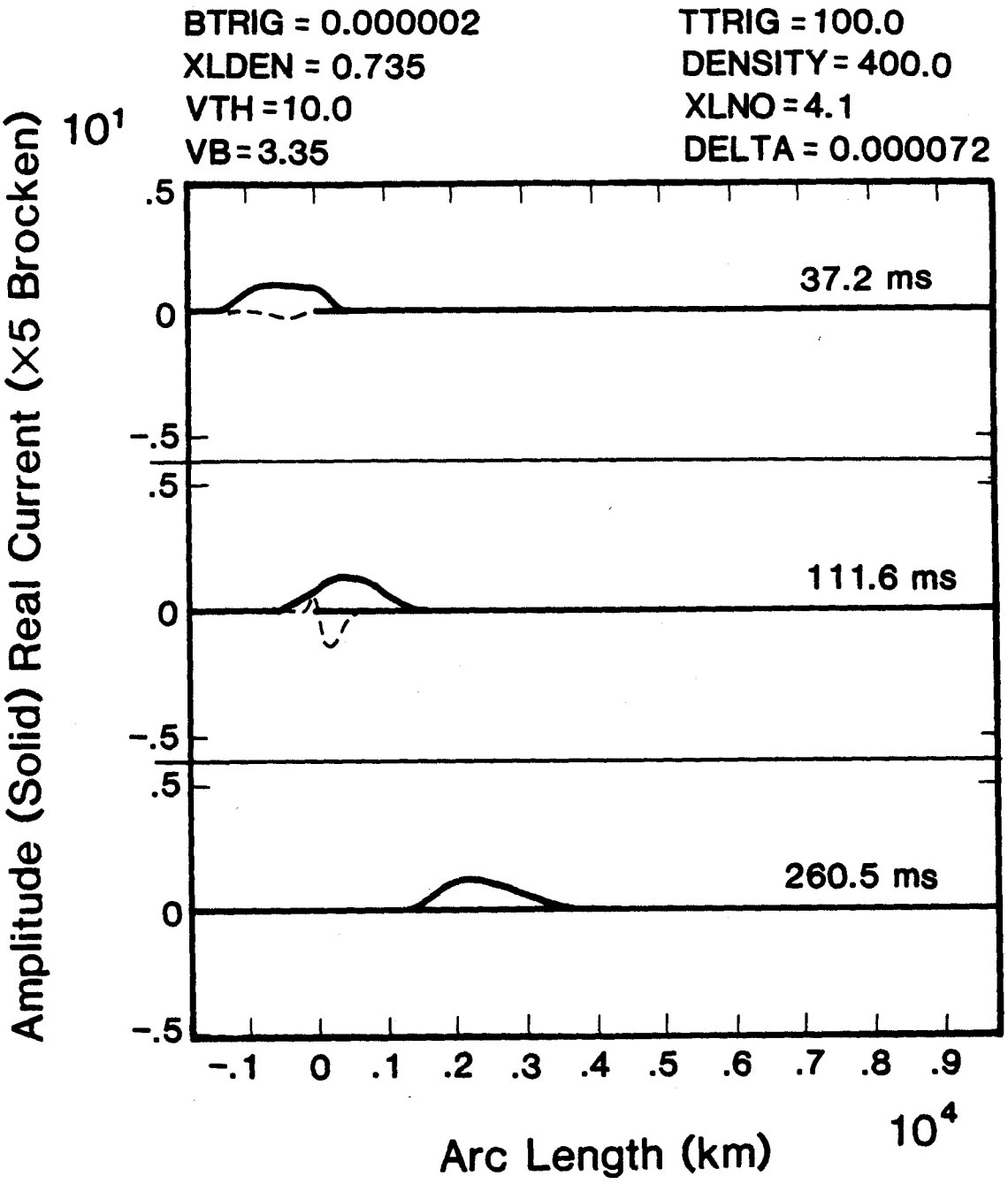
BTRIG = 0.000002
XLDEN = 0.735
VTH = 10.0
VB = 3.35
TTRIG = 100.0
DENSITY = 400.0
XLNO = 4.1
DELTA = 0.000072
Amplitude (Solid) Real Current (X5 Brocken)
10¹
37.2 ms
111.6 ms
260.5 ms
.5
0
-.5
-.1
0
.1
.2
.3
.4
.5
.6
.7
.8
.9
Arc Length (km)
10⁴

Fig.(7.8)

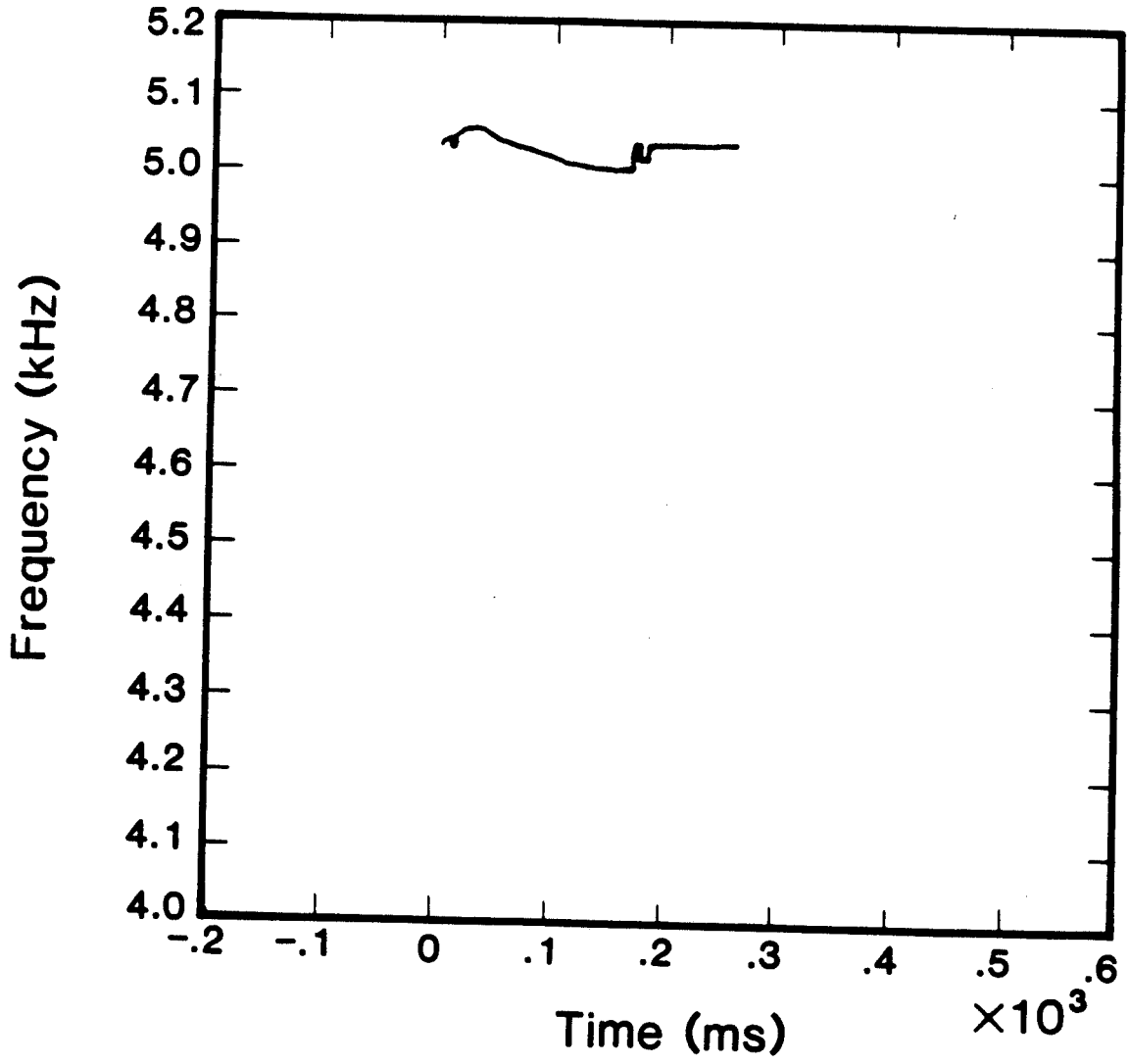
5.2
5.1
5.0
4.9
4.8
4.7
4.6
4.5
4.4
4.3
4.2
4.1
4.0
Frequency (kHz)
-.2
-.1
0
.1
.2
.3
.4
.5
.6
Time (ms)
×10³

Fig.(7.9)

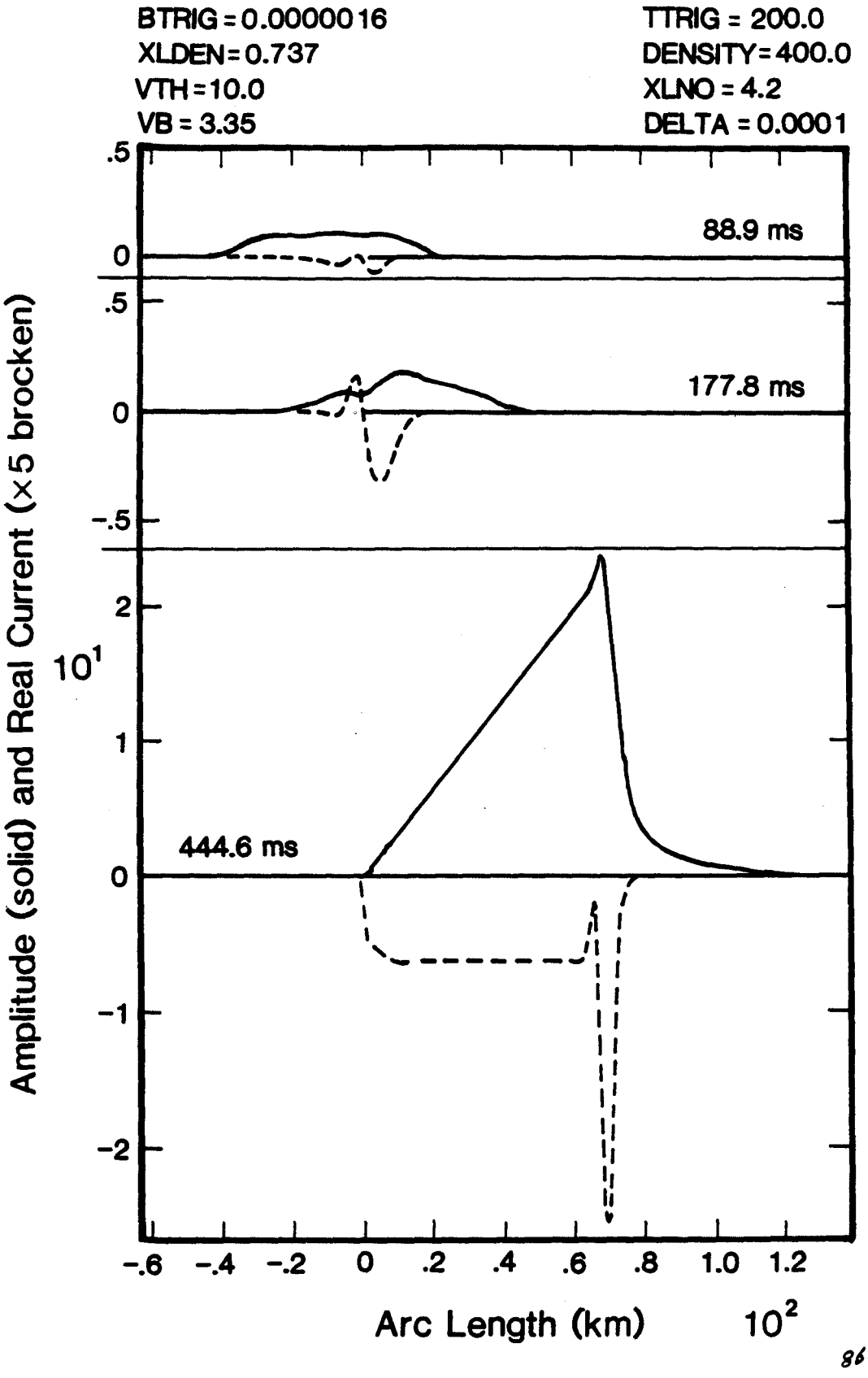

8693.26.12

Fig.(7.10)

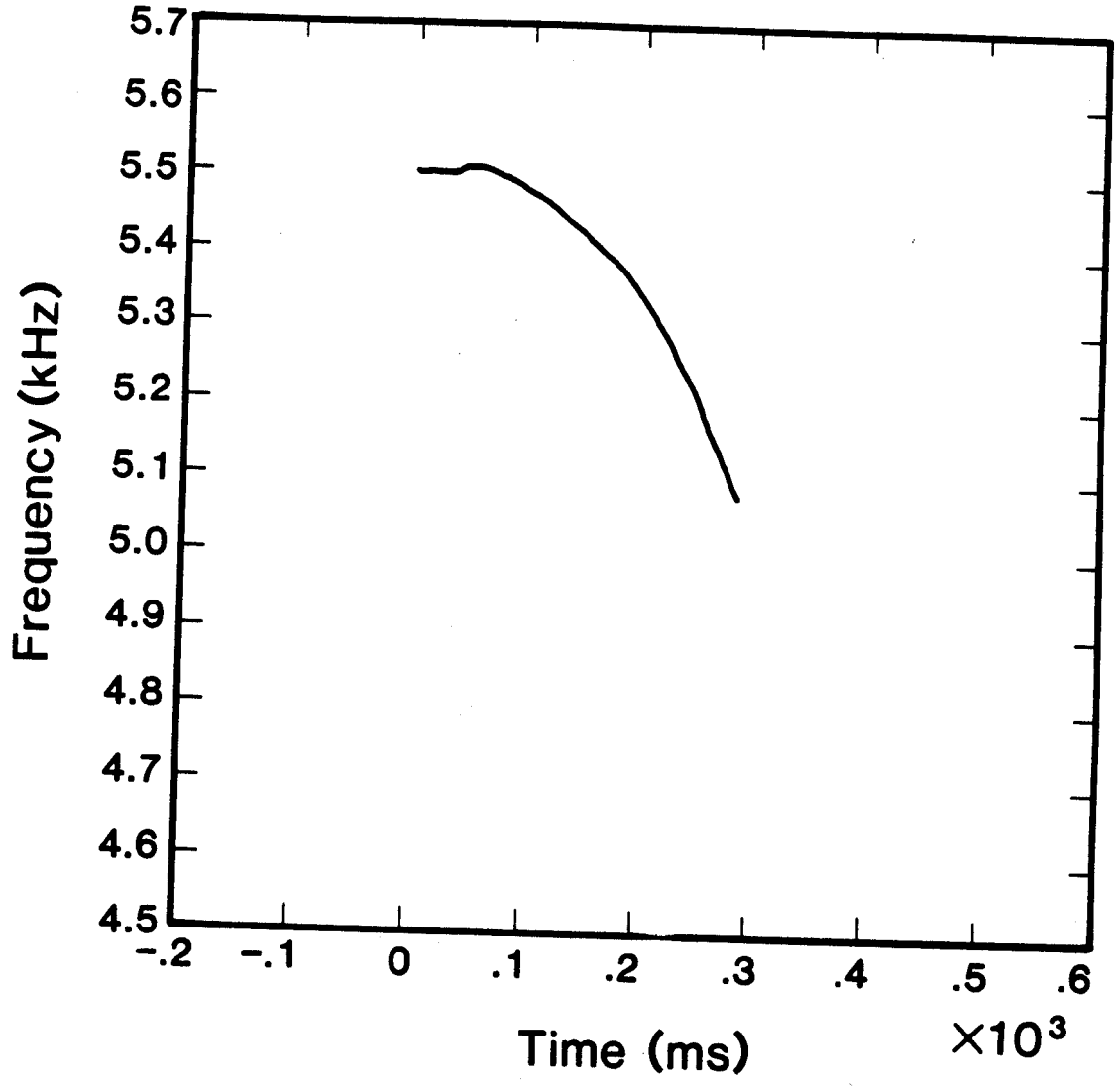

8693.26.18.

Fig.(7.11)

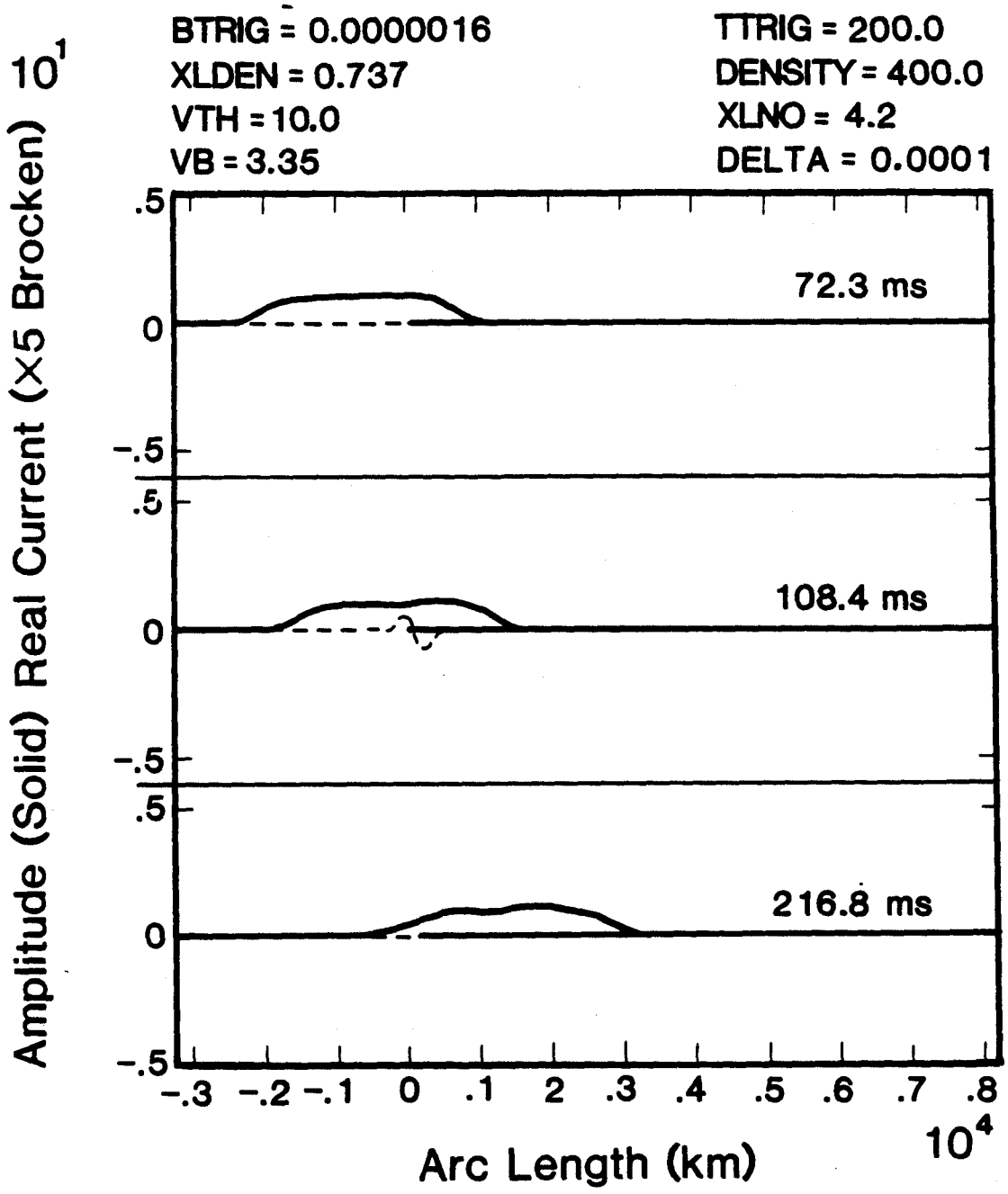
BTRIG = 0.0000016
XLDEN = 0.737
VTH = 10.0
VB = 3.35
TTRIG = 200.0
DENSITY = 400.0
XLNO = 4.2
DELTA = 0.0001
Amplitude (Solid) Real Current (X5 Brocken)
10^1
72.3 ms
108.4 ms
216.8 ms
.5
0
-.5
-.3 -.2 -.1 0 .1 2 .3 .4 .5 .6 .7 .8
10^4
Arc Length (km)

Fig.(7.12)

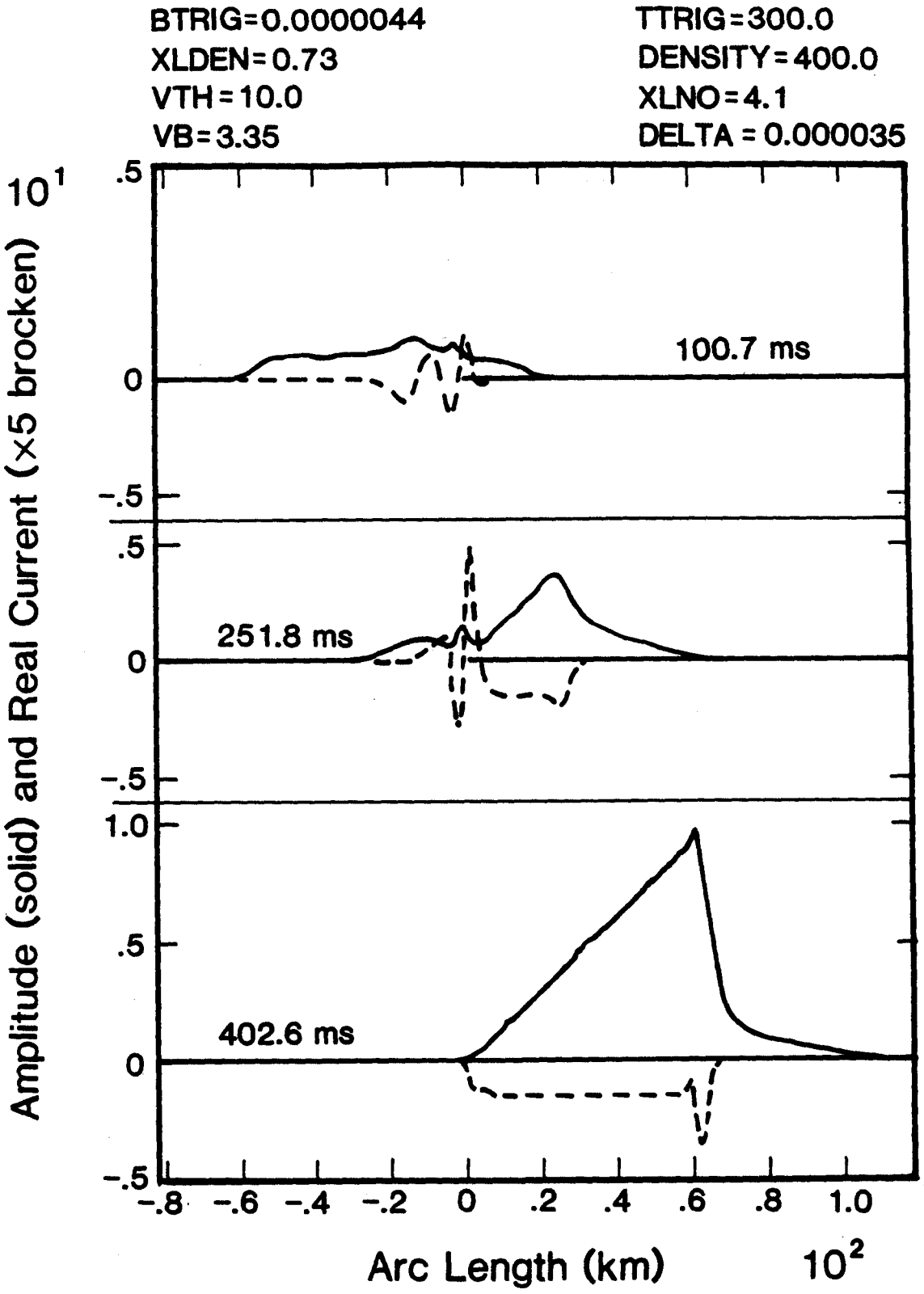
BTRIG=0.0000044
XLDEN=0.73
VTH=10.0
VB=3.35
TTRIG=300.0
DENSITY=400.0
XLNO=4.1
DELTA = 0.000035
Amplitude (solid) and Real Current (×5 brocken)
10¹
100.7 ms
251.8 ms
402.6 ms
.5
0
-.5
1.0
-.8 -.6 -.4 -.2 0 .2 .4 .6 .8 1.0
Arc Length (km)
10²

Fig.(7.13)

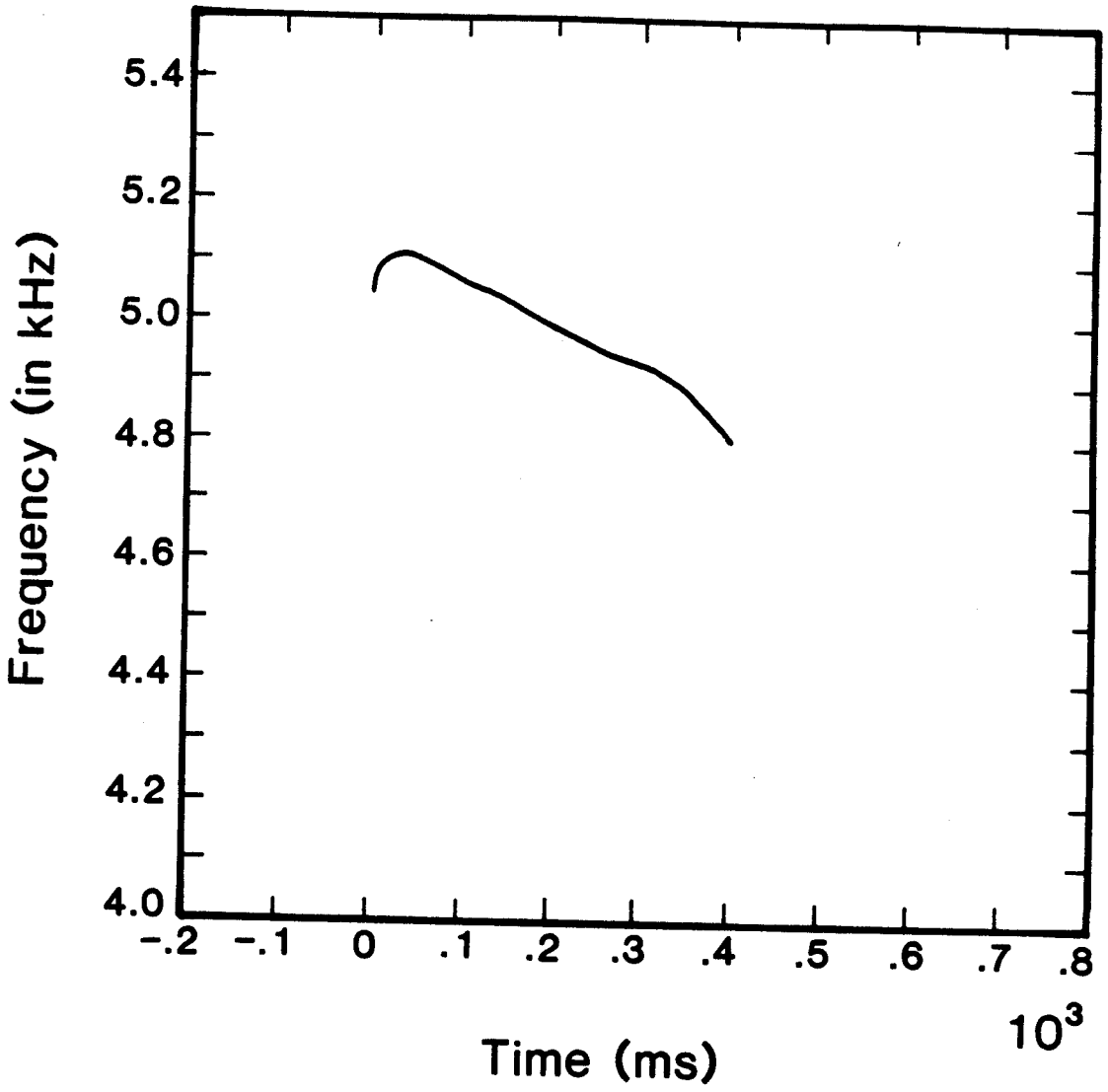
Frequency (in kHz)
5.4
5.2
5.0
4.8
4.6
4.4
4.2
4.0
-.2
-.1
0
.1
.2
.3
.4
.5
.6
.7
.8
10^3
Time (ms)

Fig.(7.14)

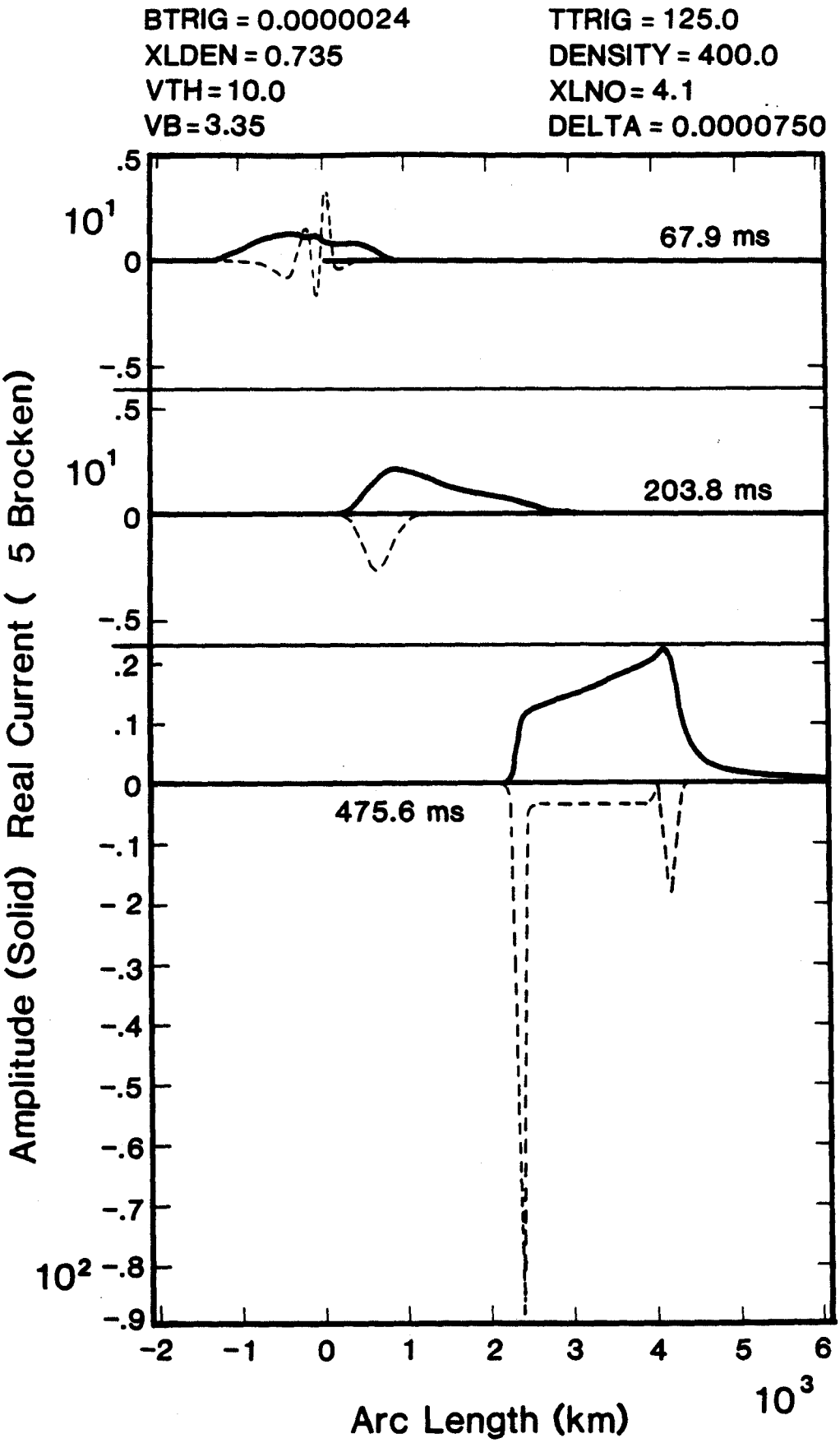
BTRIG = 0.0000024
TTRIG = 125.0
XLDEN = 0.735
DENSITY = 400.0
VTH = 10.0
XLNO = 4.1
VB = 3.35
DELTA = 0.0000750
67.9 ms
203.8 ms
475.6 ms
Amplitude (Solid) Real Current (5 Brocken)
Arc Length (km)
10³
8593.26

Fig.(7.15)

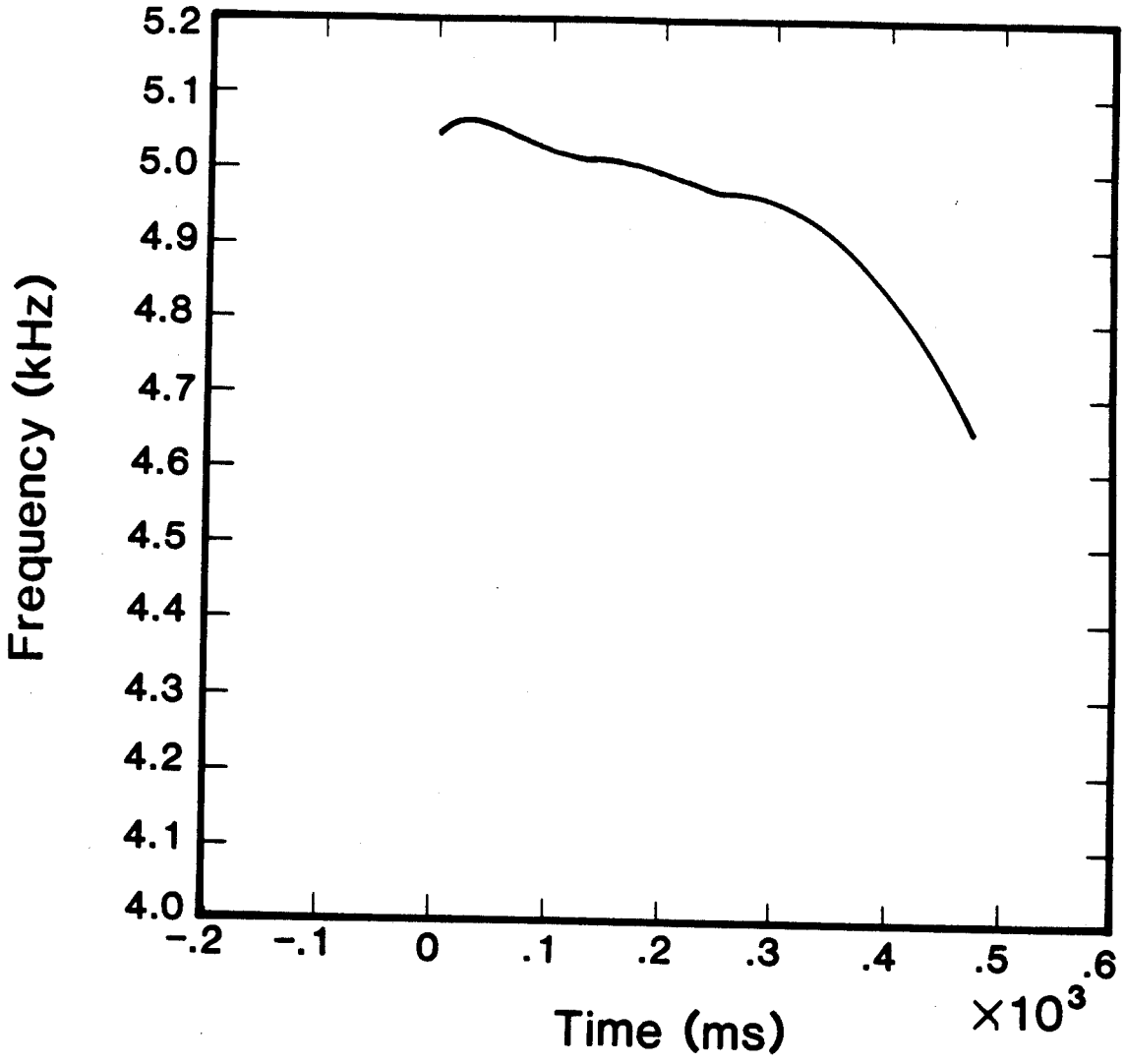

8603.26.21

Fig.(7.16)

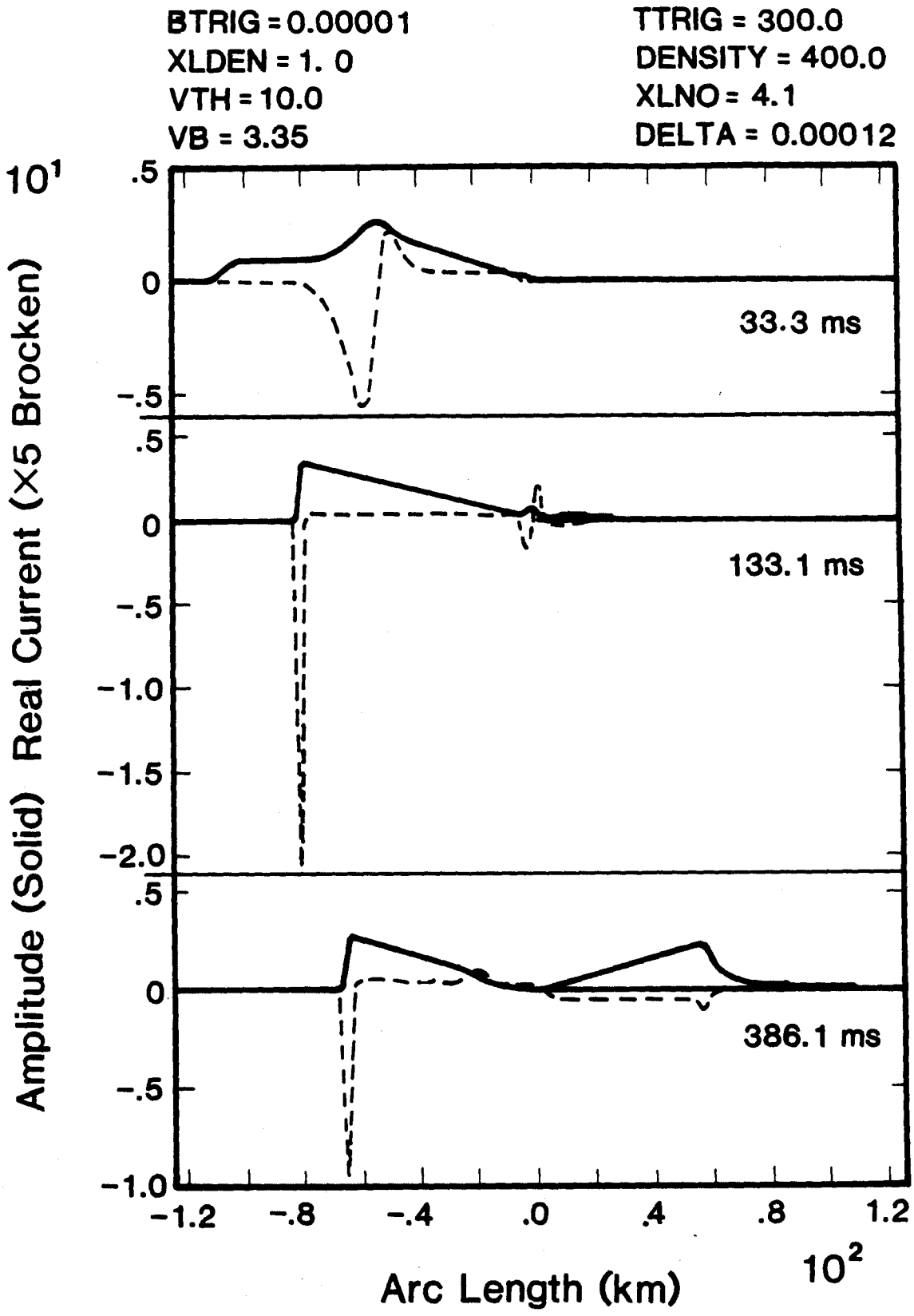
BTRIG = 0.00001
XLDEN = 1. 0
VTH = 10.0
VB = 3.35
TTRIG = 300.0
DENSITY = 400.0
XLNO = 4.1
DELTA = 0.00012
10^1
Amplitude (Solid) Real Current (X5 Brocken)
.5
0
-.5
33.3 ms
.5
0
-.5
-1.0
-1.5
-2.0
133.1 ms
.5
0
-.5
-1.0
386.1 ms
-1.2
-.8
-.4
.0
.4
.8
1.2
10^2
Arc Length (km)

Fig.(7.17)

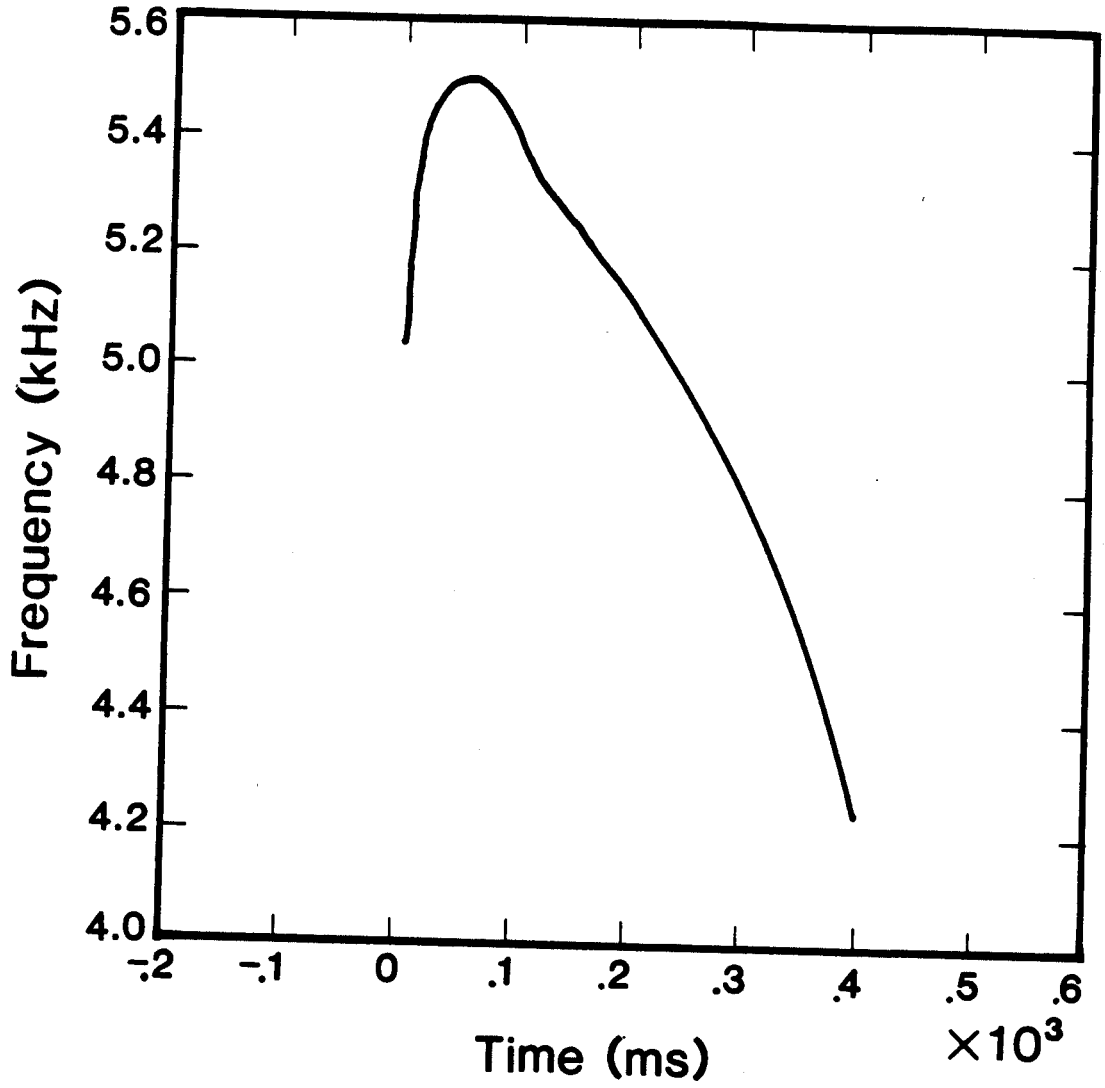

869 3.26.

Fig.(7.18)

ACKNOWLEDGEMENT

We would like to thank C.W. Roberson for initiating this project. We are also grateful for several discussions with D. Nunn, R.N. Sudan and particularly the members of the STAR group at Stanford, R.A. Helliwell, U.S. Inan, T.F. Bell, D.L. Carpenter, C.R. Carlson, which provided much stimulation and understanding of the experimental observations. The research has been sponsored by the Office of Navel Research.

REFERENCES

1) Storey, L.R.O., An investigation of whistling atmospherics, Phil. Trans. Roy. Soc. (London) **A**, 246 (1953).

2) Angerami, J.J., Whistler duct properties deduced from VLF observations made with the Ogo 3 satellite near the magnetic equator, J Geophys Res **75**, 6115 (1970)

3) Barrington, R.E., T.R. Hartz, and R.W. Harvey, Diurnal distribution of ELF, VLF, and LF noise at high latitudes as observed by Alouette 2, J Geophys Res **76**, 5278 (1971).

4) Bell, T.F., Inan, U.S., and Helliwell, R.A., ISEE-1 satellite observations of VLF signals and associated triggered emissions from the Siple station transmitter, Memoirs of National Institute of Polar Research Special Issue, **16**, 128 (1979).

5) Bell, T.F., Inan, U.S., and Helliwell, R.A., Nonducted coherent VLF waves and associated triggered emissions observed on the ISEE-1 satellite, J Geophys Res, **86**, 4649 (1981).

6) Bell, T.F., Inan, U.S., Kimura I., Matsumoto, H., Mukai,T., Hasimoto, K., EXOS-B/ Siple station VLF wave-particle interaction experiments: 2. Transmitter signals and associated emissions, J Geophys Res, **88**, 295 (1983).

7) Dunckel, N. and R.A. Helliwell, Whistler-mode emissions on the OGO 1 satellite, J Geophys Res **74**, 6371 (1969).

8) Dunckel, N., and Helliwell, R.A., Spacecraft observation of man-made Whistler-mode signals near the electron gyrofrequency, Radio Science, **12**, 821 (1977).

9) Gurnett, D.A., R.R. Shaw, R.R. Anderson, et al, Whistlers observed by Voyager 1: Detection of lightning on Jupiter, Geophys Res Lett, **6**, 511 (1979)

10) Inan, U.S., Bell, T.F., and Anderson, R.R., Cold plasma diagnostics using satellite measurements of VLF signals from ground transmitters, J Geophys Res, **82**, 1167

(1977).

11) Inan, U.S., Bell, R.F., Carpenter, D.L., and Anderson, R.R., Explorer 45 and Imp 6 observations in the magnetosphere of injected waves from the Siple Station VLF transmitter, J Geophys Res, **82**, 1177 (1977).

12) Inan, U.S., Pon, M., Banks, P.M., Williamson, P.R., Raitt, W.J., Shawhan, S.D., Modulated beam injection from the space shuttle during magnetic conjunctions of STS 3 with the DE 1 satellite, Radio Science, **19**, 487 (1984).

13) Isenberg, P.A., Koons, H.C., and Fennell, J.F., Simultaneous observations of energetic electrons and dawnside chorus in geosynchronous orbit, J Geophys Res, **87**, 1495 (1982).

14) Kimura, I., Matsumoto, H., Mukai, T., Hashimoto, K., et al, EXOS-B/Siple Station VLF wave-particle interaction experiments: 1. General description and wave-particle correlations, J Geophys Res, **88**, 282 (1983)

15) Lefeuvre, F., and Helliwell, R.A., Characterization of the sources of VLF hiss and chorus observed on GEOS 1, J Geophys Res, **90**, 6419 (1985).

16) Neubert, T., Lefeuvre, F., Parrot, M., Cornilleau-Wehrlin, N., Observations on GEOS-1 of Whistler mode turbulence generated by a ground-based VLF transmitter, Geophys Res Lett, **10**, 623 (1983).

17) Park, C.G., Lin, C.S., Parks, G.K., A ground-satellite study of wave-particle correlations, J Geophys Res, **86**, 37 (1981).

18) Rastani, K., Inan,U.S., and Helliwell, R.A., J Geophys Res **90**, 4128 (1985).

19) Scarf, F.L., D.A. Gurnett, and W.S. Kurth Jupiter plasma wave observations: An initial Voyager 1 overview, Science, **204**, 991 (1979)

20) Shawhan, S.D., Gurnett, D.A, Odem, D.L., Helliwell, R.A., Park, C.G., The plasma wave and quasi-static electric field instrument (PWI) for Dynamics Explorer-A, Space Science Instrumentation, **5**, 535 (1981).

21) Smith, R.L. and Angerami, J.J., Magnetospheric properties deduced from OGO 1 observations of ducted and nonducted Whistlers, J Geophys Res **73**, 1 (1968).

22) Warwick, J.W., J.B. Pearce, D.R. Evans, T.D. Carr, J.J. Schauble et al, Planetary radio astronomy observations from Voyager 1 near Saturn, Science, **212**, 239 (1981)

23) Michel, F.C., and A.J. Dessler, Pulsar disk systems, Astrophys J, **251**, 654 (1981)

24) Helliwell, R.A., Whistlers and Related Ionospheric Phenomena, Stanford University Press, Stanford California, 1965.

25) Stiles, G.S. and Helliwell, R.A., Frequency-time behavior of artificially stimulated VLF emissions, J Geophys Res **80**, 608 (1975).

26) Stiles, G.S., and Helliwell, R.A., Stimulated growth of coherent VLF waves in the magnetosphere, J Geophys Res, **82**, 523 (1977).

27) Das, A.C. and Kulkarni, V.H., Planet Space Sci. **23**, 41 (1975).

28) Dysthe, K.B.. J Geophys Res, **76**, 6915 (1971).

29) Helliwell, R.A., A theory of discrete VLF emissions from the magnetosphere, J Geophys Res **72**, 4773 (1967).

30) Karpman, V.I., Istomin, Ja. N. and Shklyar, D.R., Nonlinear theory of a quasi-monochromatic Whistler mode packet in inhomogeneous plasma, Plasma Physics **16**, 685 (1974).

31) Karpman, V.I., Istomin, Ja.N., Shklyar, D.R., Nonlinear frequency shift and self-modulation of the quasi-monochromatic Whistlers in the inhomogeneous plasma (magnetosphere), Planet. Space Sci., **22**, 859 (1974).

32) Nunn, D., A theory of VLF emissions, Planet. Space Sci. **19**, 1141 (1971).

33) Nunn, D., A self-consistent theory of triggered VLF emissions, Planet. Space Sci. **22**, 349 (1974).

34) Roux, A. and Pellat, R., A theory of triggered emissions, J Geophys Res **83**, 1433 (1978).

35) Sudan, R.N. and Ott, E., Theory of triggered VLF emissions, J Geophys Res **76**, 4463 (1971).

36) Matsumoto. H., *Wave Instabilities in Space Plasmas*, D. Reidel Publ. Comp., Dordrecht (1978).

37) Molvig, K., Hilfer, G., and Myczkowski, J., Self-consistent theory of triggered Whistler emissions, Plasma Fusion Center Report 86-3.

38) Helliwell, R.A., Controlled stimulation of VLF emissions from Siple Station, Antarc-

tica, Radio Sci. **18**, 801, (1983).

39) Helliwell, R.A. and Katsufrakis, J.P., VLF Wave injection into the magnetosphere from Siple station, Antarctica, J Geophys Res **79**, 2511 (1974).

40) Bell, T.F., Inan, U.S., Transient nonlinear pitch angle scattering of energetic electrons by coherent VLF wave packets in the magnetosphere, J Geophys Res, **86**, 9047 (1981).

41) Smith, R.L., Helliwell, R.A., and Yabroff, I., A theory of trapping of whistlers in field-aligned columns of enhanced ionization., J Geophys Res,**65**, 815, (1960)

42) Hansen, S.F. A mechanism for the production of very-low-frequency emissions, J Geophys Res, **68**, 5925 (1963).

43) Brice, N.M., An explanation of triggered very-low frequency emissions, J Geophys Res **68**, 4626 (1963).

44) Inan, U.S., Bell, T.F., and Helliwell, R.A., Nonlinear pitch angle scattering of energetic electrons by coherent VLF waves in the magnetosphere, J Geophys Res, **83**, 3235 (1978).

45) Omura, Y., and Matsumoto, H., Computer simulations of basic processes of coherent Whistler wave-particle interactions in the magnetosphere, J Geophys Res, **87**, 4435 (1982).

46) Nunn, D., The quasistatic theory of triggered VLF emissions, Planet. Space Sci., **32**, 325 (1984).

47) Matsumoto, H., and Omura, Y., Cluster and channel effect phase bunchings by Whistler waves in the nonuniform geomagnetic field, J Geophys Res, **86**, 779 (1981).

48) Sudan, R.A. and Denavit, J., VLF emissions from the magnetosphere, Physics Today **26**, No. 12, 36 (1973).

49) Vomvoridis, J.L., Crystal, T.L, and Denavit, J., Theory and computer simulations of magnetospheric very low frequency emissions, J Geophys Res, **87**, 1473 (1982).

50) Matsumoto, H., and Omura, Y., Computer simulation studies of VLF triggered emissions deformation of distribution function by trapping and detrapping, Geophys Res Lett, **10**, 607 (1983).

51) Helliwell, R.A. and Inan, U.S., VLF Wave growth and discrete emission triggering in the magnetosphere: A feedback model, J Geophys Res **87**, 3537 (1982).

52) Lyons, L.R., and Williams, D.J., A comment on the effects of man-made VLF waves on the radiation belts, Geophys Res Lett, **5**, 116 (1978).

53) Bernstein, I.B., Geometric optics in space and time varying plasmas, The Physics of Fluids **18**,320,(1975)

54) Luette, J.P., Park, C.G., and Helliwell, R.A., The control of magnetospheric chorus by power line radiation, J Geophys Res, **84**, 2657 (1979).

55) Brice, N. Fundamentals of VLF emission generation mechanism, J Geophys Res, **69**, 4515 (1964).

56) Palmadesso, F. and Schmidt, G., Collisionless damping of a large amplitude whistler wave, Phys. Fluids, **14**, 1411 (1971).

57) Palmadesso, G. and Schmidt, G., Stability of a steady, large amplitude whistler wave, Phys. Fluids, **15**, 485, (1972).

58) Ashour-Abdalla, M., Amplification of Whistler waves in the magnetosphere, Planet. Space Sci. **20**, 639 (1972).

59) Helliwell, R.A. and Crystal, T.L., A feedback model of cyclotron interaction between whistler-mode waves and energetic electrons in the magnetosphere, J Geophys Res, **78**, 7357 (1973).

60) Olson, W.P., and Pfitzer, K.A., A quantitative model of the magnetospheric magnetic field, J Geophys Res, **79**, 3739 (1974).

61) Angerami, J.J. and Thomas, J.O., Studies of Planetary Atmospheres; 1. The Distribution of Electrons and Ions in the Earth's Exosphere, J Geophys Res **69**, 4537 (1964).

62) Park, C.G., Carpenter, D.L., and Wiggin, D.B., Electron density in the plasmasphere: Whistler data on solar cycle, annual, and diurnal variations, J Geophys Res, **83**, 3137 (1978).

63) Nayfeh, A.H., *Perturbation Methods*, John Wiley & Sons, New York, 1973.

64) Bender, C.M., and Orszag, S.A. Advanced mathematical methods for scientists and engineers, McGraw-Hill Book Co., New York, 1978.

65) Krall, N.A. and Trivelpiece, A.W. Principles of Plasma Physics, McGrawhill Book Company, New York N.Y., 447 (1973).

66) Lax, P.D. and Wendroff, B., Systems of conservation laws, Commun. Pure Appl. Math., **13**, 1277 (1960).

67) Carlson, C.R., Helliwell, R.A., and Carpenter, D.L., Variable frequency VLF signals in the magnetosphere: Associated phenomena and plasma diagnostics, J Geophys Res, **90**, 1507 (1985).